



## Sol-Gel Materials for Optical Waveguide Applications

Item type	text; Electronic Dissertation
Authors	Himmelhuber, Roland
Publisher	The University of Arizona.
Rights	Copyright © is held by the author. Digital access to this material is made possible by the University Libraries, University of Arizona. Further transmission, reproduction or presentation (such as public display or performance) of protected items is prohibited except with permission of the author.
Downloaded	17-May-2016 08:17:29
Link to item	<a href="http://hdl.handle.net/10150/325227">http://hdl.handle.net/10150/325227</a>

SOL-GEL MATERIALS FOR OPTICAL WAVEGUIDE  
APPLICATIONS

by  
Roland Himmelhuber

---

A Dissertation Submitted to the Faculty of the  
COLLEGE OF OPTICAL SCIENCES

In Partial Fulfillment of the Requirements  
For the Degree of

DOCTOR OF PHILOSOPHY

In the Graduate College

THE UNIVERSITY OF ARIZONA

2014

THE UNIVERSITY OF ARIZONA  
GRADUATE COLLEGE

As members of the Dissertation Committee, we certify that we have read the dissertation prepared by Roland Himmelhuber, titled *Sol-Gel materials for optical waveguide applications* and recommend that it be accepted as fulfilling the dissertation requirement for the Degree of Doctor of Philosophy.

Date: June 19, 2014

---

Robert A. Norwood

Date: June 19, 2014

---

Mahmoud Fallahi

Final approval and acceptance of this dissertation is contingent upon the candidates submission of the final copies of the dissertation to the Graduate College. I hereby certify that I have read this dissertation prepared under my direction and recommend that it be accepted as fulfilling the dissertation requirement.

Date: June 19, 2014

---

Dissertation Director: Nasser Peyghambarian

## STATEMENT BY AUTHOR

This dissertation has been submitted in partial fulfillment of requirements for an advanced degree at The University of Arizona and is deposited in the University Library to be made available to borrowers under rules of the Library.

Brief quotations from this dissertation are allowable without special permission, provided that accurate acknowledgment of source is made. Requests for permission for extended quotation from or reproduction of this manuscript in whole or in part may be granted by the head of the major department or the Dean of the Graduate College when in his or her judgment the proposed use of the material is in the interests of scholarship. In all other instances, however, permission must be obtained from the author.

SIGNED: \_\_\_\_\_ ROLAND HIMMELHUBER

## ACKNOWLEDGEMENTS

I would like to thank Prof. Nasser Peygambarian and Prof. Rober A. Norwood for their guidance and support for this research. I would also like to thank Nasser for believing that a German chemist could succeed in Optical sciences and Bob for always being open for any idea as well as for his seemingly endless optimism.

I would to thank all the people who contributed to this work, by either discussions or experiments. One spacial thanks should go to Chris DeRose for showing me around and teaching me all the cleanroom necessities. I would also like to thanks Palash Gangopadhyay and Ramakrishna Voorakaranam for never being annoyed by my endless questions and for always being ready to help. Oscar Herrera also deserves a thank you for making the time here very fun and reintroducing me to  $\text{\LaTeX}$ . I also would like to thank Seyed Soroush Mehravar for measuring my samples over and over and over again. I would also like to Olli Nordman for fixing the Denton again, again and again.

Finally, I would like to thank my wife Anna Dornhaus for dealing with a grad student for this long, my parents for never pressuring me but always believing in me as well as always supporting what I did and my brother Stefan for beeing there when I needed him.

## DEDICATION

*To all my Family, the one I was born in, the one I married and the one I made.*

*Für meine Familie, die alte, die neue und die selbstbemachte.*

## TABLE OF CONTENTS

LIST OF TABLES . . . . .	<b>8</b>
LIST OF FIGURES . . . . .	<b>9</b>
ABSTRACT . . . . .	<b>12</b>
CHAPTER 1. SOL-GEL MATERIALS . . . . .	<b>14</b>
1.1. Introduction . . . . .	14
1.2. Sol gel materials for polymer modulators . . . . .	15
1.2.1. Optical properties . . . . .	16
1.2.2. Electrical properties . . . . .	26
1.3. High index sol gel materials . . . . .	30
1.3.1. Synthesis . . . . .	30
1.3.2. Chemical Analysis . . . . .	32
1.3.3. Optical properties . . . . .	34
1.3.4. Physical properties . . . . .	41
1.4. Summary . . . . .	45
CHAPTER 2. ELECTRO OPTIC POLYMER CHARACTERIZATION . . . . .	<b>47</b>
2.1. Introduction . . . . .	47
2.2. Second order non-linearities . . . . .	48
2.3. The electro optic effect . . . . .	50
2.4. The relation between $r$ and $d$ . . . . .	54
2.5. $r_{33}$ measurements in a transmission setup . . . . .	56
2.6. Second harmonic microscopy . . . . .	58
2.7. Analysis . . . . .	62
2.8. Summary . . . . .	67
CHAPTER 3. ELECTRO OPTIC MODULATORS . . . . .	<b>69</b>
3.1. Introduction . . . . .	69
3.2. Silicon EO hybrid modulators . . . . .	70
3.2.1. Optical Design . . . . .	71
3.2.2. Electrode Design . . . . .	74
3.2.3. Measurement results . . . . .	84
3.3. Silicon nitride devices . . . . .	87
3.3.1. Optical Design . . . . .	88
3.3.2. Sidecladding for field concentration . . . . .	88
3.4. Summary . . . . .	93

TABLE OF CONTENTS—*Continued*

APPENDIX A. SOL-GEL RECIPES . . . . .	<b>94</b>
APPENDIX B. MATLAB - OCTAVE CODE . . . . .	<b>103</b>
B.1. Optical field handling . . . . .	103
B.2. Electrical field handling . . . . .	107
B.3. CPS capacitance calculations . . . . .	109
B.4. Electrode loss calculations . . . . .	113
B.5. Reflection correction factor calculations . . . . .	114
APPENDIX C. FABRICATION DESCRIPTIONS . . . . .	<b>119</b>
C.1. Electrode Fabrications by lift off . . . . .	119
REFERENCES . . . . .	<b>120</b>

## LIST OF TABLES

TABLE 1.1. Silane precursors used to tune the refractive index and reduce the optical loss. Naphthalene-trimethoxy-silane is a powder, so no refractive index is given. . . . .	19
TABLE 2.1. Index contraction . . . . .	49
TABLE 2.2. Index contraction . . . . .	53
TABLE 2.3. Calculated and measured $d_{13}$ values for different chromophor loadings. . . . .	57
TABLE 2.4. Complex refractive indices of the thin film stack materials at relevant wavelengths. Ellipsometric measurements were performed on a GSE 5 spectroscopic ellipsometer from Sopra between 400 and 800nm. The EO polymer film was poled on an indium thin oxide (ITO) coated glass substrate with gold as the top electrode. The film was characterized by a Teng-Man measurement and at a $r_{33}$ coefficient of 130 pm/V. The given refractive indices are for light polarized along the poling axis. For ellipsometry a uniaxial model was used with a Sellmeier dispersion law and two absorption peaks around 865 nm and 520nm. The prism coupler was a Metricon 2010 model with lasers at 532, 633, 816, 1305 and 1554nm. Transmission measurements were performed on a Varian Cary 5000. . .	64
TABLE 2.5. Calculated correction factors with which the second harmonic signal from poled EO polymer on silica on silicon must be multiplied to be comparable with films on plain silica. . . . .	68

## LIST OF FIGURES

FIGURE 1.1.	Hydrolyzation condensation reaction of dimethyl dimethoxy silane	15
FIGURE 1.2.	Diphenyl silane diol . . . . .	17
FIGURE 1.3.	Decomposition of Irgacure 369 under UV-radiation . . . . .	18
FIGURE 1.4.	Absorption spectra of two example systems with hydrolyzation ratios of 0.45 and 0.36, respectively. . . . .	21
FIGURE 1.5.	Refractive index vs. molar percentage of PTMS, measured in cured films. . . . .	22
FIGURE 1.6.	Refractive index vs. molar percentage of BPFDPDMS, measured in cured films. . . . .	23
FIGURE 1.7.	Optical loss data for RH 10 obtained using a liquid prism set up.	24
FIGURE 1.8.	Cross section of an RH10 waveguide on RH8 undercladding. . .	25
FIGURE 1.9.	Loss measurement of RH 10 waveguides, with RH8 as a cladding.	25
FIGURE 1.10.	Voltage drop over a multilayer stack. . . . .	26
FIGURE 1.11.	Structure of 3-(triethoxysilyl)-propyl succinic acid anhydride a), the di-acid b) and a di-ester c). Al stands for an alky group . . . . .	27
FIGURE 1.12.	FT-IR spectrum of RH28-2 with deconvolved peaks. The peaks were assigned as follows: $1717\text{cm}^{-1}$ (MAPTMS), $1700\text{cm}^{-1}$ (acid of SucAHTES), $1738\text{cm}^{-1}$ (ester of SucAHTES) . . . . .	28
FIGURE 1.13.	. . . . .	29
FIGURE 1.14.	Structures of glycidyl methacrylate a) and propylene oxide b) .	31
FIGURE 1.15.	Spin curves for RHTi1 (containing only PO) and RHTi2 (containing only GLYME) . . . . .	33
FIGURE 1.16.	Structures of propylene glycol a), 1-chloro-2-propanol b) and 2-chloro-1-propanol . . . . .	34
FIGURE 1.17.	Structures of 2,3 dihydroxypropylmethacrylate a), 3-chloro-2-hydroxypropyl methacrylate b) and 2-chloro-3-hydroxypropyl methacrylate . . . . .	34
FIGURE 1.18.	Particle as it might be present in the material. . . . .	35
FIGURE 1.19.	Particle size distribution of RHTi2 measured by dynamic light scattering. . . . .	35
FIGURE 1.20.	XPS survey spectra of a material made only with PO (RHTi13) and of one only made with GLYME(RHTi13). Peak assignments are shown in the graph. Note that the C 1s peak in the black curve is not visible at this magnification due to its small size. . . . .	36
FIGURE 1.21.	Transmission spectra of RHTi1 and RHTi2 measured on quartz at the wavelengths relevant for ellipsometry. . . . .	37
FIGURE 1.22.	GLYME content versus the molar fraction of carbon in the spun film as measured by XPS. . . . .	38

LIST OF FIGURES—*Continued*

FIGURE 1.23. Refractive index at the D-line of sodium of RHTi samples with varying amount of GLYME. . . . .	39
FIGURE 1.24. Change of the refractive index of RHTi1 and RHTi2 due to heat treatment at 550°C . . . . .	40
FIGURE 1.25. X-ray diffraction measurement for an amorphous and crystalline RHTi1 film. . . . .	41
FIGURE 1.26. Surface profile scan over a 300m wide structure. The image in the middle shows a microscope picture of the sample. . . . .	42
FIGURE 1.27. Topographic image of an RHTi7 film measured by AFM . . . . .	43
FIGURE 1.28. AFM phase image of an RHTi7 film representing the relative hardness of the surface. . . . .	44
FIGURE 1.29. EFM phase image of a RHTi7 film representing the relative static dielectric constant. . . . .	45
FIGURE 1.30. Distribution of relative dielectric constants computed from EFM image. . . . .	46
FIGURE 2.1. Schematic of the transmission $r_{33}$ setup . . . . .	57
FIGURE 2.2. Cross section of coplanar samples (a) and top view of the gold electrodes (b). The right hand side shows a zoom in of the area of interest. . . . .	59
FIGURE 2.3. Schematic of the multiple-photon imaging system . . . . .	60
FIGURE 2.4. (a):Composite of SH(red) and TH(green), (b): SH in the poled region, (c):TH from on top of the gold electrodes. The purple box in (b) indicates the region in which the quantitative SHG data was collected. . . . .	62
FIGURE 2.5. SH signal as a function of the linear polarization angle of the fundamental. . . . .	63
FIGURE 2.6. Ratio of the measured $r_{33}$ to the square root of the second harmonic. . . . .	65
FIGURE 2.7. Schematic of the multilayer stacks of the calibration samples(left) and silicon wafer with a silica layer(right). For reflection calculations only the area between the electrodes (see Fig. 2.2) is considered. . . . .	66
FIGURE 3.1. Schematic of a Mach-Zehnder modulator. The phase of the modulated arm is changed by $\pi$ . . . . .	69
FIGURE 3.2. Schematic of the EO-silicon hybrid modulator structure. . . . .	72
FIGURE 3.3. The confinement factor in the polymer ( $n = 1.7$ ) and $n_{eff}^3$ vs. silicon waveguide width. The height of the silicon waveguide is 250nm and the wavelength of light is 1550nm. . . . .	73
FIGURE 3.4. Confinement factor multiplied by $n_{eff}^3$ for 1550nm light vs. waveguide with for different waveguide heights. . . . .	74
FIGURE 3.5. Confinement factor multiplied by $n_{eff}^3$ for 1310nm light vs. waveguide with for different waveguide heights. . . . .	75

LIST OF FIGURES—*Continued*

FIGURE 3.6. Electrical field of a TE mode in a 260nm wide and 300nm high silicon waveguide with EO cladding on SiO <sub>2</sub> at 1550nm. . . . .	76
FIGURE 3.7. Simulated DC field around the EO polymer cladding waveguide for 6 $\mu$ m electrode spacing and 175nm electrode height. . . . .	77
FIGURE 3.8. Simulated DC field around the EO polymer cladding waveguide for 3 $\mu$ m electrode spacing and 2 $\mu$ m electrode height. . . . .	78
FIGURE 3.9. Simulated DC field around the EO polymer cladding waveguide for 2 $\mu$ m electrode spacing and 2 $\mu$ m electrode height. . . . .	79
FIGURE 3.10. Overlap integral of the optical field in the EO polymer with the electrical DC field(1550nm light) . . . . .	80
FIGURE 3.11. Overlap integral of the optical field in the EO polymer with the electrical DC field(1310nm light) . . . . .	81
FIGURE 3.12. Line capacitance for 2,4,6, and 8 $\mu$ m electrode spacing plotted over the electrode width . . . . .	82
FIGURE 3.13. Calculated electrode loss for different electrode geometries ( a)= 10 $\mu$ m wide, 2 $\mu$ m gap, b)= 10 $\mu$ m wide, 4 $\mu$ m gap, c)= 50 $\mu$ m wide, 2 $\mu$ m gap, d)= 50 $\mu$ m wide, 4 $\mu$ m gap, e)= 200 $\mu$ m wide, 2 $\mu$ m gap, f)= 200 $\mu$ m wide, 4 $\mu$ m gap. . . . .	83
FIGURE 3.14. Calculated $V_\pi$ L and FOM . . . . .	84
FIGURE 3.15. Schematic of the V measurement setup. Yellow lines show electrical and blue ones show optical connections . . . . .	85
FIGURE 3.16. Screenshot from the oscilloscope used to measure $V_\pi$ . . . . .	87
FIGURE 3.17. The confinement factor in the polymer ( $n = 1.7$ ) and $n_{eff}$ vs. Si <sub>3</sub> N <sub>4</sub> waveguide width. The height of the Si <sub>3</sub> N <sub>4</sub> waveguide is 250nm and 500nm, while the wavelength of light is 1310nm. . . . .	89
FIGURE 3.18. Confinement factor multiplied by $n_{eff}^3$ for 1310nm light vs. waveguide with for different waveguide heights. . . . .	90
FIGURE 3.19. Electrical modulation field distribution for a Si <sub>3</sub> N <sub>4</sub> device with sol gel side cladding. . . . .	91
FIGURE 3.20. Electrical modulation field distribution for a Si <sub>3</sub> N <sub>4</sub> device with sol gel side cladding ( $\epsilon = 10$ ). . . . .	91
FIGURE 3.21. Electrical modulation field distribution for a Si <sub>3</sub> N <sub>4</sub> device with sol gel side cladding ( $\epsilon = 100$ ). . . . .	92
FIGURE 3.22. Electrical field enhancement increases with decreasing EO polymer gap. . . . .	92

## ABSTRACT

Sol-gel materials are an important material class, as they provide for easy modification of material properties, good processability and routine synthesis. This allows for the tailoring of the material properties to the needs of specific device designs. In the case of electro-optic modulators with a coplanar or coplanar strip (CPS) electrode design, sol-gel cladding materials can be used to confine the light to the electro-optic material as well as to concentrate the electrical field used for poling and driving the modulator. Another important material property that can influence the poling efficiency is the conductivity of the material surrounding the electro-optic material, and this property can also be controlled.

In this dissertation I discuss several approaches to altering the material properties of sol-gel materials in order to achieve a specific performance objective. The optical loss in the telecom regime as well the refractive index will be discussed. I will introduce a novel titania-based family of sol-gel materials, which exhibit very high refractive indices, tuneability and high dielectric constant ( $\epsilon$ ).

Coplanar electrode design is useful for device platforms that do not allow for a microstrip geometry, such as silicon and  $\text{Si}_3\text{N}_4$  devices. CPS electrodes however bring new challenges with them, especially optimizing the poling process. I will discuss a method for characterizing coplanar poled polymer films by a modified Teng-Man technique as well as with second harmonic microscope (SHM). SHM allows for an almost real-time mapping of the Pockels coefficient. The described method allows for quantitative measurements of the Pockels coefficient in a poled film with spatial resolution at the micron level.

Finally, I will discuss the device design considerations for a silicon-EO hybrid modulator. Optimal dimensions for the silicon waveguide are shown and the feasibility of the proposed electrode design for high speed operation is theoretically shown. All

design parameters, including electrode spacing and height are optimized towards the highest possible figure of merit. The functionality of a simple test device is shown. For  $\text{Si}_3\text{N}_4$  waveguides optimal dimensions are found as well and the influence of a high  $\epsilon$  sol-gel side cladding is examined.

## Chapter 1

# SOL-GEL MATERIALS

### 1.1 Introduction

Sol-gel materials are most commonly perceived as either sols, gels, resins or films which are prepared by the hydrolyzation-condensation reaction of metal alkoxides or halides. A sol is a subclass of colloid, which is defined as a suspension in which the suspended particles are so small that gravity has little influence on the position or movement when compared to Brownian motion [1]. Common colloids are fog, where water droplets are suspended in air, and milk where fat and protein droplets are suspended in water. If a solid is suspended in a liquid the suspension is called a sol. If the sol is dried and the condensation reaction continues until the formed molecules grow larger and larger, combining into virtually a single molecule with the macroscopic dimensions of the reaction vessel, the material is called a gel. If during solvent removal the sol particles do not react with each other and stay separated the resulting liquid is often called a resin. It is, however, not necessary to remove the solvent for gelation to occur. A solvent free resin can then be either thermally or UV cured if the appropriate moieties (like a organic epoxy or methacrylate group) are present. This can be done in bulk or after film formation by spin or dip coating. It is also possible to spin film directly from a sol, the formed film is technically also a gel, but often more dense.

The sol-gel materials discussed in this thesis are also inorganic organic hybrid materials. This means that organic and inorganic parts of the material are mixed on a molecular level. Organic molecules are commonly described as consisting mainly of carbon and hydrogen. Carbon-carbon bonds form the backbone of molecules and polymers, while hydrogen populates the bonds not occupied by carbon. Sulfur, oxy-

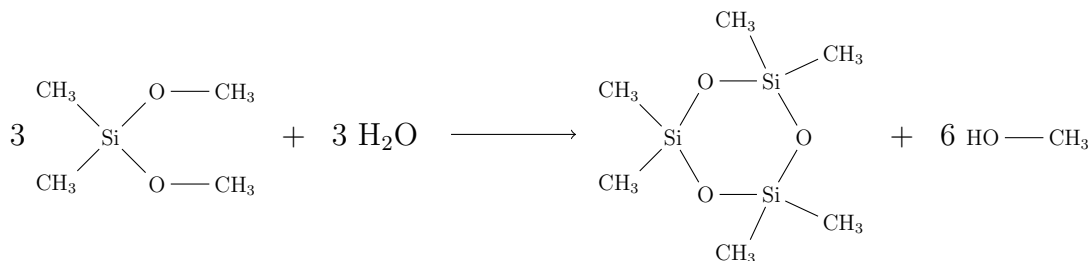


FIGURE 1.1. Hydrolyzation condensation reaction of dimethyl dimethoxy silane

gen, nitrogen can be present, among others as well. Inorganic compounds can be classified in many different ways; classes include oxides, metals, minerals and ceramics. They all have in common that they generally lack carbon-carbon bonds. Inorganic-organic hybrids are materials in which the organic and inorganic parts are intertwined. A very simple case of this is shown in 1.1. Here dimethyl dimethoxy silane reacts with water to form a ring of silicon and oxygen. The ring itself can be considered inorganic, because it only contains silicon (a half metal) and oxygen. The methyl groups attached to the silicon on the other hand are purely organic.

A benefit of using inorganic-organic hybrid materials is that the material properties can be altered easily by choosing precursor molecules with different organic end groups such that the resulting material can be designed to meet the needs of the specific application. The synthesis of these sol-gel materials is typically a one pot single step process which can be done in a simple scintillation vial without the need for chemical glassware and numerous reaction setups.

## 1.2 Sol gel materials for polymer modulators <sup>1</sup>

Polymer-based EO modulators have been of great interest for a number of years, mainly because of their promising high speed capabilities. Two primary fabrication methods for Mach-Zehnder EO modulators have been used so far. One approach is to

<sup>1</sup>Taken in large parts from Himmelhuber et.al. [2]

pattern the EO polymer directly by reactive ion etching [3]. Another possibility is to pattern trenches in a passive material like inorganic-organic hybrid sol-gel materials and fill the trenches with EO polymer [4]. This approach has several advantages, like the ability to only use EO polymer in the active region and use only passive materials in the waveguide transition section, which can decrease the overall optical loss in the device, because of both better coupling efficiency and the high near infrared (near-IR) losses of some EO chromophores. It has also been shown that using sol-gel materials can increase the poling efficiency in the device[5].

### 1.2.1 Optical properties

Passive sol-gel materials play an important role in the development of electro-optic(EO) polymer-based modulators, because of their variety of available refractive indices. They can be used to form passive waveguide transitions to minimize coupling loss or as cladding layers for the EO polymer. The demands for these two applications are different. For waveguide transitions the most important factor is the optical loss. If the sol-gel material is used as a cladding for the EO material the electrical conductivity at poling conditions as well as the dielectric constant are important factors for efficient poling and driving the modulator. Polymer-based EO modulators have been of great interest for a number of years, mainly because of their promising high speed capabilities. Much effort has been put into the development of polymeric materials with very high  $r_{33}$  coefficients as well as in the overall device design [6]. Photopatternable sol-gel materials with low ( $< 0.8\text{dB/cm}$ ) losses at  $1.55\mu\text{m}$  have been known for some time. They were first reported via a water free synthesis [7]. This method uses a prehydrolyzed precursor, diphenylsilanediol (see Fig. 1.2) which reacts under base catalysis with a crosslinkable alkoxy silane. Because no additional water is introduced into the synthesis, the percentage of uncondensed Si-OH groups is negligible. This eliminates one major source of absorption losses common in sol-gel materials,

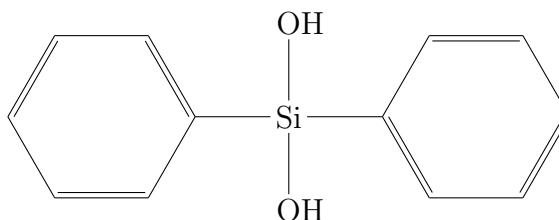


FIGURE 1.2. Diphenyl silane diol

i.e., large absorption by the OH functionality.

Even though this approach is extremely useful for eliminating loss caused by OH groups, it restricts the number of available precursors, because diphenylsilanediol is the only commercially available silanediol. It is however possible to reduce the optical losses through aqueous routes. This places no restrictions on the precursors, but creates the need for a very well controlled hydrolysis-condensation reaction to ensure a minimum of remaining OH. Specifically, the amount of water used in the reaction plays a major role[8]. If the amount of water is too large, not all hydrolyzed groups will be condensed and left over OH will be present. If the amount of water is too small insufficient formation of the inorganic network will occur, which leads to poor mechanical properties. The large number of left over alkoxy groups also increases the loss because of the  $\text{CH}_2$  and  $\text{CH}_3$  groups in the alkoxy functionality, which result in absorption in the NIR because of the CH stretch vibration. Most water-based sol-gel materials for waveguide applications also contain zirconium alkoxides to increase the adhesion of the material to the substrate. It is believed that the zirconium is primarily responsible for the high conductivity, and is beneficial for poling as described above. However, the presence of zirconium leads unfortunately to the absorption of water in the cured film [9] as well as to a reduction in shelf life. It can however also lead to lower losses[8]. The wide availability of silane precursors makes it easy to tailor the properties of sol-gel materials to fit the needs of the application. The chemical structure of MAPTMS as well as the structures of the other silanes used can be found

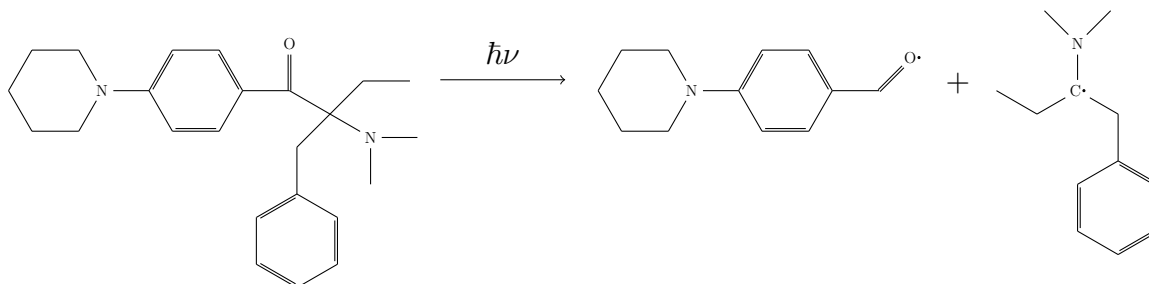


FIGURE 1.3. Decomposition of Irgacure 369 under UV-radiation

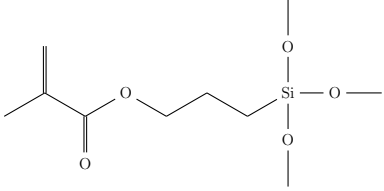
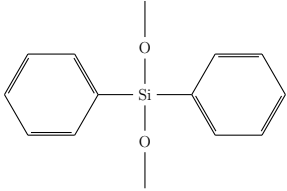
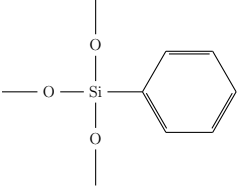
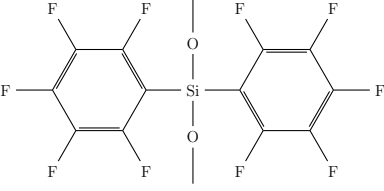
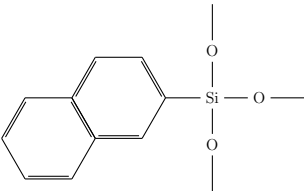
in Table 1.1.

MAPTMS contains a methacrylic group which can be polymerized under UV-radiation after the addition of a photoinitiator [10]. The photoinitiator used in this work was Irgacure 369 from Ciba. When exposed to UV radiation a bond in Irgacure 369 breaks homolytically to form two radicals (see Fig. 1.3)[11]. The carboxyl radical then starts a chain reaction to crosslink the oligomers formed during the sol-gel reaction. This leads to solid materials with a three dimensionally crosslinked network, which provides high thermal and chemical stability.

The sol-gel reactions were carried out in capped 20 ml clear vials with an electric stirrer at room temperature with hydrochloric acid as a catalyst. Details recipes can be found in Appendix A. All mixtures were stirred for 48h. After this the liberated methanol was removed by heating the vial until the mixture reached 120°C. The absorption spectra of the solvent free sols were measured using a CARY 5G UV-VIS-NIR spectrometer with 1cm thick PMMA cuvettes. Corrections for reflections at the air/PMMA interfaces are incorporated in the data. Loss measurements on cured film were performed using a liquid prism set up as described by Teng [12], for selected materials. In addition, rib waveguides were fabricated with a Karl-Sss MJB3 mask aligner and characterized using the cut-back method.

The hydrolyzation ratio (rh) is the ratio of added water to the number of hydrolyzable alkoxy groups. For every hydrolyzed alkoxy group, two alcohols are produced,

TABLE 1.1. Silane precursors used to tune the refractive index and reduce the optical loss. Naphthalene-trimethoxy-silane is a powder, so no refractive index is given.

Chemical Name	Chemical Structure	$n_D^{20}$	Benefits	Drawbacks
Methacryloxipropyl-trimethoxy-silane (MAPTMS)		1.4277	Better adhesion, photo-patterable	increases loss
Diphenyl-dimethoxy-silane (DPDMS)		1.5447	increases index, decreases loss	
Phenyl-trimethoxy-silane (PTMS)		1.4734	increases index, decreases loss	
Bispenta-fluoro-diphenyl-dimethoxy-silane (BPFDPDMS)		1.4181	lowers index, decreases loss	reduces photosensitivity
Naphthalen-trimethoxy-silane (NaphTMS)		n/a	increases index	

one in hydrolysis and one in condensation, during which the Si-O-Si bond is formed. If the condensation is carried out between a hydrolyzed and non-hydrolyzed species, the alcohol is separated directly. If the condensation is carried out between two hydrolyzed species, water instead of alcohol is formed, which can afterwards again hydrolyze an alkoxy group. The amount of water added to the synthesis determines the amount of hydrolyzation and condensation and therefore the average size of the resulting oligomers. The larger these oligomers are, the higher the viscosity of the resulting material will be. Because the higher the condensation ratio the denser the resulting network, the amount of water also influences the refractive index of the material slightly. The influence of the hydrolyzation ratio on the optical loss of the resulting materials in the telecom regime at 1550nm is of great interest. It was found, that by decreasing the hydrolyzation ratio from 0.45 (RH4) to 0.36 (RH5) the optical loss can be drastically decreased from 1.2dB/cm to 0.6dB/cm. The measured spectra can be seen in 1.4. Both systems had a molar ratio of 1:1 MAPTMS:DPDMS and used 0.1 molar hydrochloric acid as a catalyst. The reason for the strong influence of the hydrolyzation ratio on the optical loss is that that some hydrolyzed groups are not accessible for the condensation reaction as the oligomers grow around them and therefore form a protecting shell. The hydrolyzation ratio must therefore be chosen to minimize the amount of these inaccessible SiOH groups, but still large enough to result in complete hydrolysis.

The influence of the pH of the reaction mixture on the optical loss was also examined. For this synthesis, the same system as described above (1:1 MAPTMS:DPDMS) was used with a hydrolyzation ratio of 0.36. The pH was varied by using different solutions of hydrochloric acid. The lowest loss resulted from using 1M HCl, which was 0.1dB/cm lower than for 0.1M HCl and 0.5M HCl; note that the data for RH5 and RH7 lie on top of one another. The loss for the material made with 0.2M HCl is considerably higher than for the others. The reasons for this are not completely clear at this time.

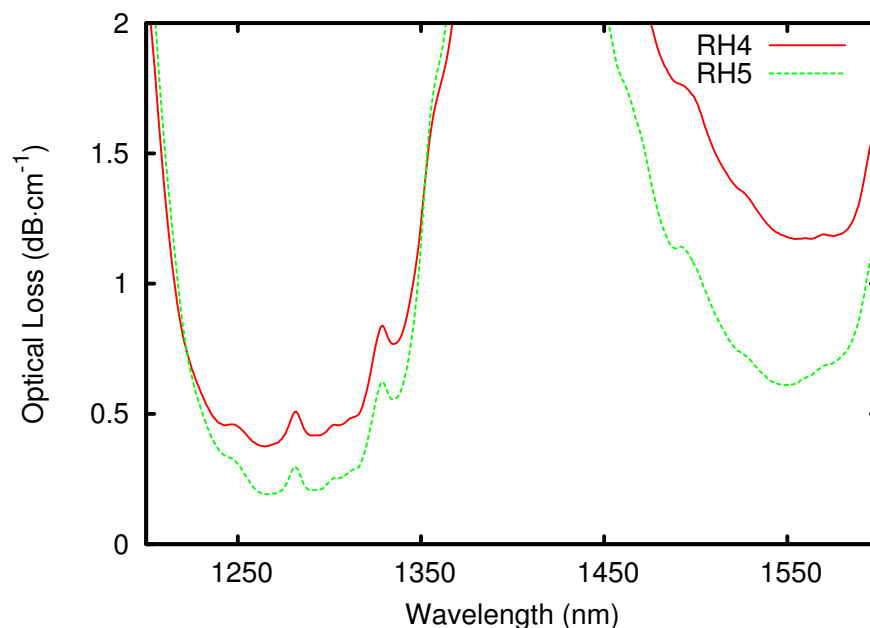


FIGURE 1.4. Absorption spectra of two example systems with hydrolyzation ratios of 0.45 and 0.36, respectively.

Since the sol-gel materials are to be used in planar optical waveguides, it is quite useful to be able to change the refractive index of the material easily, without changing the other properties drastically. With RH8 as a basis material, several ways of tuning the refractive index were explored. The most common way to tune the index of sol-gel materials is to vary the amount of zirconium (IV)-propoxide added during the synthesis. As described before, the addition of zirconium has an unfavorable influence on the optical loss of the material. An alternative method for changing the refractive index, chosen here, is to introduce silanes as index changing agents. If RH8 is chosen as the cladding material for optical waveguiding, the material used for the core must have an higher index and this was accomplished by replacing a certain fraction of MAPTMS with phenyl trimethoxy silane (PTMS). The influence of the PTMS content on the refractive index is, as expected at these low molar percentages, very linear and can be seen in Fig. 1.5 It is even possible to increase the refractive

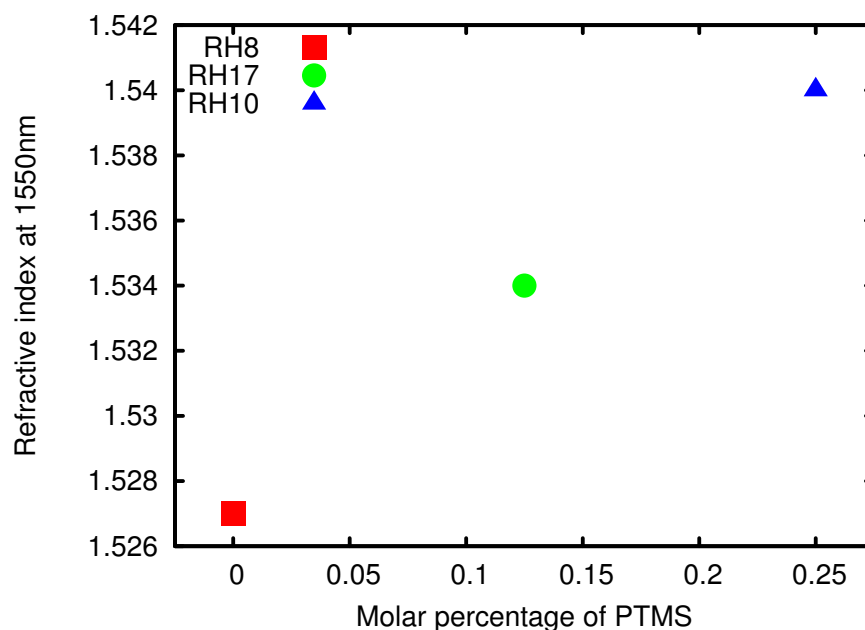


FIGURE 1.5. Refractive index vs. molar percentage of PTMS, measured in cured films.

index up to 1.562 if naphthalene trimethoxysilane (NaphTMS) is used instead of PTMS.

By using bis-pentafluoro dimethoxysilane (FDPDMS) the refractive index can also be lowered below the value for RH8. In this case the percentage of MAPTMS was kept constant and DPDMS was replaced by FDPDMS. The corresponding results can be seen in Fig. 1.6. The available refractive index range from 1.495 to 1.562 enables a great freedom in the design of devices. The optical loss values of the materials were all between 0.6 dB/cm and 0.45 dB/cm (liquid phase solvent free sols).

To confirm the optical performance of the new sol-gel material in the solid state, two measurements were carried out. For the measurement of slab waveguides, films were prepared on silicon wafers with 6 $\mu$ m of thermally grown silica. The films were then characterized in a liquid prism set up. In this set up a collimated laser beam is coupled into a film using a prism. The film is systematically translated into a liquid

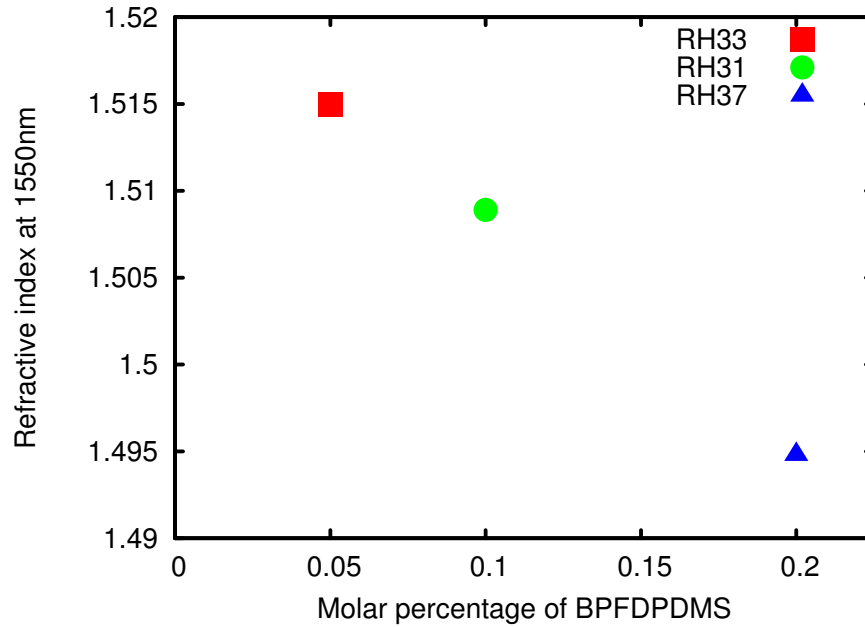


FIGURE 1.6. Refractive index vs. molar percentage of BPFDPDMS, measured in cured films.

with an index higher than that of the film, so that the light is coupled into the liquid and is then collected by a photodetector. As an example, the measurement results for RH10 are in shown in Fig. 1.7. The loss in the film was determined to be 0.68dB/cm at 1550nm. The difference between the optical loss in the liquid state (0.5 dB/cm) and in the film can be explained by defects and imperfections that develop during thin film processing.

In addition to the measurements on slab waveguides, rectangular waveguides were fabricated with RH8 as the cladding material and RH10 as the core. A cross section of an RH10 waveguide on RH8 undercladding is shown in Fig. 1.8. After the evaporation of methanol, 0.1 % of Irgacure 369 as an initiator and 10 % propylene glycol monomethyl ether acetate as a solvent were added to the RH10 sol. Prior to spin coating the wafers were cleaned in an ultrasonic bath with acetone and in an oxygen plasma chamber. The patterning was carried out using a Karl Sss MJB3 mask aligner

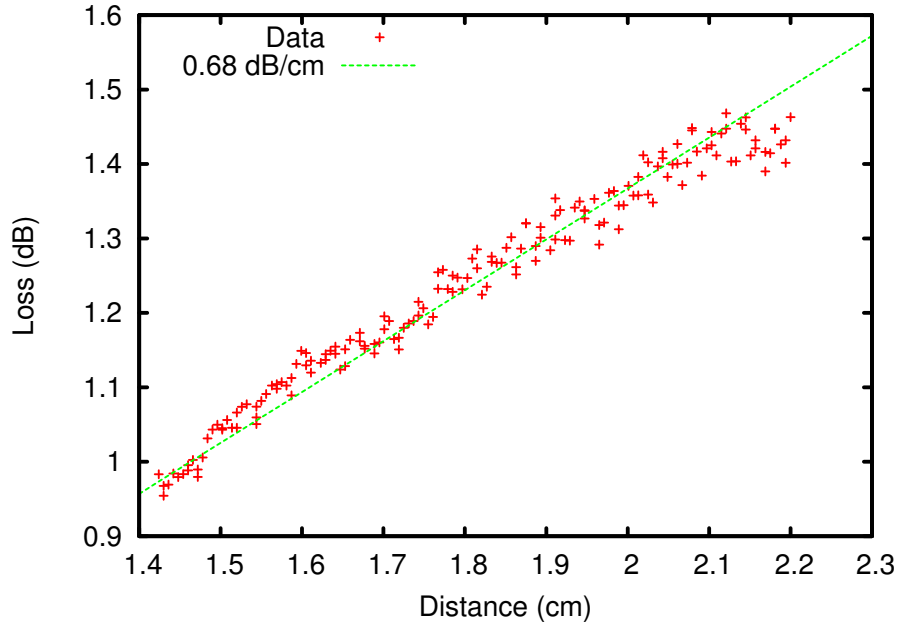


FIGURE 1.7. Optical loss data for RH 10 obtained using a liquid prism set up.

under an  $N_2$  atmosphere.

The optical loss of the fabricated waveguide devices was measured by the cutback technique. After cleaving both ends of the device, light at 1550 nm was coupled into the waveguide from an SMF-28 optical fiber. The light leaving the device was collected by a lens and focused on a detector. After cleaving off a small piece on the exit side the measurement was repeated. For every sample length eight waveguides were measured. The resulting data are shown in Fig. 1.9. The average optical loss in the waveguides was calculated to be  $0.52 \pm 0.04$  dB/cm with a coupling loss of  $1.6 \pm 0.1$  dB. This result agrees very well with the liquid state as well as the slab waveguide measurement[5]. We now discuss the electrical properties of sol-gels and factors that are critical for good poling efficiency.

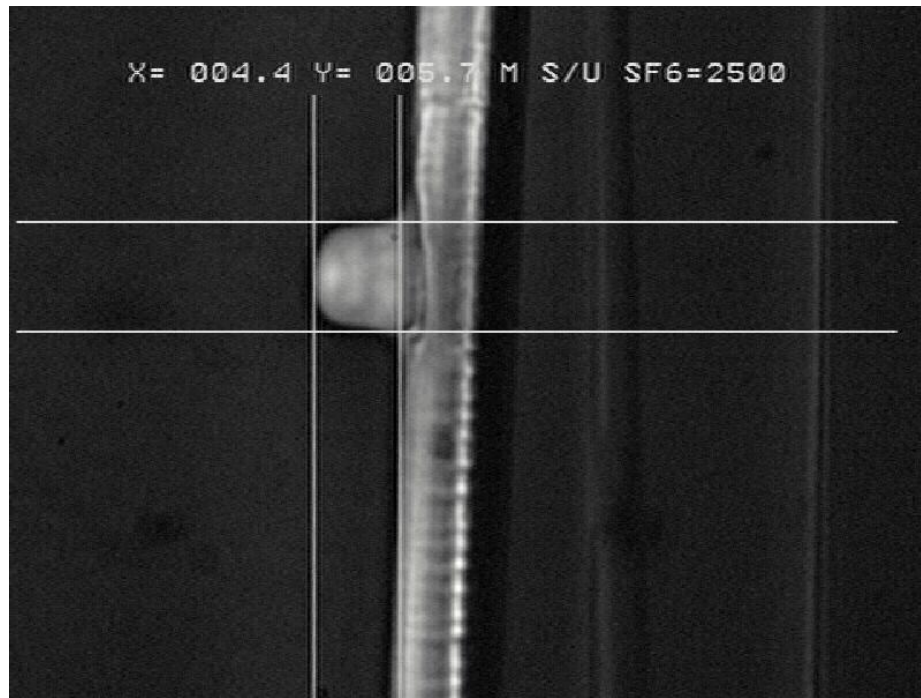


FIGURE 1.8. Cross section of an RH10 waveguide on RH8 undercladding.

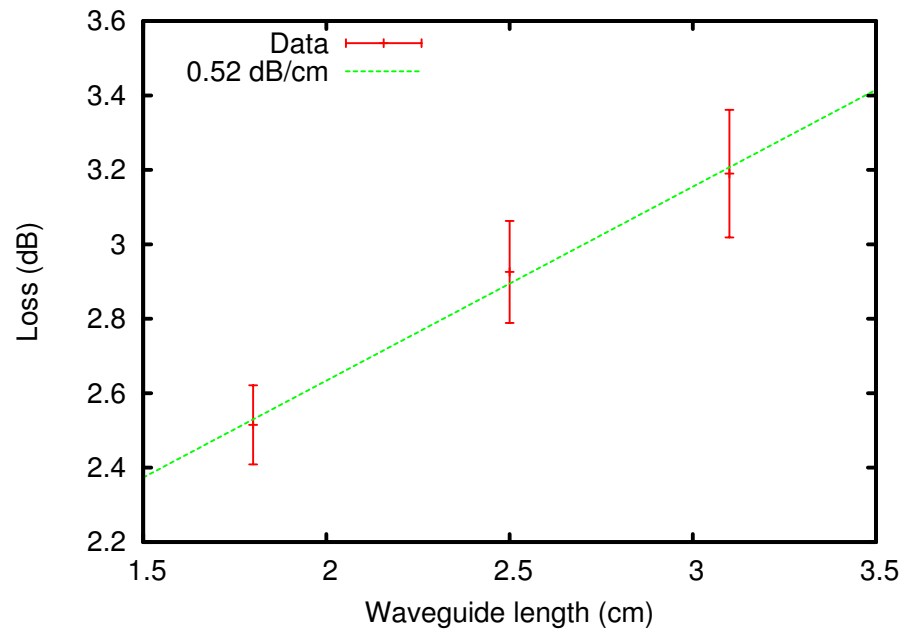


FIGURE 1.9. Loss measurement of RH 10 waveguides, with RH8 as a cladding.

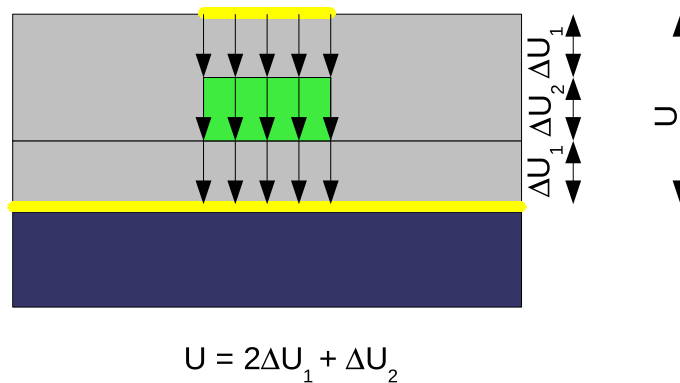


FIGURE 1.10. Voltage drop over a multilayer stack.

### 1.2.2 Electrical properties

In principle there are three critical electrical properties for a cladding material in an EO polymer modulator, namely, their dielectric loss, their dielectric constant and their conductivity during the poling process. The dielectric loss is especially important for high modulation speeds in a traveling wave electrode configuration. The dielectric loss should be low ( 0.005 or less) to reduce the attenuation of the modulation field as it passes traverses the modulator. The dielectric constant is of interest because it can help to concentrate the modulation field in the EO polymer and therefore reduce the switching voltage  $V_\pi$  . With respect to poling, the voltage drop over the cladding materials should be as small as possible so that the maximum poling field is applied to the EO polymer and optimal poling results. A schematic of a multilayer stack typical of hybrid EO polymer/sol-gel devices is shown in Fig.1.10.

The newly developed sol-gel materials discussed thus far are not suitable for this purpose as their conductivities at the poling temperature (around 150°C ) are several orders of magnitude lower than that of a typical EO polymer. Zirconium containing sol-gel materials, however, show conductivities of the same order as EO polymers. The reason for the higher conductivity is still not completely understood, but could

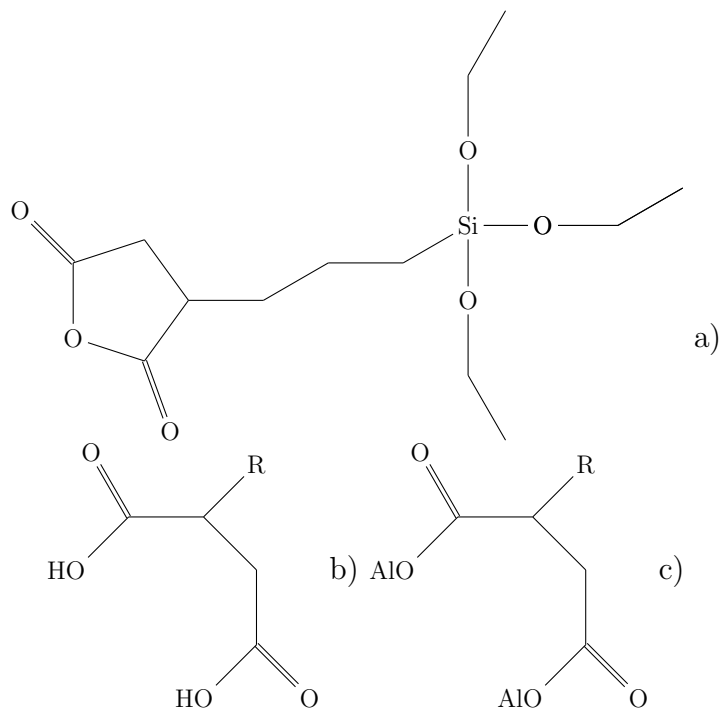


FIGURE 1.11. Structure of 3-(triethoxysilyl)-propyl succinic acid anhydride a), the di-acid b) and a di-ester c). Al stands for an alky group

be related to their high water uptake. Besides zirconium-propoxide, methacrylic acid is commonly added to sol-gel materials as a chelating agent for the zirconium. The reason for this is to reduce the reactivity of the metal by the formation of a stable complex [13]. The conductivity of sol-gel materials without any zirconium can be increased by the addition of methacrylic acid. The amount of methacrylic acid is basically limited by the reduction of film quality and adhesion that results with its addition. The maximum amount of methacrylic acid, that produced a useful material was about 3.5%. Another approach to introducing acid functionalities, is to form them in-situ during the sol-gel reaction. As a source for carboxylic acid functionality, 3-(triethoxysilyl)-propyl-succinic-acid-anhydride (SucAHTES) was chosen. The structure can be seen in Fig.1.11.

The anhydride ring can open up under acidic or basic condition to form the di-

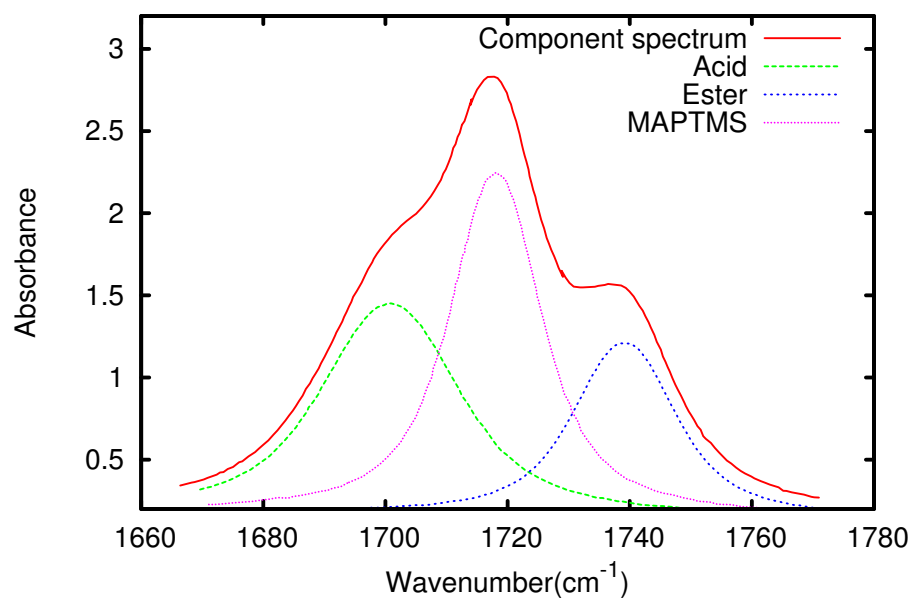


FIGURE 1.12. FT-IR spectrum of RH28-2 with deconvoluted peaks. The peaks were assigned as follows:  $1717\text{cm}^{-1}$ (MAPTMS),  $1700\text{cm}^{-1}$ (acid of SucAHTES),  $1738\text{cm}^{-1}$ (ester of SucAHTES)

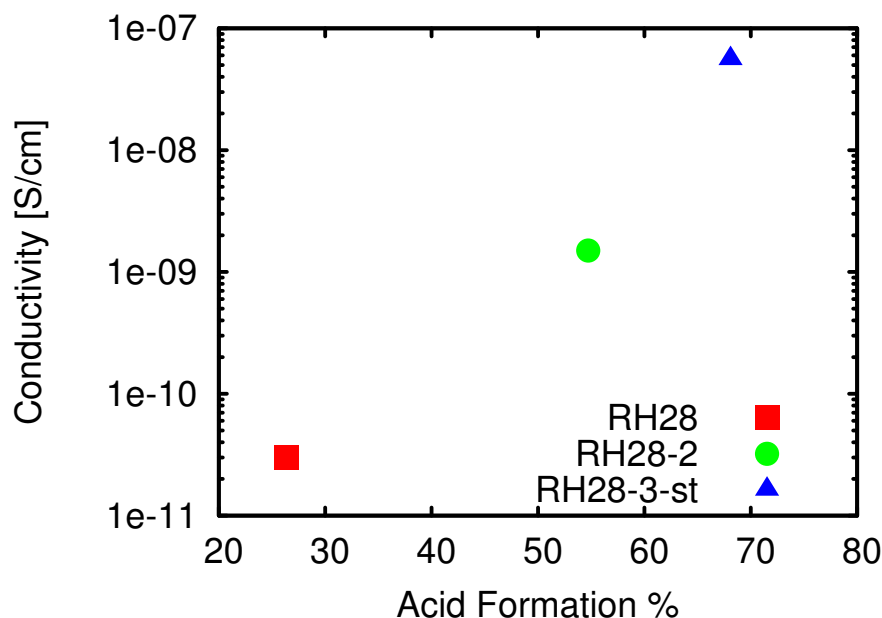


FIGURE 1.13.

acid. Another product is the ester, which can be formed from the acid stage or the anhydride stage. To minimize the formation of the ester the hydrolyzation of the anhydride and the formation of the inorganic-organic network was carried out in two stages. To reduce the concentration of methanol and ethanol from the sol gel reaction, iso-propanol as a solvent was chosen. Iso-propanol is sterically hindered and will not form esters easily. The recipe is also given in appendix A. The ester does not contain any easily detachable protons and therefore does not contribute to the conductivity. The structures of the di-acid and the a ester are also shown in Fig. 1.11. To maximize the acid yield the reaction was controlled by Fourier transform infrared spectroscopy (FT-IR). A typical FT-IR spectrum is shown in Fig. 1.12. To peaks of interest originate in carboxylic stretch vibration. The position in the spectrum gives information about the chemical environment of the carboxylic group and allows for identification of the esters and acids [14].

To measure the conductivity of the materials samples with indium tin oxide (ITO)

as a bottom electrode and gold as a top electrode were prepared. The RH28 materials were spun coated and cured by UV exposure. The electrodes were pattern by sputtering and shadowmasking. The are of the electrode was  $1.2 \text{ cm}^2$ . At an applied field of  $50V \text{ cm}^{-1}$  the samples where heated in a intergas atmosphere at approximately  $13^\circ\text{C min}^{-1}$  to  $150^\circ\text{C}$  . The current was recorded by using a pico amp meter in series with the sample. The general behavior of all samples was a steady increase in current with a slight plato around  $110^\circ\text{C}$  . The highest current was observed at  $150^\circ\text{C}$  . As the area of the electrode as well as the thickness and the applied field is known the conductivity of the material can be calculated. It should be noted that insulating materials do not generally show ohmic behavior, meaning the conductivity depends on the applied field as with some other sol-gel materials[5]. In Fig. 1.13 the conductivity of three materials with different acid formation yields is shown. It is very clear from the graph that the amount of current that is recorded dramatically increases with the amount of acid formed during the synthesis.

### 1.3 High index sol gel materials <sup>1</sup>

#### 1.3.1 Synthesis

To allow for compact waveguide devices a material with a high refractive index is desirable; silicon and silicon nitride are most commonly used for this. They are however not photopatternable and patterns need to be created by photoresist patterning and subsequent reactive ion etching. Titanium oxide is well-known for its high refractive index and has been used for this reason in the formation of sol-gel materials for optical applications quite extensively [16, 17, 18, 19]. Recently, the use of sol-gel derived titanate for photonic nanosheets has been demonstrated[20]. Due to the reactivity of the titanium alkoxides, most approaches use sol-gel polymerizations of alkoxides in the presence of chelating additives or pre-formed titanium oxide nanoparticles dispersed

---

<sup>1</sup>Taken in large parts from Himmelhuber et.al. [15]

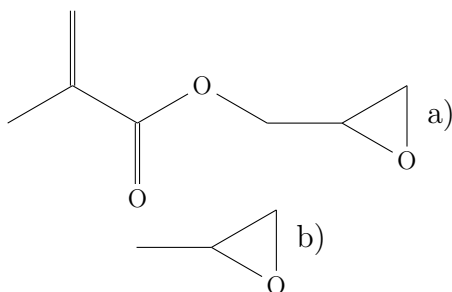


FIGURE 1.14. Structures of glycidyl methacrylate a) and propylene oxide b)

into an organic polymer matrix. Chelating agents often add undesirable properties to the materials, limiting overall control over the optical properties and often need to be removed by a high temperature baking process. In general, nanoparticle composites are known to show scattering loss at high loading and are difficult to process. Glycidyl methacrylate (GLYME) was used for the sol-gel polymerization of titanium tetrachloride, in a simple one-pot synthesis to prepare high quality thin films of organically modified titanium oxide with tunable refractive index. The refractive index of the films can be controlled by substituting some of the GLYME with propylene oxide (PO). Structures of GLYME and PO can be seen in Fig.1.14. The methacrylate functionality in GLYME allows to direct photopatterning of the obtained films and enables tunability of the refractive index at 589 nm (sodium D-line) from roughly 1.76 to 2.05. As such, the material is a strong candidate for applications in compact integrated photonics, since its high index allows for tight bends, while the index tunability provides for good coupling to optical fiber and compatibility with a wide range of other photonic materials.

The films were prepared by dissolving titanium tetrachloride (0.36 M, 99% Aldrich) in ethanol (200 proof, anhydrous, 99.5%, Aldrich). This has to be done very carefully and inside a fume hood, due to the exothermic nature of the mixing process. The mixture is shaken for 5 sec. After the mixture has cooled down to room temperature an excess of water (1.2 M) is added and the mixture is shaken again for 5 sec.

GLYME or a mixture of GLYME with propylene oxide (PO) (1.3 M) is added last. After a final vigorous shaking the mixture is aged at room temperature for a week before spinning films. By keeping the concentration of epoxide below 1.3 M, stable sols were obtained which, as pointed out above, is ordinarily difficult for titania-based sol-gels. All recipes for the prepared materials are given in Appendix A. Films were prepared by spincleaning a silicon substrate with water, acetone and 2-propanol. The sol to be spincoated is filtered through a 100nm polytetrafluoroethylene membrane syringe filter directly onto the substrate. The films are spin-coated between 1000 and 4000 RPM without a spread cycle, followed by baking for 30 sec at 80°C, for 10 min at 120°C on a hotplate and then for 18h at 150°C in an oven. Heat treatment at 150°C for 18 h evaporated the residual ethanol and the lighter by-products of the epoxide ring opening producing mechanically stable, hard, transparent, colorless films. Typical film thicknesses obtained by this process are between 70 and 200 nm. Spin curves for two different materials synthesized with either GLYME or PO can be seen in Fig.1.15. For photopatterning 2% (with respect to solid content) Irgacure 369 (Ciba) was added to the sol prior to spincoating. The film was exposed in a MJB3 mask aligner with a UV 400 filter for 1min. The power level was  $8mW/cm^2$  measured at  $365nm$ . After a post exposure bake at 80°C for 20 sec the sample was developed in a 1:4 mixture of acetone and 2-propanol.

### 1.3.2 Chemical Analysis

Propylene oxide can react to form propylene glycol, 1-chloro-2-propanol and 2-chloro-1-propanol when used as a gelation agent with a metal chloride [21]; these are shown in Fig.1.16. The boiling points of these compounds are between 133°C and 189°C at standard pressure [22, 23]. The corresponding reaction products of glycidylmethacrylate (3-chloro-2-hydroxypropyl methacrylate, boiling point 104-108°C at 5 torr [24], 2-chloro-3-hydroxypropyl methacrylate, boiling point 116-148°C at 5 torr [25] and

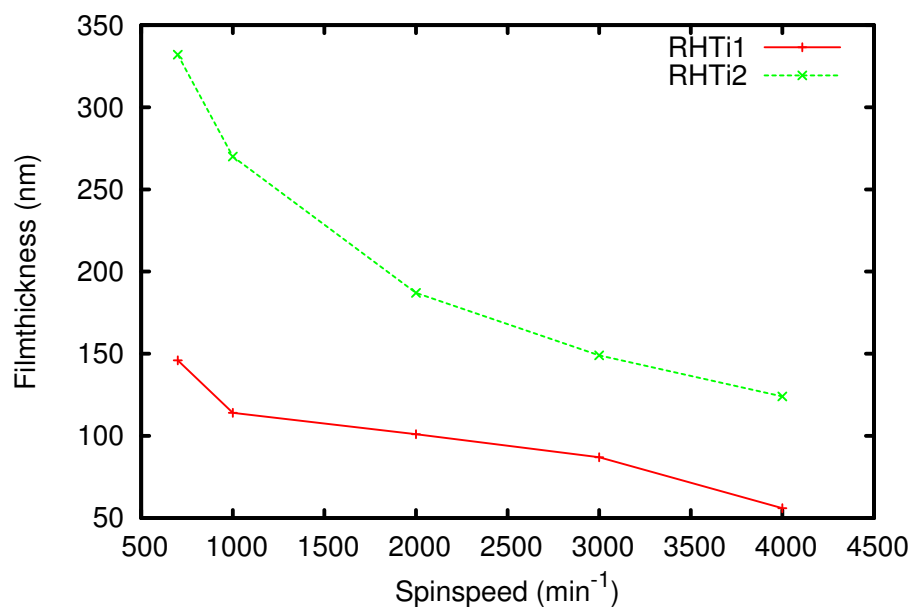


FIGURE 1.15. Spin curves for RHTi1 (containing only PO) and RHTi2 (containing only GLYME)

2,3 dihydroxypropylmethacrylate, boiling point 95-97°C at 0.05 torr for the racemate [26]) are much less volatile; the structures of these products are shown in 1.17. In addition to the high boiling points of the reaction products of GLYME, an FT-IR analysis indicated a potential coordination of the carbonyl oxygen to titanium. This is indicated by a peak in the infrared spectrum at  $1520\text{ cm}^{-1}$ . The spectra were recorded on a Thermo Electron Nicolet 6700 FT-IR spectrometer. For preparation of solid film samples the sol was drop cast onto a sodium chloride plate which was then baked in the same manner as the films for refractive index measurements. It is known that the coordination of a Lewis acid to a carbonyl oxygen can cause the absorption band to shift into this region [27]. More evidence for this coordination is that titanium oxyacetylacetonate and bis (tris- (acetylacetonato)) titanium hexachloro-titanate have both of their carbonyl oxygens coordinated to titanium and show peaks at  $1525\text{ cm}^{-1}$  and  $1534\text{ cm}^{-1}$ , respectively [28]. In addition to the coordination of the carbonyl

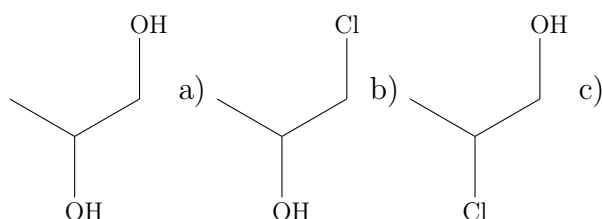


FIGURE 1.16. Structures of propylene glycol a), 1-chloro-2-propanol b) and 2-chloro-1-propanol

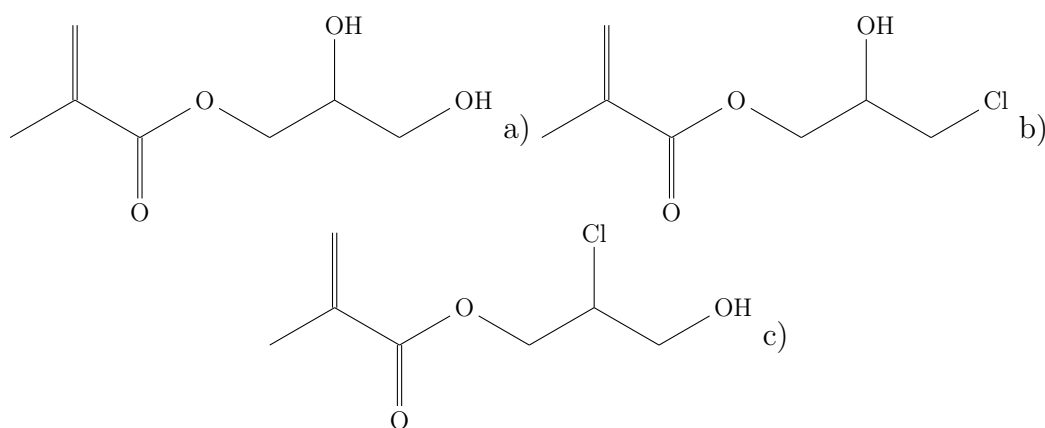


FIGURE 1.17. Structures of 2,3 dihydroxypropylmethacrylate a), 3-chloro-2-hydroxypropyl methacrylate b) and 2-chloro-3-hydroxypropyl methacrylate

group, the diol of 2,3 dihydroxypropylmethacrylate and propylene glycol also probably coordinates to the titanium oxide particles formed during the sol-gel reaction. A schematic of a titanium oxide particle with a randomly oriented organic shell is shown in Fig. 1.18.

### 1.3.3 Optical properties

Dynamic light scattering measurements showed the size of the particles in suspension to be app. between 3nm and 10nm. A typical light scattering data plot is shown in Fig. 1.19. This result indicates that if waveguides would be fabricated from the material, losses due to scattering should be minimal. An X-ray photoelectron spectroscopy (XPS) analysis of the films revealed that the percentage of carbon in the

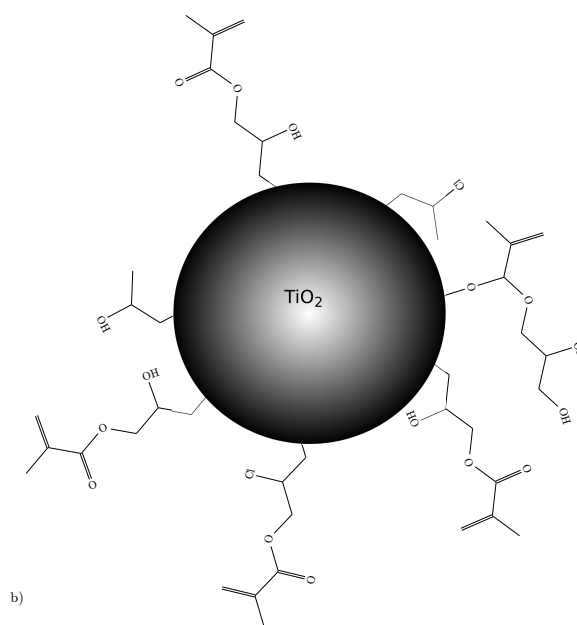


FIGURE 1.18. Particle as it might be present in the material.

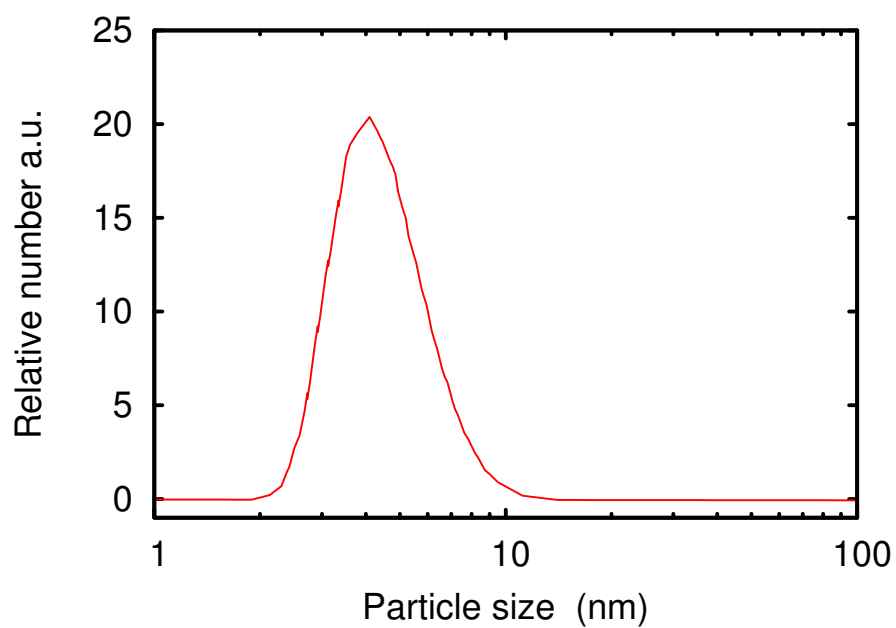


FIGURE 1.19. Particle size distribution of RHTi2 measured by dynamic light scattering.

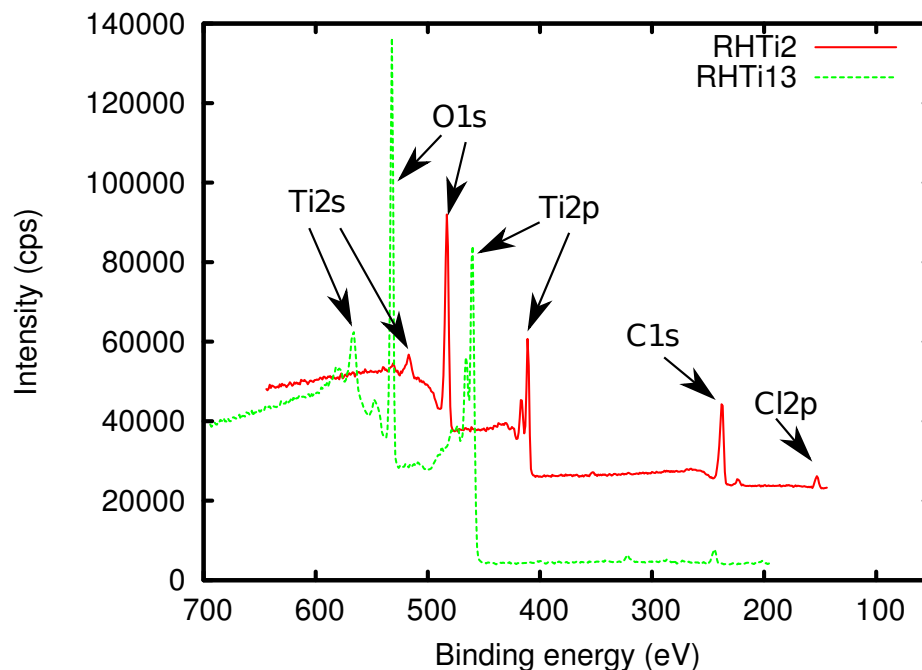


FIGURE 1.20. XPS survey spectra of a material made only with PO (RHTi13) and of one only made with GLYME(RHTi13). Peak assignments are shown in the graph. Note that the C 1s peak in the black curve is not visible at this magnification due to its small size.

final samples depends on the amount of GLYME used in the synthesis. Two typical survey spectra are shown in Fig. 1.20. Besides the expected elements, some residual Cl from GLYME reaction products was found in some samples. The area of the O 1s, Ti 2p, C 1s and if applicable of the Cl 2p peak were used for the quantitative analysis of the carbon content.

This data was correlated with optical properties of the films measured with a GSE5 spectral ellipsometer from Sopra. Ellipsometry measures the intensity and phase difference of s and p polarized light reflected from the film and the substrate. If other properties of the samples, like the optical properties of the substrate are known, this data can be used to determine a dispersion law that describes the refractive index of the film as well as the film thickness. In our case the titanium oxide films were

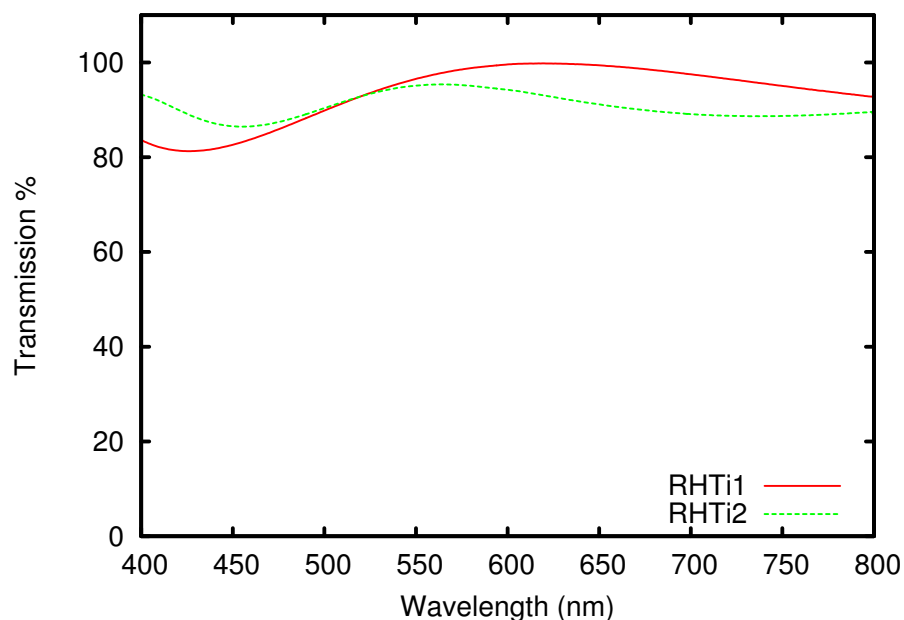


FIGURE 1.21. Transmission spectra of RHTi1 and RHTi2 measured on quartz at the wavelengths relevant for ellipsometry.

measured on silicon wafers. Every substrate was first measured blank to examine the thickness of the native oxide layer. A Sellmeier model was used to describe the real part of the dielectric function of the thin films between 400 and 800 nm. Absorption was neglected for most of the films, because the quality of the fit did not increase if absorption was included in the model. A transmission measurement of two films on quartz did not reveal any absorption between 400 and 800 nm (see Fig.1.21). The fact that the transmission is not exactly 100% is due to reflection and thin film interference.

As shown in Fig.1.22 the carbon content in the films changes linearly with the amount of GLYME used in the synthesis. For the same range (0 to app. 50% GLYME) refractive indices of the films also change approximately linearly with the GLYME concentration. If the amount of GLYME is increased further, both the carbon content and the refractive index level out. If only GLYME is used for the

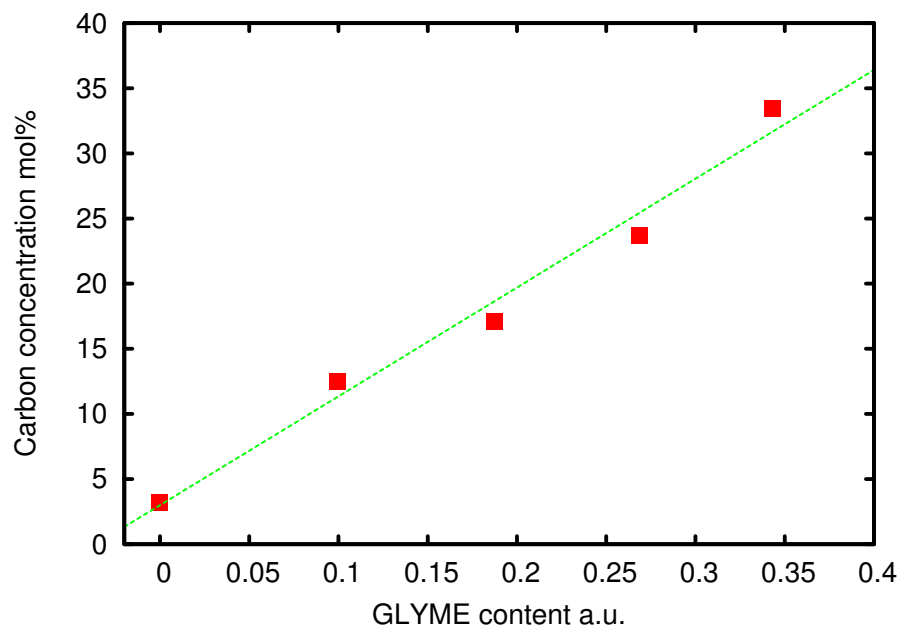


FIGURE 1.22. GLYME content versus the molar fraction of carbon in the spun film as measured by XPS.

synthesis the amount of carbon in the film is around 45 mol%. To test if the refractive indices of the materials are dependent on the epoxide used for synthesis, we compared the refractive indices of films which were made from sols synthesized with mixtures of PO and GLYME with films obtained by mixing two sols solely made from either PO or GLYME. The two sols were mixed right before spin coating to obtain PO and GLYME concentrations similar to the sols synthesized with a mixture of PO and GLYME.

The resulting refractive index data plotted versus the GLYME content are shown in Fig. 1.23. The x-axis indicates the amount of GLYME in the sol. For the materials synthesized with a mixture of GLYME and PO a value on the x-axis of for example 0.75 indicates that 75% of the total molar epoxy concentration in the sol comes from GLYME and 25% is from PO. In the case of films made from the mixtures of two sols, the x-axis values indicate the mixing ratio of the two sols. Again, 0.75 on

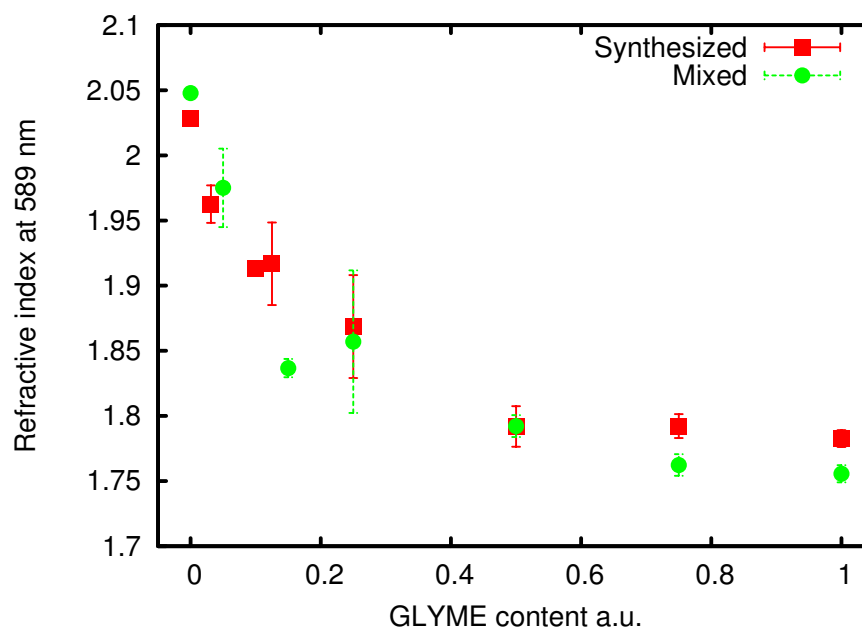


FIGURE 1.23. Refractive index at the D-line of sodium of RHTi samples with varying amount of GLYME.

the x-axis means that 75% of a GLYME sol and 25% of a PO sol were used. The red squares represent data from sols synthesized with mixtures of GLYME and PO. The concentration of epoxy groups, water and  $\text{TiCl}_4$  was kept constant for all the materials. The green circles represent the films obtained from mixtures of two sols, synthesized separately with either PO or GLYME. The error bars show the standard error of the mean. Every data point represents at least 4 samples, with synthesis performed in sets of three. The change of refractive index for the synthesized and the mixed samples follows the same shape and no significant offset can be seen, indicating that the influence of GLYME during the synthesis is negligible and that GLYME is just as suitable as PO in the epoxy initiated formation of titanium oxide. This also implies that the coordination of the reaction products of GLYME to the titanium oxide particles happens during annealing and not during the particle formation.

Overall, this data shows the facility of this method for preparing films with re-

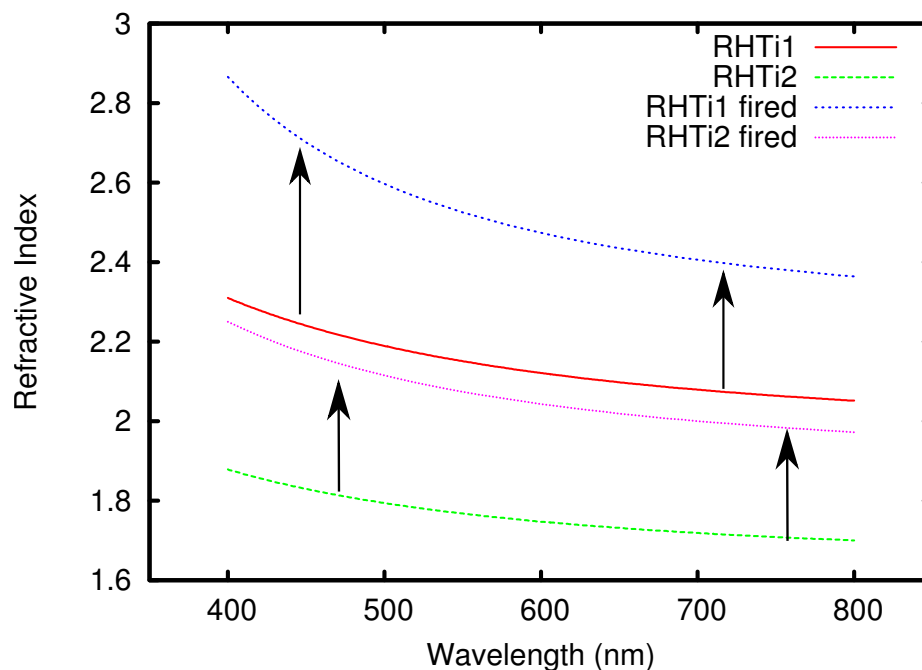


FIGURE 1.24. Change of the refractive index of RHTi1 and RHTi2 due to heat treatment at 550°C .

refractive indices between 1.76 to 2.05. The dispersion behavior of the materials is in the expected range for titanium oxide containing mixtures. An extrapolation of the fitted Sellmeier function into the near IR suggests that the refractive index of the materials at 1550nm is between 1.7 and 1.9. Annealing the materials at 550°C for 10 h increases the refractive indices of the films by approximately 0.3 at 800nm; as shown in Fig.1.24. This heat treatment also induces a phase transition from amorphous titania to anatase, as X-ray diffraction(XRD) analysis showed. The domain size in the anatase was estimated to be around 3 nm. Due to its nano crystalline nature scattering in waveguides due to grain boundaries should also be very small. An XRD spectrum of an RHTi1 films processed normally and one fired at 550°C for 1h is shown in Fig. 1.25.

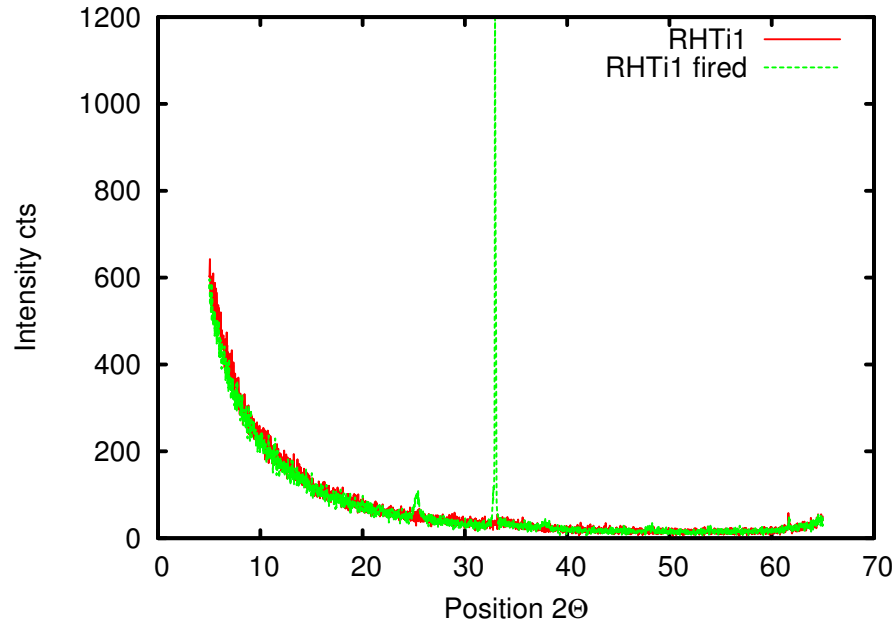


FIGURE 1.25. X-ray diffraction measurement for an amorphous and crystalline RHTi1 film.

### 1.3.4 Physical properties

The methacrylate group in glycidylmethacrylate can be photopolymerized, allowing us to demonstrate photopatterning. By adding Irgacure 369 as a photoinitiator and exposing through a photomask we were able to create a 120nm high pattern. The smallest feature on the mask was 4μm. A surface profile scan over a 300μm wide feature is shown in Fig.1.26. Because of their high and adjustable index as well as their lithographic processability these materials can be very useful for the fabrication of compact photonics devices and structures such as couplers, ring resonators and gratings. By having control over the refractive index in this region it is possible to fine tune the transmission band of a waveguide Bragg grating, without changing the structure. This has a big cost benefit as the the photo mask or nano imprint stamp used to fabricate the structure does not have to be redesigned.

To investigate the nanoscale distribution of titanium oxide in the composites,

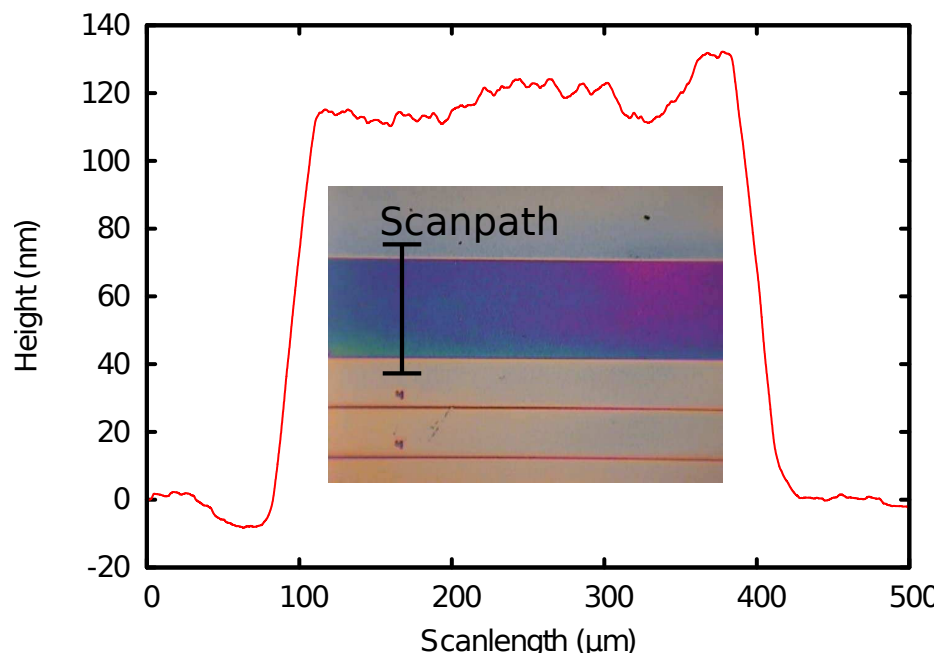


FIGURE 1.26. Surface profile scan over a 300m wide structure. The image in the middle shows a microscope picture of the sample.

subsurface dielectric imaging of thin films was pursued using electrostatic force microscopy (EFM). EFM experiments were realized using a double pass method: during the first pass, the topographic image was acquired in normal tapping mode using a Veeco Innova atomic force microscope equipped with a Nanodrive controller. The second pass raised the conductive atomic force microscope (AFM) probe above the sample to a fixed distance and re-scanned the surface with a bias voltage applied between the probe and AFM stage, following the previously recorded topography to maintain a constant tip-sample separation. The amplitude and phase of the probe during the second pass were recorded as EFM signals. Two types of conductive AFM probes were used. One is a conventional platinum-iridium coated AFM probe (Bruker SCM-PIT). The other is a high aspect ratio antimony doped highly conducting Si probe (Bruker, FESP) with apex diameter  $< 8\text{nm}$ , resonance frequency at 77.25 kHz and force constant of 2.5 N/m. The bias voltage applied to the AFM

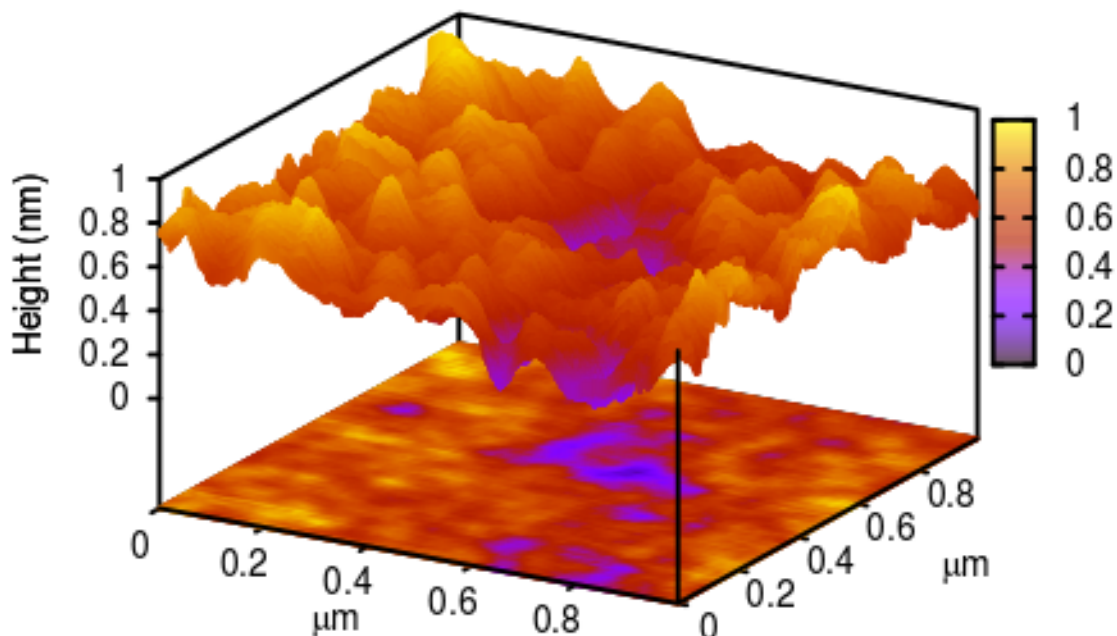


FIGURE 1.27. Topographic image of an RHTi7 film measured by AFM

probes ranged from 10 to +10 V and the lift height was varied from 10 to 100 nm. The images reported here were recorded using FESP tips with a lift height of  $18 \pm 2$  nm and a bias voltage of -5V applied through the substrate. The AFM height image in Fig.1.27 shows a relatively smooth surface with an rms roughness of 0.6nm; the AFM phase image, which reflects the relative hardness of the material, indicates nanophase separation on the surface, possibly between titanium oxide (hard - dark) and organic rich (soft - white) domains. The average domain size is less than 20nm.

The EFM phase image (Fig.1.29) shows the subsurface distribution of the domains with the darker parts indicating domains with higher dielectric constant. The dark areas account for approximately 46% of the area, which corresponds to 46 wt%. Both images show a homogenous distribution of organic and inorganic domains without

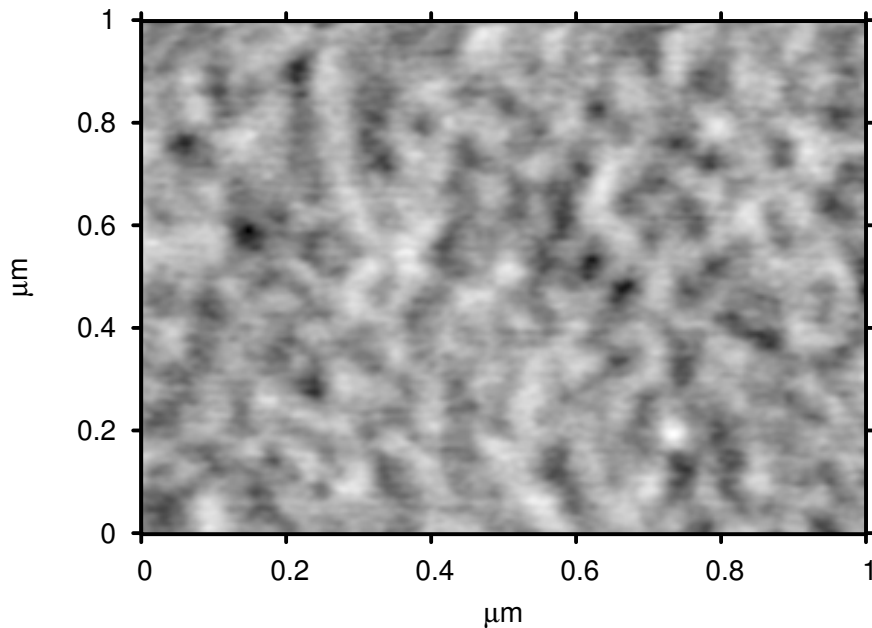


FIGURE 1.28. AFM phase image of an RHTi7 film representing the relative hardness of the surface.

large clusters. The relative static dielectric constants of the two phases were estimated from a series of EFM images recorded under changing biasing voltages based on the methodology of Zhao [29] and Riedel [30]. Relative static dielectric constants calculated from the EFM phase map show a nearly bimodal distribution of organic rich domains at  $7.5 \pm 3$  and titanium oxide rich ones at  $68 \pm 12$ . The distribution of the dielectric constant is shown in Fig. 1.30. For comparison, the static dielectric constants for rutile are 170 and 86 for the ordinary and extraordinary axis [31] and 3.6 for poly methacrylate [32], respectively.

The high dielectric constant of the presumably inorganic phase of the RHTi materials also make them good candidates for electric field concentration applications. For this a high dielectric constant material resides between the electrode and the EO polymer in a electro optic modulator. Because the D-field has to be continuous and  $D = \epsilon E$  the electric field in the region with a lower dielectric constant is enhanced.

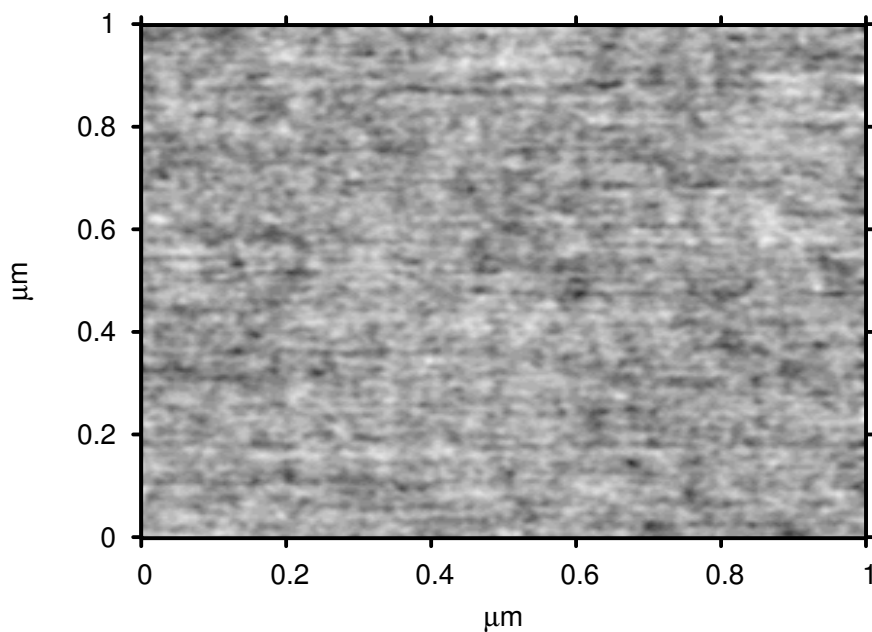


FIGURE 1.29. EFM phase image of a RHTi7 film representing the relative static dielectric constant.

## 1.4 Summary

Sol gel materials with wide variety of optical and electrical properties have been developed. Materials with tunable refractive indices from below 1.4 to above 2 have been shown. A method for increasing the conductivity of a sol gel material has been developed. An epoxy based method for making high index, high dielectric constant thin films has been demonstrated; the static dielectric constant of the developed material is around 80.

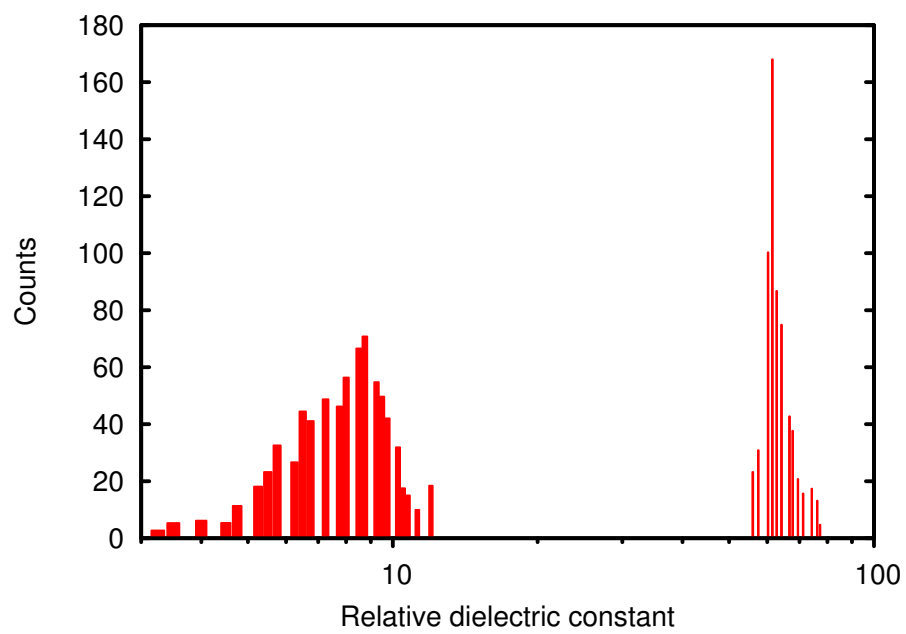


FIGURE 1.30. Distribution of relative dielectric constants computed from EFM image.

## Chapter 2

# ELECTRO OPTIC POLYMER CHARACTERIZATION <sup>1</sup>

## 2.1 Introduction

While sol-gel materials clearly have an attractive property set as the passive cladding materials in electro-optic (EO) modulators, of course an EO active material is needed. Characterization of EO active materials, more specifically EO polymers is important as it allows for poling optimization and test device characterization without going through the complete fabrication cycle of a waveguide modulator device.

EO guest-host polymers consist of an amorphous polymer matrix and a dye with a permanent dipole moment. These mixtures are most often prepared in solution and then spun cast into films; after spin casting the dye molecules are oriented randomly. During the poling process a high electric field is applied and the film is heated up close to the glass transition temperature of the polymer. The polar dye molecules align along the electric field lines creating a non-centrosymmetric order which is frozen in as the material is returned to room temperature with the field still applied. As such the now poled polymer has a non-zero  $\chi^{(2)}$  tensor and exhibits the electro-optic effect, usually quantified in terms of the Pockels coefficient. A second order nonlinear optical material can also be used to create second harmonic light, and the intensity of the generated second harmonic depends quadratically on the  $d$  coefficients which can be directly related to the Pockels coefficient [34].

Poled polymer films, which exhibit second order nonlinear optical properties have been investigated for over 20 years [35]. Optical polymers are, aside from technically irrelevant single crystal examples, amorphous materials. To show second-order nonlinearities some sort of order has to be introduced into the system, such as via the

---

<sup>1</sup>Taken in large parts from Himmelhuber et.al. [33]

poling process described above[36]. To characterize these poled polymer films it is possible to measure the Pockels coefficients or the  $d$  coefficients.

Second harmonic generation in non centrosymmetric media and the Pockels effect are based on the same physical principles. The nomenclature for describing these phenomena are quite different however. In this section the relation between the non linear coefficients ( $d_{xy}$ ) and the Pockels coefficients ( $r_{xy}$ ) will be discussed. For this we will first go briefly through the description of second order nonlinearities and indicate the origin of the  $d$  coefficients. Then we will discuss the origin of the linear EO effect and show how the  $r$  coefficients are used in this context. This discussion will show that once the similarity of these two described effects are clear, it is possible to describe them in relation to each other. This is particularly useful for determining the Pockels coefficients through second harmonic generation measurements.

## 2.2 Second order non-linearities

In general, the polarization of a material can be described as

$$\mathbf{P}(\mathbf{r}, t) = \epsilon_0 \boldsymbol{\chi}(\mathbf{r}, t) \mathbf{E}(\mathbf{r}, t) \quad (2.1)$$

which is often written as the series

$$\mathbf{P}(\mathbf{r}, t) = \epsilon_0 (\boldsymbol{\chi}^{(1)}(\mathbf{r}, t) \mathbf{E}(\mathbf{r}, t) + \boldsymbol{\chi}^{(2)}(\mathbf{r}, t) \mathbf{E}^2(\mathbf{r}, t) + \boldsymbol{\chi}^{(3)}(\mathbf{r}, t) \mathbf{E}^3(\mathbf{r}, t) + \dots) \quad (2.2)$$

The linear susceptibility is a second rank tensor (a three by three matrix), the second order susceptibility is a third rank tensor (three by three by three matrix). In general the higher orders of the  $E$  field can be of different frequency and amplitude ( $E^3 = E_1 E_2 E_3$ ). If one only looks at the case where all term above second order are ignored and only one field is incident on the material. This is the simplest case for second harmonic generation and the second order polarizability can be written as

TABLE 2.1. Index contraction

jk	11	22	33	23=32	31=13	12=21
m	1	2	3	4	5	6

$$\mathbf{P}^{(2)}(2\omega) = \epsilon_0 \chi^{(2)}_{ijk}(-2\omega, \omega, \omega) \mathbf{E}(\omega) \mathbf{E}(\omega) \quad (2.3)$$

In the case of negligible absorption losses and dispersion Kleinman symmetry is valid. This means that

$$\chi_{ijk} = \chi_{jik}^{(2)} = \chi_{ikj}^{(2)} = \chi_{jki}^{(2)} = \chi_{kji}^{(2)} = \chi_{kij}^{(2)} \quad (2.4)$$

To emphasize this special case one can make the substitution  $\chi_{ijk}^{(2)} = \mathbf{d}_{ijk}$ . Due to its symmetry  $\mathbf{d}_{ijk}$  can be reduced to a six by three matrix without any loss on information. This is called index contraction. If we call the six by three matrix  $\mathbf{d}_{lm}$  then the transformation can be done with  $i = l$  as shown in Table 2.1.

The polarization can now be written as

$$\begin{bmatrix} P_x^{(2)}(2\omega) \\ P_y^{(2)}(2\omega) \\ P_z^{(2)}(2\omega) \end{bmatrix} = \epsilon_0 \begin{bmatrix} d_{11} & d_{12} & d_{13} & d_{14} & d_{15} & d_{16} \\ d_{21} & d_{22} & d_{23} & d_{24} & d_{25} & d_{26} \\ d_{31} & d_{32} & d_{33} & d_{34} & d_{35} & d_{36} \end{bmatrix} \begin{bmatrix} E_x^2 \\ E_y^2 \\ E_z^2 \\ 2E_z E_y \\ 2E_x E_y \\ 2E_x E_z \end{bmatrix} \quad (2.5)$$

This is a very interesting result, as it states that there are cases where two polarizations (e.g.  $E_x$  and  $E_z$ ) are needed to create a linearly polarized second harmonic wave. This should be emphasized, because in the discussion about the electro optic effect something similar will occur.

### 2.3 The electro optic effect

The electro-optic (EO) effect is the change in the refractive index of a material if a low frequency (compared to light) electric field is applied. If the change of refractive index changes linearly with the applied field it is called the ‘‘Pockels Effect’’ after Friedrich Pockels, A German physicist who lived from 1865 to 1913. The EO effect can be understood as a special case of a second order nonlinearity. If in (2.3) the frequency of one of the incident fields is set to 0

$$\mathbf{P}^{(2)}(\omega) = \epsilon_0 \chi^{(2)}_{ijk}(-\omega, \omega, 0) \mathbf{E}(\omega) \mathbf{E}(0) \quad (2.6)$$

results.

Using the same arguments as before it is easy to rewrite (2.6) as:

$$\mathbf{P}^{(2)}(\omega) = \epsilon_0 \mathbf{d}_{lm} \mathbf{E}(\omega) \mathbf{E}(0) \quad (2.7)$$

Because the EO effect is just a special case of the second order nonlinearity it is clear that only anisotropic media can exhibit it. In this respect a relationship that is similar to (2.5) can be developed, which connects the change in refractive index to the applied field and the Pockels coefficients. The relationship between the E field and the displacement field D in a lossless anisotropic material can be written as

$$\begin{aligned} D_x & \\ D_y & \\ D_z & \end{aligned} = \epsilon_0 \begin{bmatrix} \epsilon_x & 0 & 0 \\ 0 & \epsilon_y & 0 \\ 0 & 0 & \epsilon_z \end{bmatrix} \begin{bmatrix} E_x \\ E_y \\ E_z \end{bmatrix}. \quad (2.8)$$

From this the energy density per unit volume is

$$U = \frac{1}{2} \begin{bmatrix} D_x & D_y & D_z \end{bmatrix} \begin{bmatrix} E_x \\ E_y \\ E_z \end{bmatrix} = \frac{1}{2} \epsilon_0 \begin{bmatrix} \epsilon_x E_x & \epsilon_y E_y & \epsilon_z E_x \end{bmatrix} \begin{bmatrix} E_x \\ E_y \\ E_z \end{bmatrix} \quad (2.9)$$

$$= \frac{1}{2\epsilon_0} \epsilon_o^2 (\epsilon_x E_x E_x + \epsilon_y E_y E_y + \epsilon_z E_z E_z). \quad (2.10)$$

With  $D_i = \epsilon_0 \epsilon_i E_i$  2.11 becomes

$$U = \frac{1}{2\epsilon_0} \epsilon_o (D_x E_x + D_y E_y + D_z E_z) \quad (2.11)$$

$$= \frac{1}{2\epsilon_0} \left( \frac{D_x^2}{\epsilon_x} + \frac{D_y^2}{\epsilon_y} + \frac{D_z^2}{\epsilon_z} \right) \quad (2.12)$$

This already has the well known form of the index ellipsoid; the final transformation only requires two more substitutions, namely  $\epsilon_i = n_i^2$  and  $i = \sqrt{\frac{1}{2\epsilon_0 U}} D_i$  with  $i = x, y$  and  $z$  yielding

$$1 = \frac{x^2}{n_x^2} + \frac{y^2}{n_y^2} + \frac{z^2}{n_z^2} \quad (2.13)$$

This is the index ellipsoid for the case that the axes of the ellipsoid are aligned with the principle axis system; the more general mathematical expression for the index ellipsoid is given by

$$1 = \frac{1}{n_1^2} x^2 + \frac{1}{n_2^2} y^2 + \frac{1}{n_3^2} z^2 + 2 \frac{1}{n_4^2} yz + 2 \frac{1}{n_5^2} xz + 2 \frac{1}{n_6^2} xy \quad (2.14)$$

This curve defines the refractive indices that light of any given polarization experiences when its travels through the medium in any given direction. Now lets explore what happens to the ellipsoid if an electric field is applied. (2.9) written in a more general case, where the principle axis system is not aligned with the major and minor polarization axes of the material is

$$U = \frac{1}{2}\epsilon_0 \begin{bmatrix} E_x \\ E_y \\ E_z \end{bmatrix} \begin{bmatrix} \epsilon_{11} & \epsilon_{12} & \epsilon_{13} \\ \epsilon_{21} & \epsilon_{22} & \epsilon_{23} \\ \epsilon_{31} & \epsilon_{32} & \epsilon_{33} \end{bmatrix} \begin{bmatrix} E_x \\ E_y \\ E_z \end{bmatrix}. \quad (2.15)$$

Performing the matrix multiplication and recognizing that the  $\epsilon$  matrix must be symmetric gives

$$U = \frac{1}{2}\epsilon_0^2(\epsilon_{11}E_xE_x + \epsilon_{22}E_yE_y + \epsilon_{33}E_zE_z + 2\epsilon_{13}E_zE_x + 2\epsilon_{12}E_xE_y + 2\epsilon_{23}E_zE_y) \quad (2.16)$$

Comparing (2.16) to (2.14) and following the same steps that lead from (2.9) to (2.14) it is clear that

$$\left(\frac{1}{n_1^2} = \frac{1}{\epsilon_{11}}\right), \left(\frac{1}{n_2^2} = \frac{1}{\epsilon_{22}}\right), \left(\frac{1}{n_3^2} = \frac{1}{\epsilon_{33}}\right), \\ \left(\frac{1}{n_4^2} = \frac{1}{\epsilon_{23}}\right), \left(\frac{1}{n_5^2} = \frac{1}{\epsilon_{13}}\right) \text{ and } \left(\frac{1}{n_6^2} = \frac{1}{\epsilon_{12}}\right)$$

Knowing that the relative permittivity  $\epsilon = (1 + \chi)$  and that  $\chi$  can be described as a power series of the form  $\chi = \chi^{(1)} + \chi^{(2)}E + \chi^{(3)}E^2 + \dots$  it is viable to assume that the same should be possible for  $1/\epsilon$ . Following this argument we can write

$$\frac{1}{\epsilon_{ij}} = \frac{1}{\epsilon_{ij}^{(0)}} + \frac{\mathbf{E}}{\epsilon_{ijk}^{(1)}} + \frac{\mathbf{E}\mathbf{E}}{\epsilon_{ijkl}^{(2)}} + \dots \quad (2.17)$$

Introducing the impermeability tensor  $\eta$  which is the inverse of  $\epsilon$  results in

$$\eta_{ij} = \eta_{ij}^{(0)} + \mathbf{E}r_{ijk}^{(1)} + \dots \quad (2.18)$$

If  $\epsilon$  is lossless and dispersionless in the wavelength regime of interest (no dispersion in the bandwidth of a laser), it is therefore real and symmetric. This means that the third rank tensor  $r_{ijk}$  can be contracted into a three by six matrix just like in (2.5).

TABLE 2.2. Index contraction

ij	11	22	33	23=32	31=13	12=21
1	1	2	3	4	5	6

The only reason that the  $d$  tensor is a six by three matrix and  $r$  is three by six, is convention; the electro-optic effect was observed and studied for practically a century before nonlinear optics developed around the invention of the laser. With  $k = m$  and the other conventions adopted in Table 2.2 this matrix can be used to determine the first correction for the refractive index in response to an applied electric field:

$$\begin{bmatrix} \Delta(1/n_1^2) \\ \Delta(1/n_2^2) \\ \Delta(1/n_3^2) \\ \Delta(1/n_4^2) \\ \Delta(1/n_5^2) \\ \Delta(1/n_6^2) \end{bmatrix} = \begin{bmatrix} r_{11} & r_{12} & r_{13} \\ r_{21} & r_{22} & r_{23} \\ r_{31} & r_{32} & r_{33} \\ r_{41} & r_{42} & r_{43} \\ r_{51} & r_{52} & r_{53} \\ r_{61} & r_{62} & r_{63} \end{bmatrix} \begin{bmatrix} E_x^2 \\ E_y^2 \\ E_z^2 \end{bmatrix} \quad (2.19)$$

Applying this correction to the index ellipsoid ( 2.14), as well as relabeling the refractive indices and refractive index changes gives, in the principle axis system

$$\begin{aligned}
 1 = & \left( \frac{1}{n_{x0}^2} + r_{11}E_x + r_{12}E_y + r_{13}E_z \right) x^2 + \left( \frac{1}{n_{y0}^2} + r_{21}E_x + r_{22}E_y + r_{23}E_z \right) y^2 \\
 & + \left( \frac{1}{n_{z0}^2} + r_{31}E_x + r_{32}E_y + r_{33}E_z \right) z^2 + 2(r_{41}E_x + r_{42}E_y + r_{43}E_z)yz \\
 & + 2(r_{51}E_x + r_{52}E_y + r_{53}E_z)xz + 2(r_{61}E_x + r_{62}E_y + r_{63}E_z)xy \quad (2.20)
 \end{aligned}$$

For most real materials many of the Pockels coefficients are in fact 0 and it unusual to apply an electric field along more than one axis. For example, a material used in many EO modulators is lithium niobate . For lithium niobate all  $r$  coefficients but

$r_{13}, r_{33}, r_{22}, r_{42}$  are 0. When a field is applied along the  $z$  axis the above formula reduces to

$$1 = \left( \frac{1}{n_{x0}^2} + r_{13}E_z \right) x^2 + \left( \frac{1}{n_{y0}^2} \right) y^2 + \left( \frac{1}{n_{z0}^2} + r_{33}E_z \right) z^2. \quad (2.21)$$

From the index ellipsoid it can be deduced that  $\frac{1}{n_x^2} = \frac{1}{n_{x0}^2} + r_{13}E_z$  and therefore  $n_x = \left( \frac{1}{n_{x0}^2} + r_{13}E_z \right)^{-\frac{1}{2}}$ . Because  $r_{13}E_z$  can be assumed to be  $\ll 1$  a Taylor expansion can be used to get

$$n_x = n_{x0}^3 - \frac{1}{2} \left( \frac{1}{n_{x0}^3} + 0 \right)^{-3.5} r_{13}E_z \quad (2.22)$$

$$= n_{x0} - \frac{1}{2} n_{x0}^3 r_{13} E_z \quad (2.23)$$

and

$$n_x = n_{x0} - \frac{1}{2} n_{x0}^3 r_{13} E_z \quad (2.24)$$

## 2.4 The relation between $r$ and $d$

In the case of a applied static electric field (DC) (2.5) for the second order polarization becomes:

$$\begin{bmatrix} P_x^{(2)}(\omega) \\ P_y^{(2)}(\omega) \\ P_z^{(2)}(\omega) \end{bmatrix} = 2\epsilon_0 \begin{bmatrix} d_{11} & d_{12} & d_{13} & d_{14} & d_{15} & d_{16} \\ d_{21} & d_{22} & d_{23} & d_{24} & d_{25} & d_{26} \\ d_{31} & d_{32} & d_{33} & d_{34} & d_{35} & d_{36} \end{bmatrix} \begin{bmatrix} E_x(\omega)E_x^{DC} \\ E_y(\omega)E_y^{DC} \\ E_z(\omega)E_z^{DC} \\ E_z^{DC}E_y(\omega) + E_y^{DC}E_z(\omega) \\ E_x^{DC}E_z(\omega) + E_z^{DC}E_x(\omega) \\ E_x^{DC}E_y(\omega) + E_y^{DC}E_x(\omega) \end{bmatrix} \quad (2.25)$$

The total polarization can be written as

$$\mathbf{P}(\omega) = \mathbf{P}^{(1)}(\omega) + \mathbf{P}^{(2)}(\omega) \quad (2.26)$$

$$= \epsilon_0 \chi^{(1)} \mathbf{E}(\omega) + 2d \mathbf{E}^{DC} \mathbf{E}(\omega) \quad (2.27)$$

$$= \epsilon_0 (\chi^{(1)} + 2d \mathbf{E}^{DC}) \mathbf{E}(\omega) \quad (2.28)$$

$$\cdot \quad (2.29)$$

With  $P = \epsilon_0 \chi E$  and  $n^2 = 1 + \chi$  a scalar relationship between  $n$  and  $d$  can be written as

$$n^2 = 1 + \chi^{(1)} + 2dE^{DC} = n_0^2 + \Delta n^2 \quad (2.30)$$

To show which elements of  $d$  go with which components of  $E^{DC}$  the components of (2.25) have to simply be written out. Note that only one component of  $P$  is shown here, but writing down the others is straightforward.

$$\begin{aligned} P_x^{(2)}(\omega) &= 2\epsilon_0 E_x(\omega) (d_{11} E_x^{DC} + d_{16} E_y^{DC} + d_{15} E_z^{DC}) \\ &\quad + 2\epsilon_0 E_y(\omega) (d_{16} E_x^{DC} + d_{12} E_y^{DC} + d_{14} E_z^{DC}) \\ &\quad + 2\epsilon_0 E_z(\omega) (d_{15} E_x^{DC} + d_{14} E_y^{DC} + d_{13} E_z^{DC}) \end{aligned} \quad (2.31)$$

By using the argument that lead from (2.26) to (2.30), expressions can be written that relate the change in refractive index to the applied electric field and  $d$ .

$$\begin{aligned} \Delta n_x^2 &= 2(E_x^{DC} (d_{11} + d_{15} + d_{16}) + E_y^{DC} (d_{12} + d_{14} + d_{16}) \\ &\quad + E_z^{DC} (d_{15} + d_{14} + d_{13})) \end{aligned} \quad (2.32)$$

$$\begin{aligned} \Delta n_y^2 &= 2(E_x^{DC} (d_{21} + d_{25} + d_{26}) + E_y^{DC} (d_{22} + d_{24} + d_{26}) \\ &\quad + E_z^{DC} (d_{25} + d_{24} + d_{23})) \end{aligned} \quad (2.33)$$

$$\Delta n_z^2 = 2(E_x^{DC}(d_{31} + d_{35} + d_{36}) + E_y^{DC}(d_{32} + d_{34} + d_{36}) + E_z^{DC}(d_{35} + d_{34} + d_{33})) \quad (2.34)$$

For real materials like lithium niobate (all but  $r_{13}, r_{33}, r_{22}, r_{42}$  are 0) these expressions are simplified dramatically. In this case, applying a field along the z-axis will change the refractive indices along the z and the x axes. If the light is polarized in the z-direction (which, in modulators, is the most common) all  $d_{lm}$  coefficients with  $m = 1, 2, 5, 4, 6$  will vanish because they will not contribute to  $P^{(2)}$  (see (2.31)). Therefore, (2.32) and (2.34) are reduced to  $\Delta n_x^2 = E_z^{DC} d_{13}$  and  $\Delta n_z^2 = E_z^{DC} d_{33}$ . Using a Taylor expansion together with (2.31) this can be written as

$$n_x = n_{x0} + d_{13} \frac{E_z^{DC}}{n_{x0}} \quad (2.35)$$

$$n_z = n_{z0} + d_{33} \frac{E_z^{DC}}{n_{z0}}. \quad (2.36)$$

Comparing (2.35) and (2.36) with (2.22) and (2.24) it is easy to find that

$$d_{13} = \frac{1}{2} n_{x0}^4 r_{13} \quad (2.37)$$

$$d_{33} = \frac{1}{2} n_{x0}^4 r_{33} \quad (2.38)$$

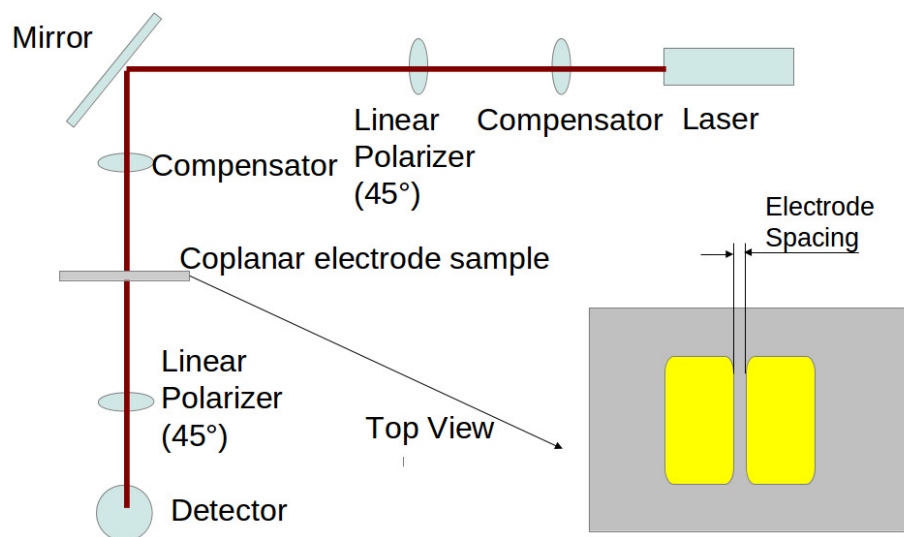
This relation is much simpler than those commonly used in the literature [34], but performs well. In Table 2.3 measured  $d_{13}$  values are compared with calculated ones. One set is calculated from (2.38), while the measured  $d_{13}$  values are from Goodson et.al. [34].

## 2.5 $r_{33}$ measurements in a transmission setup

For the  $r_{33}$  measurements the coplanar poled transparent samples were illuminated with 1340nm light polarized at  $45^\circ$  to the direction of the poling field. An AC signal of

TABLE 2.3. Calculated and measured  $d_{13}$  values for different chromophor loadings.

Loading (wt%)	$r_{13}$ measured ( $\text{pmV}^{-1}$ )	$d_{13}$ measured ( $\text{pmV}^{-1}$ )	$d_{13}$ calculated (Goodson)	$d_{13}$ calculated (Himmelhuber)
4.9	0.11	0.26	0.24	0.27
10	0.18	0.55	0.41	0.45
14.8	0.38	1.11	1.01	0.97
21	0.53	1.31	1.24	1.38
24	0.61	1.45	1.43	1.63

FIGURE 2.1. Schematic of the transmission  $r_{33}$  setup

1kHz frequency and 33.5V RMS amplitude was applied to the electrodes. The phase difference between the  $p$  and  $s$  components of the transmitted beam changes due to the electro optic effect and by measuring the change of intensity after a second polarizer oriented at  $45^\circ$  to the poling field direction,  $r_{33}$  can be calculated. The electrodes of the samples were large enough to act as an aperture for the laser beam, so all collected light has to go through the poled part of the polymer. A schematic of the measurement setup is shown in Figure 2.1. This method was first described by Nahata et.al. [37]. The electrode spacing was varied between 10 and  $20\mu\text{m}$ . Metalization was performed in a electron beam evaporator from Denton Vacuum Systems. For more details see Appendix C. The EO polymer SEO100 is commercially available from Soluxra LLC and was processed according to the provided documentation. After the EO polymer was dried over night in vacuum at  $80^\circ$  a  $15\mu\text{m}$  thick layer of sol gel buffer material [5] was spun on top of the calibration samples to prevent dielectric breakdown during poling. Poling fields varied between 50 and  $125\text{ V}/\mu\text{m}$ , depending on the electrode spacing.

A schematic of the analyzed samples is shown in Fig. 2.2. The two images on the top show the cross section view of the electrodes used for poling. The bottom two images show the top view of the samples. The zoomed in image shows approximately the region that would be visible in the multiphoton microscope. The SH signal only originates in the poled area between the electrodes.

## 2.6 Second harmonic microscopy

Second-harmonic microscopy has been used to map the Pockels coefficients of poled polymer films [38] and poled silica waveguides [39] qualitatively in the past. Quantitative measurements of the  $d$  coefficients to characterize EO-polymers have been performed in transmission, as this allows for inline calibration to a material with a known  $d$  coefficient like urea [40]. Nonlinear optical microscopy in reflection allows

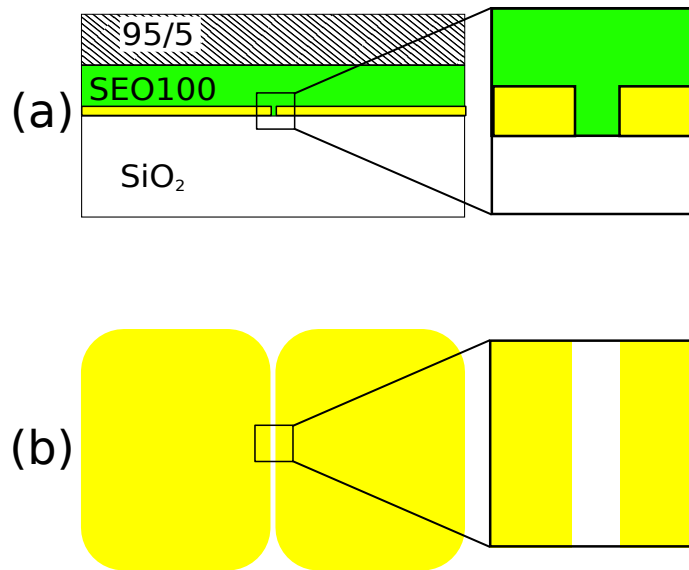


FIGURE 2.2. Cross section of coplanar samples (a) and top view of the gold electrodes (b). The right hand side shows a zoom in of the area of interest.

for a large variety of substrates, but is difficult to calibrate, due to multiple reflections and the limited availability of suitable thin films with known nonlinear optical properties. Some work has been done to numerically describe nonlinear optical microscopes for biological applications [41], but the usefulness of this work for thin film characterization is limited.

A method for measuring and mapping the Pockels coefficient of poled EO polymer films with a multiphoton microscope is described.

The multiphoton imaging measurement system is shown in Fig. 2.3. The excitation laser is a compact femtosecond (fs) fiber laser mode-locked with a carbon nanotube saturable absorber (CNT SA) developed by Prof. Khan Kieu [42]. The laser operates near 1560nm which is an important wavelength for fiber optic communication systems. The input 150 fs laser beam is raster-scanned over the sample using a 2D galvo scanner system. The beam is relayed and expanded with a scan lens and a tube lens arranged in a telescopic scheme. The back aperture of the objective is fully

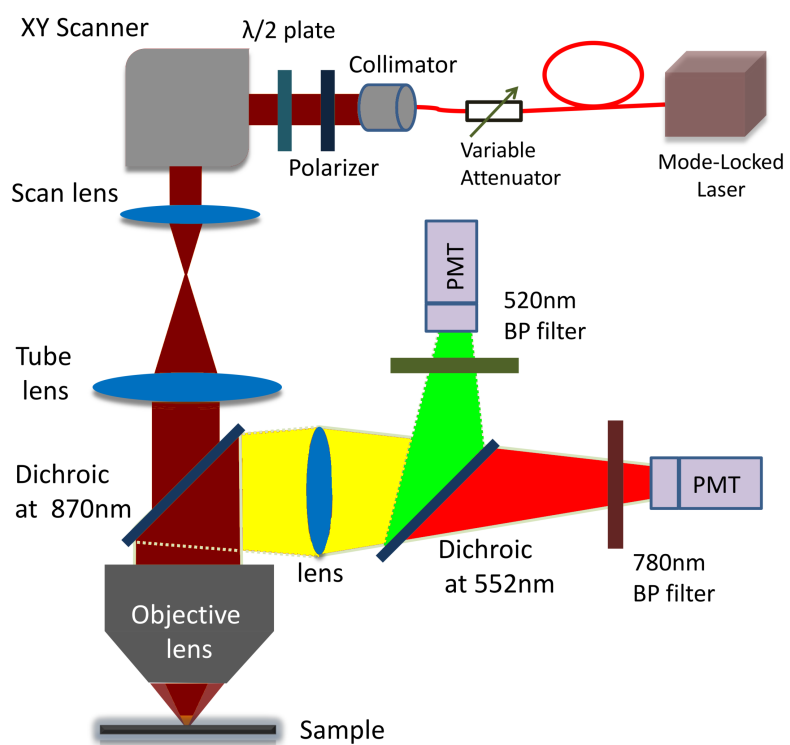


FIGURE 2.3. Schematic of the multiple-photon imaging system

illuminated to make use of the full NA and create the smallest possible laser spot size on the sample. The generated second and third harmonic signals (SHG and THG) are detected simultaneously using two highly sensitive photomultiplier tubes (PMTs) through a couple of dichroic beam splitters and laser filters. A narrow bandpass filter ( $\sim 20\text{nm}$  FWHM bandwidth) is used before each of the PMTs to detect the SHG ( $\sim 780\text{nm}$ ) and THG ( $\sim 520\text{nm}$ ) generated from the laser focal spot. The sample is moved along the  $z$  direction in combination with the galvo-scanner to quickly create 3D images showing maps of the second and third order optical non linearities of the sample. A more detailed description of the microscope setup was published recently [43]. The power variation of the SHG due to laser defocus during scanning in the region of interest was below 20% and was the same for all measured samples.

In Fig. 2.4 the recorded images from a coplanar poled polymer film on  $\text{SiO}_2$  can be seen. The acquisition frame rate was about 1Hz. The left image shows the composite image of the second (SH) and the third harmonic (TH). The image in the middle shows only the SH; it is clear that the SH only appears in the poled region. On top of the gold electrodes we see a very strong TH signal. The reason for this is probably the high reflectivity of gold at  $1560\text{nm}$  (0.98) and  $520\text{nm}$  (0.6) compared to silica (0.032 at  $1560\text{nm}$  and 0.035 at  $520\text{nm}$ ). The enhancement was observed on poled as well as unpoled films and was approximately 70 fold. The strong third harmonic signal localized on the electrodes allowed us to select the area between the electrodes for quantitative determination of the second-harmonic signal very precisely by using the image analysis software Fiji. The second harmonic signal was measured at multiple areas on every sample with the measurement region being  $250\ \mu\text{m}$  by  $250\ \mu\text{m}$ . The variation in second harmonic signal strength from area to area was below 10%. The laser power was checked prior to every microscope measurement and adjusted to be between 1.2 and 1.26mW average power with a pulse duration of 150ps and a repetition rate of 50MHz. The displayed data is corrected for the power level for each measurement. At every position the sample was moved though the focus of

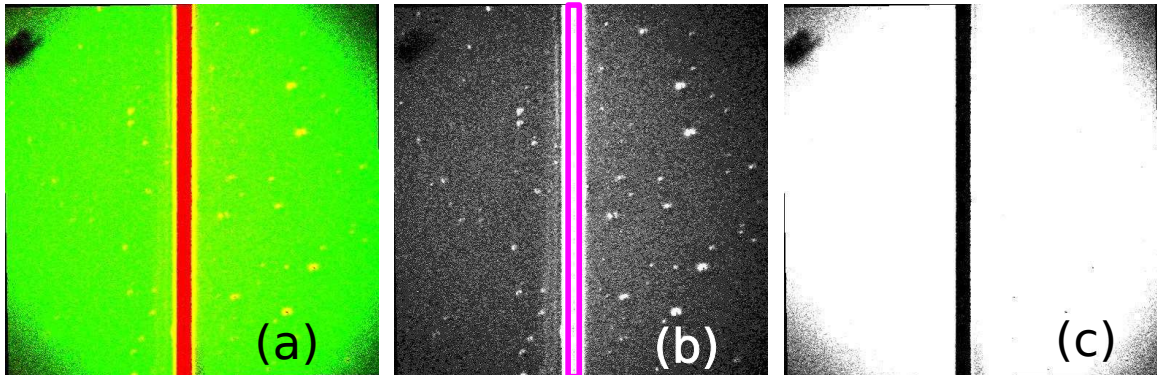


FIGURE 2.4. (a):Composite of SH(red) and TH(green), (b): SH in the poled region, (c):TH from on top of the gold electrodes. The purple box in (b) indicates the region in which the quantitative SHG data was collected.

the microscope on an automated stage to find the position with the highest intensity. The polarization of the fundamental was adjusted to give the highest SH signal, thus being polarized along the poling axis. The polarization control also allowed us to separately probe  $r_{33}$  and  $r_{13}$ . The calculated tensor ratio was three, as expected for a guest host polymer lacking specific chromophore/polymer interactions. As a function of the polarization angle  $\alpha$  of the fundamental, the intensity of the SH given by

$$I = Cr_{33}^2 \sin^4(\alpha + B) + Cr_{13}^2 \cos^4(\alpha + B). \quad (2.39)$$

Where  $C$  is a proportionality factor  $r_{33}$  and  $r_{13}$  are the Pockels coefficients, and  $B$  represents an offset factor. In Fig. 2.5 the intensity of the SH signal is shown over the polarization angle. The data was fitted with (2.39), with the green line representing the first term and the blue line the second one.

## 2.7 Analysis

The intensity of the second-harmonic signal for multiple samples was compared with  $r_{33}$  measurements from the same samples. Fig. 2.6 shows the ratio of the measured

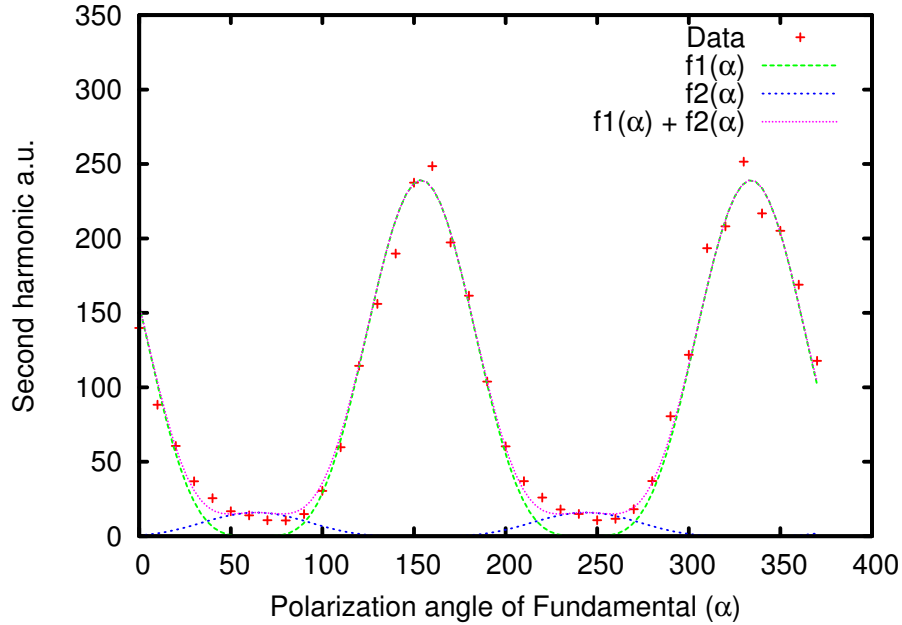


FIGURE 2.5. SH signal as a function of the linear polarization angle of the fundamental.

$r_{33}$  value to the square root of the second harmonic signal. The green line indicates the average of 28.3, the standard error of the mean was 1.3. Note that  $r_{33}$  was measured at 1340nm, but the fundamental for the second harmonic generation was at 1560nm. The Pockels coefficient at a given wavelength however can be estimated from the known coefficient at another wavelength if the nearest absorption maximum of the material is strong and isolated and the refractive index at the two wavelengths is known [44]. The graph in Fig. 2.6 incorporates this correction. The absorption maximum of the chromophore in the tested EO polymer (SEO100) is at 856nm and the Pockels coefficient at 1560nm is estimated to be a factor of 0.83 smaller than that at 1340nm.

The average value of the ratio of the second harmonic signal to the  $r_{33}$  coefficient was then used to estimate  $r_{33}$  of a coplanar poled polymer film on a silicon on insulator (SOI) wafer. A silicon waveguide was placed between the electrodes, which can act as

TABLE 2.4. Complex refractive indices of the thin film stack materials at relevant wavelengths. Ellipsometric measurements were performed on a GSE 5 spectroscopic ellipsometer from Sopra between 400 and 800nm. The EO polymer film was poled on an indium thin oxide (ITO) coated glass substrate with gold as the top electrode. The film was characterized by a Teng-Man measurement and at a  $r_{33}$  coefficient of 130 pm/V. The given refractive indices are for light polarized along the poling axis. For ellipsometry a uniaxial model was used with a Sellmeier dispersion law and two absorption peaks around 865 nm and 520nm. The prism coupler was a Metricon 2010 model with lasers at 532, 633, 816, 1305 and 1554nm. Transmission measurements were performed on a Varian Cary 5000. Alphabetic (lowercase)

$\lambda$ (nm)	SEO100			SiO <sub>2</sub> [45]			Si [46]			95/5	
	$n_r$	$n_i$		$n_r$	$n_i$		$n_r$	$n_i$		$n_r^a$	$n_i^e$
1560	1.710 <sup>a</sup>	$< 10^{-5}$ <sup>c</sup>		1.444	$< 10^{-6}$		3.475	$1.121 \times 10^{-6}$		1.484	$< 2 \times 10^{-5}$
1340	1.757 <sup>a</sup>	n/a <sup>d</sup>		1.446	$< 10^{-6}$		3.504	$1.335 \times 10^{-6}$		1.486	$< 10^{-5}$
780	1.490 <sup>b</sup>	0.181 <sup>b</sup>		1.454	$< 10^{-6}$		3.709	$7.479 \times 10^{-3}$		1.490	$< 10^{-5}$

<sup>a</sup>estimated by prism coupling at relevant wavelengths and consecutive Sellmeier regression.  $\pm 0.001$

<sup>b</sup>measured by ellipsometry.  $2\sigma$  for all fitted parameters was below 15%

<sup>c</sup>estimated from waveguide losses (approximately 2 dB/cm).

<sup>d</sup>Thin film transmission measurements show no absorption at this wavelength.

<sup>e</sup>Estimated from liquid state transmission measurements in a 1 cm thick cuvette cell. The value at 1560nm is most likely to high due to residual methanol.

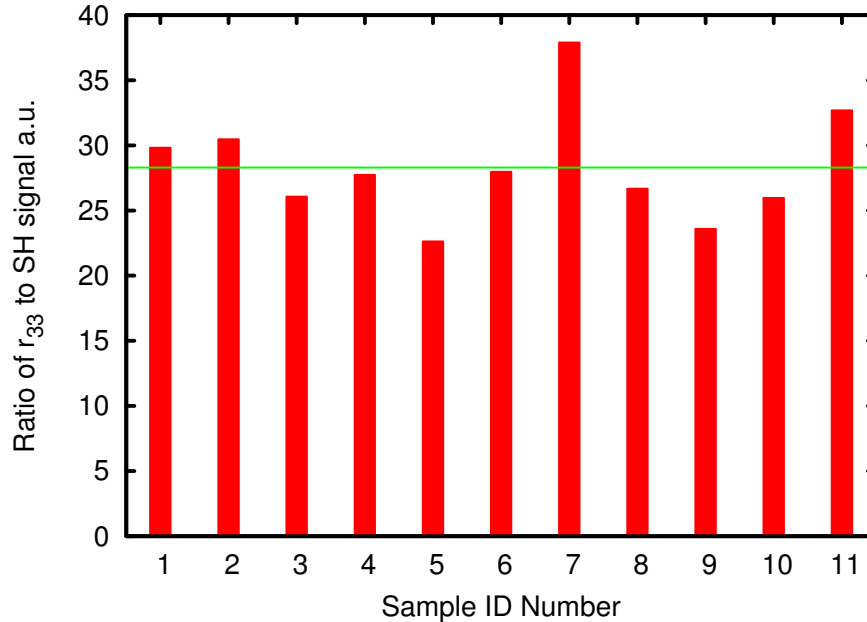


FIGURE 2.6. Ratio of the measured  $r_{33}$  to the square root of the second harmonic.

a phase modulator when an EO polymer cladding is present. A detailed description and analysis of the phase modulator device is published elsewhere [47]. Because the samples used to calibrate the second-harmonic signal to the Pockels coefficient have different reflecting interfaces than the phase modulator sample, the ratio determined from Fig. 2.6 can not simply be used to calculate the Pockels coefficient of the EO polymer layer on the SOI wafer. As the microscope employs a tightly focused Gaussian beam, we can approximately treat the reflection effects through simple addition of reflected intensities. A schematic of the two structures is shown in Fig. 2.7. Because the quantitative SHG data is only collected between the electrodes, the metal does not play a role in the reflection calculation. Here F0 is the fundamental at 1560nm entering the multilayer stack, F1 represents the amount of light entering the EO layer, F2 is reflected from the EO/silica interface and F3 is reflected from the silica/silicon interface and reenters the EO layer. S1 is the second harmonic generated from F1, S1' is the reflected SH from the EO/silica interface. S1\*' is the reflection of S1\* on

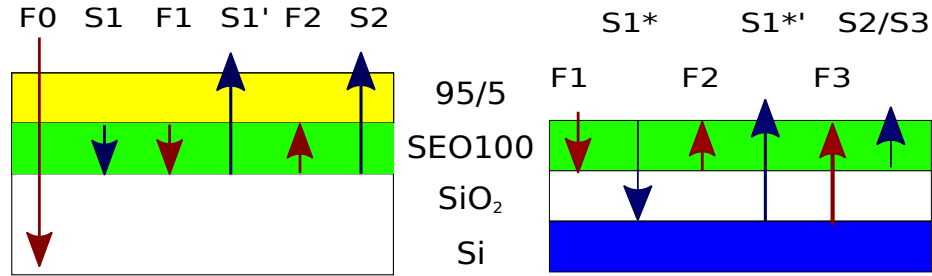


FIGURE 2.7. Schematic of the multilayer stacks of the calibration samples(left) and silicon wafer with a silica layer(right). For reflection calculations only the area between the electrodes (see Fig. 2.2) is considered.

the silica/silicon interface, which is the residual amount of S1 after the EO/silica interface. S2 is generated backwards by F2 and S3 is generated backwards from F3. As the microscope operates in reflection, only reflected or backward generated SH is collected. All additional reflections, for example the EO/sol gel interface reflection of S2' are omitted for clarity in the schematic, but included in the calculations.

To estimate the amount of reflected light from the interfaces the well-known Fresnel formula for normal incidence ( $R = \left| \frac{n_1 - n_2}{n_1 + n_2} \right|^2$ ) was used as well as the more general ones for p and s polarized light as a Gaussian beam outside of the focal spot has a angular beam cone. The largest angular spread was calculated to be  $16^\circ$ . For a focused beam the plane of incidence is the surface of the beam cone and for linearly polarized light half of the light will be s-polarized with respect to the plane of incidence and half will be p-polarized. Complex refractive indices were used for the reflection calculation because SEO100 and silicon have non-negligible absorption at the second harmonic. The refractive indices at relevant wavelengths are shown in Table 2.4. The fundamental light is tightly focused and therefore the SH will also undergo Gaussian beam spread. The EO-silica interface is the same for the reference samples and the device sample and the amount of collected light from this reflection should be the same. Therefore the Gaussian beam spread only needs to be considered for S1\*', F3 and S3. Knowing the NA of the objective (0.6) the beam waist can easily be calcu-

lated as  $w_0 = \frac{\lambda}{\pi NA}$ . The beams pass through the SiO<sub>2</sub> twice so the beam width after the reflection on the silica/silicon interface is  $w = \sqrt{w_0^2(1 + (\frac{z}{z_0})^2)}$ , where  $z$  is twice the silica thickness and  $z_0 = \pi \frac{w_0^2}{\lambda}$ . The thickness of the SiO<sub>2</sub> layer influences the degree to which the reflected fundamental is spread before reentering the EO layer. This is important because the amount of backwards created SH depends quadratically on the intensity of F3. The amount of reflected SH (S1\*) that is lost due to beam spread also depends on the SiO<sub>2</sub> thickness. In Table 2.5 the correction factor (C) is shown for different silica thicknesses. Values for simple normal incidence calculations as well as for the case when the angle of the beam cone is incorporated are shown. Note that because the reflections for s and p polarized light counteract each other the difference between the average of p and s polarized light and the normal incidence calculations is minimal. Matlab/Octave code for the calculations are incorporated in Appendix B. The sol-gel layer acts as a weak anti reflective coating and causes around 2% more fundamental to enter the EO layer and approximately 1% more SH to be collected. A sample with a 1 $\mu$ m thick SiO<sub>2</sub> layer and a Pockels coefficient of the EO film of 132 pm/V [47] at 1550nm was characterized by second harmonic microscopy and the calculated  $r_{33}$  value was 112 pm/V. A sample with a 6 $\mu$ m thick silica layer showed a  $r_{33}$  value of around 160 pm/V, which is in good agreement with samples poled under similar conditions and characterized either by the transmission measurement mentioned earlier or by a regular Teng-Man method[48].

## 2.8 Summary

A simple relationship between the  $d$  and  $r$  coefficients has been developed and a novel method for characterizing coplanar poled polymer films has been developed. Coplanar poled EO polymer films are important for device structures that do not allow for a microstrip electrode design such as silicon/polymer hybrid devices.

TABLE 2.5. Calculated correction factors with which the second harmonic signal from poled EO polymer on silica on silicon must be multiplied to be comparable with films on plain silica.

SiO <sub>2</sub> ( $\mu\text{m}$ )	0.5	1	2	3	4	5	6
C - normal	0.0144	0.0403	0.135	0.265	0.395	0.508	0.598
C - p	0.0142	0.0391	0.129	0.251	0.376	0.486	0.576
C - s	0.0146	0.0416	0.142	0.279	0.414	0.528	0.616

## Chapter 3

# ELECTRO OPTIC MODULATORS

### 3.1 Introduction

In general an electro-optic(EO) modulator transforms an electrical signal into an optical signal. The incoming electrical signal is most commonly information encoded in a voltage change. This voltage change is then transformed into either a phase change or an intensity change in the light signal. In principle light has two more degrees of freedom, namely wavelength and polarization, which are used for multiplexing, but not as commonly used in modulation schemes. As EO materials change their refractive index if a voltage is applied across them, intensity modulation is also based on phase modulation, via consecutive interference. The most common device design for this is a Mach-Zehnder modulator (MZM); a schematic is shown in Fig. 3.1. When voltage is applied to one arm of the MZM, the refractive index of the material changes. If the phase of the light passing through this arm is either enhanced or retarded by  $\pi$ , the modulated light and the non-modulated light interfere destructively. The voltage at which this happens is called  $V_\pi$ .

The most commonly used material for EO modulators is lithium niobate ( $\text{LiNbO}_4$ ). Lithium niobate is a non-centrosymmetric crystal and therefore has a non-zero  $\chi^{(2)}$ .

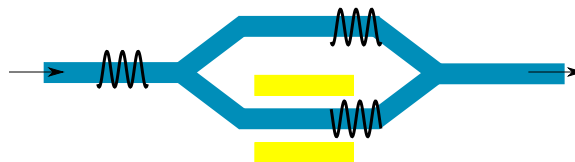


FIGURE 3.1. Schematic of a Mach-Zehnder modulator. The phase of the modulated arm is changed by  $\pi$ .

tensor. The corresponding  $r_{33}$  coefficient is around  $32 \text{ pmV}^{-1}$ [49] at  $1550\text{nm}$ , where the ordinary refractive index is 2.13 and the extraordinary refractive index is 2.21 [50]. Waveguide fabrication is commonly done by titanium in-diffusion processes[49] or proton exchange [51].

EO polymers have been successfully used in EO modulators showing sub-volt  $V_\pi$  [4] ( $1.8 \text{ Vcm}$   $V_\pi L$ ), low optical loss [52] and bandwidths above  $100 \text{ GHz}$  [53]. To date the best available crosslinkable EO polymers exhibit a combination of both large  $r_{33}$  values of  $100 \text{ pmV}^{-1}$  and excellent thermal stability up to  $230^\circ\text{C}$  , a very important advance that can enable high performance organic EO materials to fulfill the CMOS compatibility requirement [54].

### 3.2 Silicon EO hybrid modulators <sup>1</sup>

Because of their outstanding properties it is very desirable to integrate EO polymers with silicon devices to ease passive/active integration and to benefit from state-of-the-art complementary metaloxidesemiconductor (CMOS) fabrication capabilities. Silicon-based modulators based on plasma dispersion [55] have been demonstrated some time ago and this is now together with carrier depletion the most widely used approach. The  $V_\pi L$  for a MachZehnder configuration is around  $1.4\text{Vcm}$  up to  $12\text{GHz}$  [56]; for a microring geometry switching voltages are  $1 \text{ V}$  or lower [57]. If photonic crystal structures are incorporated to make use of the slow light effect  $V_\pi L$  values as low as  $0.05\text{Vmm}$  with  $20\text{dB}$  total insertion loss have been shown operating up to  $2\text{GHz}$  [58]. The use of silicon, however, requires multiple doping steps, which complicate the fabrication process. Photonic crystal structures require e-beam lithography and often show narrowband transmission and undesired dispersion characteristics. There are numerous approaches to integrating EO polymers on the silicon platform, such as silicon slot waveguides [59],[60],[61] and photonic crystal waveguides [61]. Slotted waveguide modulators have  $V_\pi L$  below  $1\text{Vcm}$  but optical insertion losses above  $35\text{dB}$

for slotted waveguides; the shortcomings of photonic crystal structures are mentioned previously, nevertheless  $V_\pi L$  below 0.5Vcm with losses around 22dB [62], has been achieved. As with photonic crystal structures, slotted waveguides require e-beam lithography, making them very challenging to fabricate and impractical to manufacture. We present a design that promises to exceed some of the performance standards mentioned earlier, but at the same time is straightforward to fabricate with optical lithography and is capable of broadband optical operation.

### 3.2.1 Optical Design

In this modulator design the silicon is completely passive, and therefore no implantation is needed which simplifies the fabrication process and keeps silicon based propagation losses to a minimum. Our design consists of a silicon strip waveguide surrounded by an EO polymer cladding. The electrodes for poling and driving are placed to the left and right of the silicon waveguide directly on the buried oxide (BOX) layer. The polymer can be applied at the backend of the fabrication process and therefore does not interfere with any CMOS processing. The constraints on polymer film quality are also low, as the light is tightly confined around the silicon waveguide, extending only a few hundred nanometers around the waveguide for the optimal geometry; a schematic is shown in Fig. 3.2.

To achieve good modulation performance certain criteria have to be fulfilled. The parameters influencing the switching voltage  $V_\pi$  are shown in (3.1)

$$V_\pi = \frac{\lambda d}{r_{33} L n_{eff}^3 \Gamma} \quad (3.1)$$

where  $\lambda$  is the wavelength of light,  $d$  is the electrode separation,  $n_{eff}$  is the eigenvalue of the propagating mode,  $L$  is the length of the active section,  $r_{33}$  is the Pockels coefficient and  $\Gamma$  the overlap integral factor of the light confined in the active material,

---

<sup>1</sup>Taken in large parts from Himmelhuber et.al. [47]

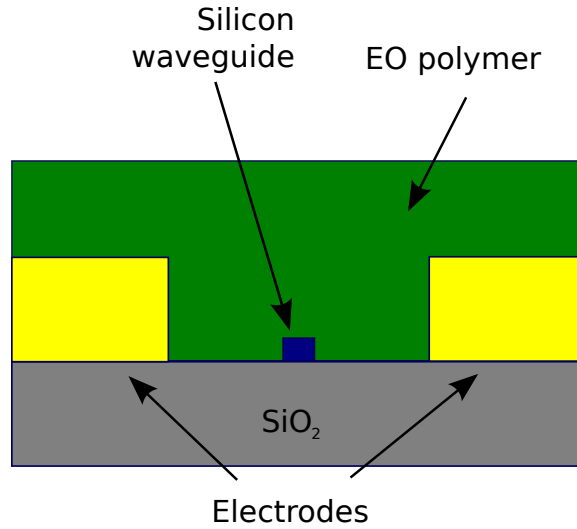


FIGURE 3.2. Schematic of the EO-silicon hybrid modulator structure.

in our case the cladding, with the electrical field used for modulation. In optimizing the design of the waveguide from an optical perspective we find it useful to ignore the modulating electrical field for the moment. In this case the overlap integral factor is just the well-known confinement factor [63],[64]. The main design parameters that influence the confinement factor and mode index are waveguide height and width, as the core is fixed to be silicon ( $n_{Si/1550nm} = 3.48$ ,  $n_{Si/1310nm} = 3.50$  [46]) and most EO polymers have refractive indices between 1.6 and 1.7. Because silicon photonics is reliant on silicon on insulator (SOI) wafers with thin device layers and the range of available silicon thicknesses is limited, we restricted our simulations to device layer thicknesses from 200 to 300nm. The simulations of the optical field in the waveguide structure were carried out using Fimmwave 5.1. Due to the coplanar electrode configuration only TE modes were considered, since this is the polarization corresponding to  $r_{33}$ , the largest EO polymer tensor component. In Fig.3.3, the Si waveguide width dependence of the confinement factor in the polymer cladding and the mode index for 250nm height silicon waveguides with EO polymer side cladding and SiO<sub>2</sub> bottom cladding is shown. One can see that with increasing waveguide width the confinement

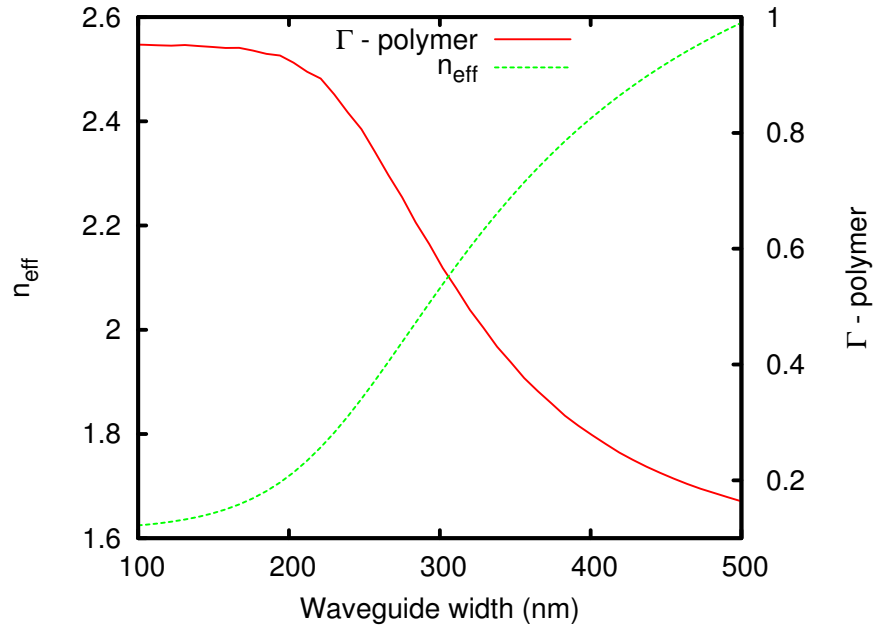


FIGURE 3.3. The confinement factor in the polymer ( $n = 1.7$ ) and  $n_{eff}^3$  vs. silicon waveguide width. The height of the silicon waveguide is 250nm and the wavelength of light is 1550nm.

reduces, but the effective index of the mode increases. For waveguides with less than 100nm width, most of the light is in the EO polymer. The reason that the mode index is below the polymer index in this case is that some light is in the BOX layer. For optimizing the waveguide dimensions the product of  $n_{eff}$  and  $\Gamma$  is of utmost importance.

In Fig. 3.4 a plot of the calculated values of  $n_{eff}^3\Gamma$  vs. waveguide width for different waveguide heights is shown for light at 1550nm. For 1550nm light the optimal waveguide width is around 275nm. In Fig. 3.5 a plot of the calculated values of  $n_{eff}^3\Gamma$  vs. waveguide width for different waveguide heights is shown for light with 1310nm. For 1310nm light the optimal waveguide width is between 200 and 220nm. These dimensions are readily achievable with optical lithography, making this design suitable for mass fabrication. In both cases the maxima are fairly flat, suggesting

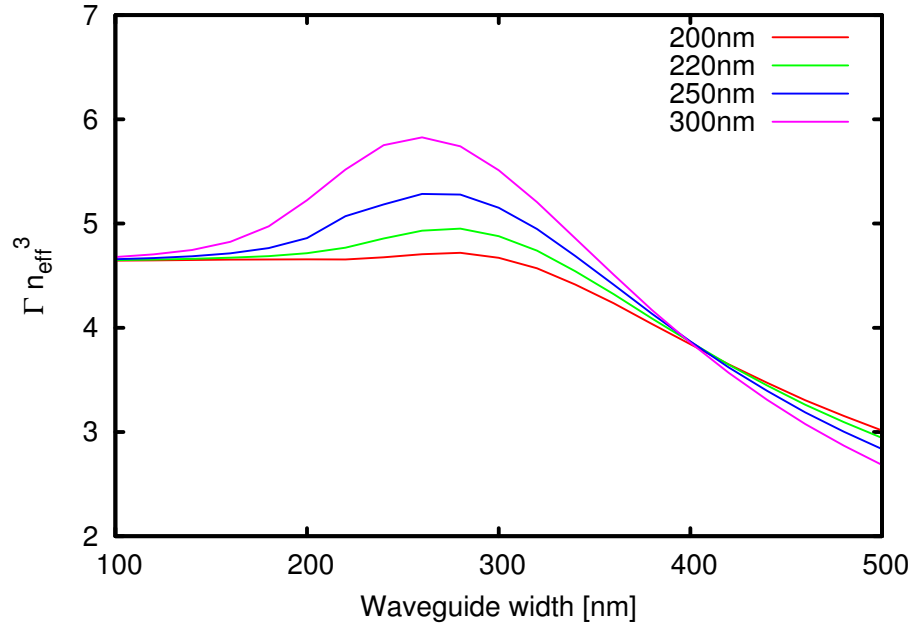


FIGURE 3.4. Confinement factor multiplied by  $n_{eff}^3$  for 1550nm light vs. waveguide width for different waveguide heights.

that the design has high fabrication tolerances. The trend that thicker waveguides seem to perform better is present for both wavelengths, with the values for 1310nm light being generally higher. For a conventional polymer modulator with the same EO polymer used the highest achievable value for  $n_{eff}^3\Gamma$  is 4.9. This assumes that all the light is confined in the polymer which is often not the case. Fig.3.6 shows the electrical field of a TE mode in a 260nm wide and 300nm high silicon waveguide with EO cladding on SiO<sub>2</sub> at 1550nm. One can see that equal amounts of the optical field are located to the left and right of the silicon waveguide, i.e., the mode is symmetric with respect to the Y axis.

### 3.2.2 Electrode Design

The electrode design in a coplanar-strip geometry is crucial for achieving the best possible performance, because the electrical field between the electrodes is highly

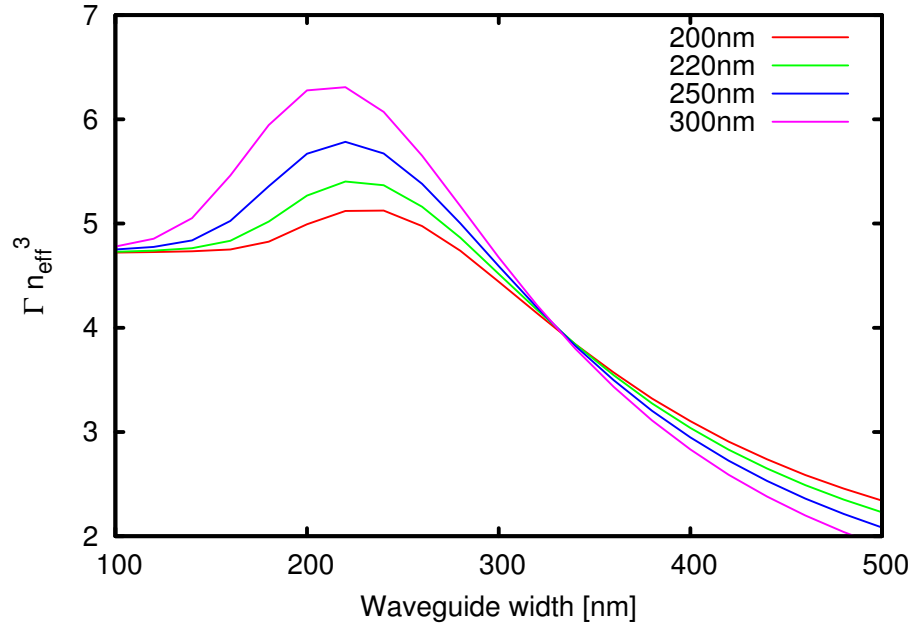


FIGURE 3.5. Confinement factor multiplied by  $n_{eff}^3$  for 1310nm light vs. waveguide width for different waveguide heights.

inhomogeneous. This configuration consists of one electrode acting as ground and one carrying the signal. With only one waveguide and two electrodes the device acts as a phase modulator, but it can be considered as one arm of a Mach-Zehnder modulator. In the past there have been approaches to describe the electrical field between coplanar electrodes analytically but these models assume infinitely thin electrodes [65] or a constant permittivity in the area of interest [64]. Because the EO polymer and silicon have different dielectric constants additional field variations are present and we used numerical simulations to estimate the electrical field inside the EO polymer. This is not only important for driving the modulator but also for poling the EO polymer because the achievable  $r_{33}$  values depend linearly on the poling field [5]. As can be seen from 3.1, one would like to have the electrodes as close together as possible, but too small a separation between the optical field and the metal electrodes will cause considerable optical losses, due to absorption by the metal.

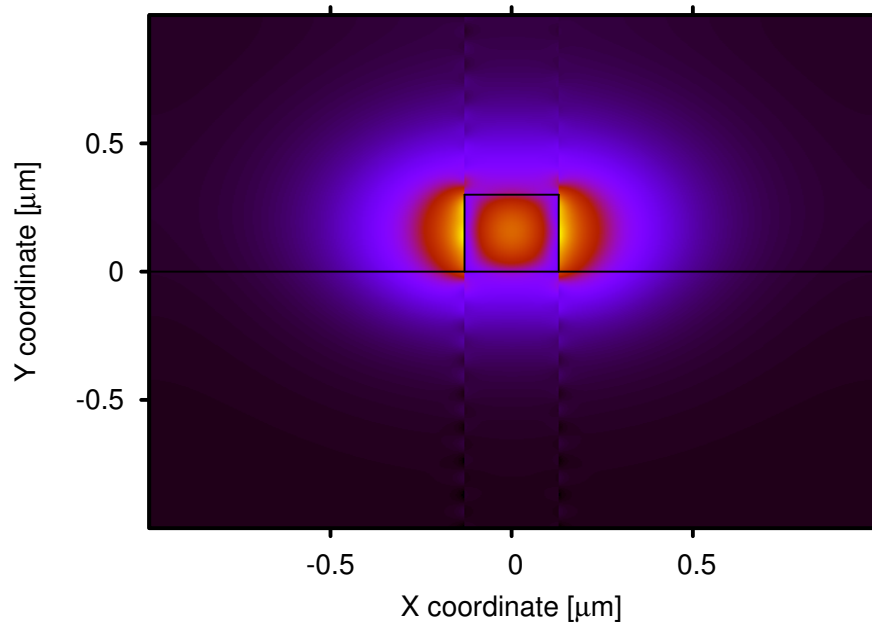


FIGURE 3.6. Electrical field of a TE mode in a 260nm wide and 300nm high silicon waveguide with EO cladding on SiO<sub>2</sub> at 1550nm.

The simulations indicate that electrode spacings over  $3\mu\text{m}$  for 300nm high waveguides (1550nm light) and over  $4\mu\text{m}$  for 200nm high waveguides should not contribute significantly ( $\leq 0.3 \text{ dBcm}^{-1}$ ) to the overall optical device loss, assuming that the appropriate waveguide width (see Fig. 3.5 and Fig. 3.4) is chosen. An electrode spacing of  $2\mu\text{m}$  increases the loss for 300nm high waveguides to  $1.6 \text{ dBcm}^{-1}$  for 1550nm light, which is already substantial, but this configuration is included for completeness and since for 1310nm light the optical losses at  $2\mu\text{m}$  spacing are still below  $0.2 \text{ dBcm}^{-1}$ . Further decreasing the electrode spacing leads to losses greater than  $10 \text{ dBcm}^{-1}$ . These results are fairly independent of the electrode thickness for these calculations where gold was the electrode metal. It is worth noting that simulations tend to underestimate the loss originating from metal electrodes and that electrodes made out of a metal with a higher real refractive index than gold ( $n_r \geq 1$  for 1550 and 1310nm) might show higher optical losses.

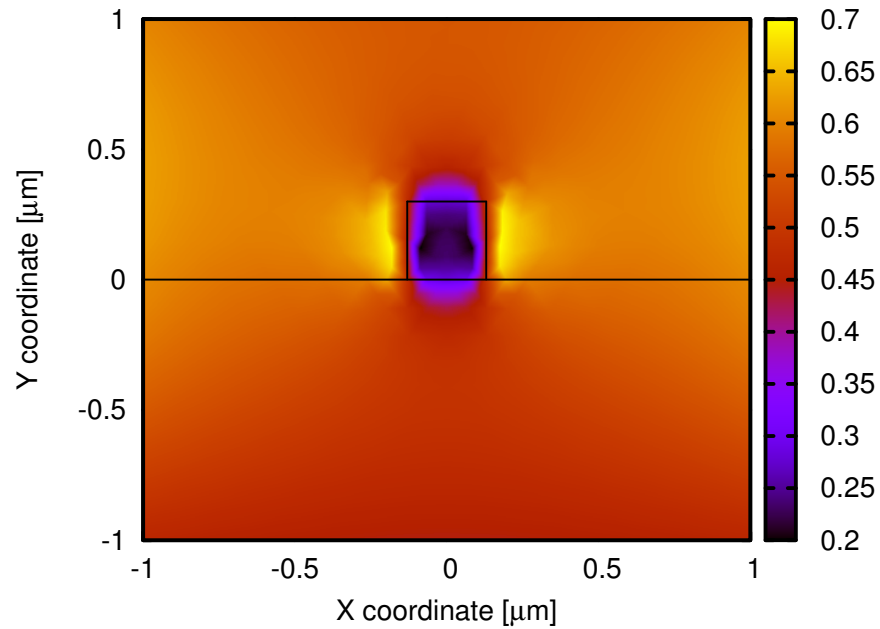


FIGURE 3.7. Simulated DC field around the EO polymer cladding waveguide for  $6\mu\text{m}$  electrode spacing and  $175\text{nm}$  electrode height.

Simulations to estimate the DC electric field were carried out with COMSOL 4.3a. In Fig. 3.7 the DC fields for two electrode configurations are shown. The scale of the DC field is normalized to the value for a microstrip geometry with the same electrode separation. In a microstrip geometry the field is simply the applied voltage divided by the electrode spacing. One can see that for  $6\mu\text{m}$  coplanar electrode spacing with  $175\text{nm}$  thick electrodes, the highest field around the waveguide is around 80% that of a microstrip.

If the electrode thickness is increased to  $2\mu\text{m}$  and the electrode spacing is reduced to  $3\mu\text{m}$  the highest field around the waveguide increases to 100% that of an equivalent microstrip (Fig 3.8). Further reducing the electrode spacing increases the field to around 120% of the microstrip value as can be seen in Fig.3.9. This field enhancement is due to the high dielectric constant of silicon compared to that of the EO polymer. Further increase of the electrode thickness does not lead to more field enhancement.

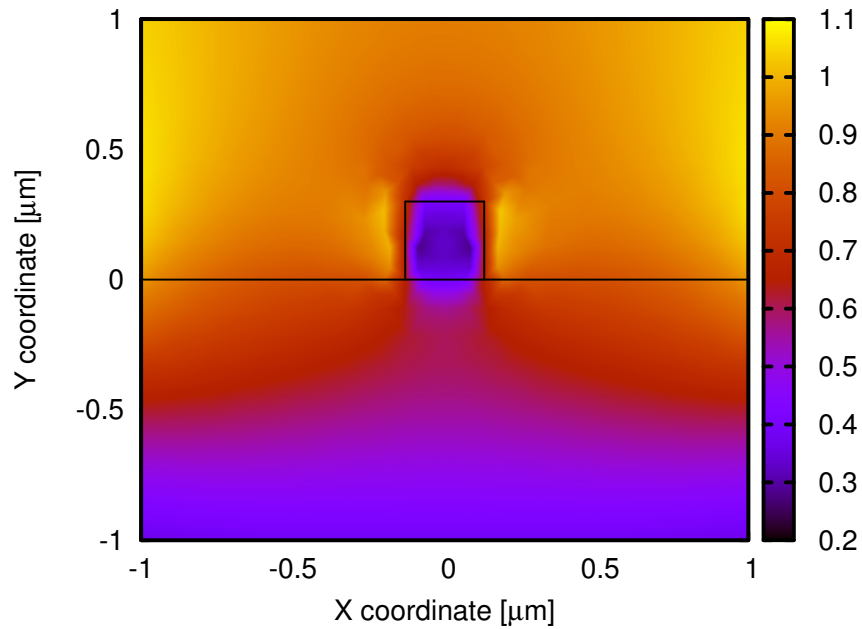


FIGURE 3.8. Simulated DC field around the EO polymer cladding waveguide for  $3\mu\text{m}$  electrode spacing and  $2\mu\text{m}$  electrode height.

When Fig.3.9 is compared with the Fig.3.6 , one can see that the DC field and the optical field left and right of the Si waveguide overlap well.

To analyze these results quantitatively, the overlap integral of the optical and the electrical fields was calculated numerically. For this a matrix representing the optical field and a matrix representing the electrical field are multiplied. One should note that both matrices have to be centered at the same point and the portions of the field outside the active EO material have to be removed. The matlaboctave code for this is given in Appendix B. In Fig.3.10 the results for different electrode thicknesses and spacings for  $1550\text{nm}$  light are shown. The optimal Si waveguide is  $260\text{nm}$  wide and has a thickness of  $300\text{nm}$ . For  $1310\text{ nm}$  light the optimal Si waveguide is now  $220\text{nm}$  wide and  $300\text{nm}$  thick, as shown in Fig.3.11

In the case of a microstrip geometry, the overlap integral of the electrical field with the optical field would simply be the confinement factor of the mode in the polymer,

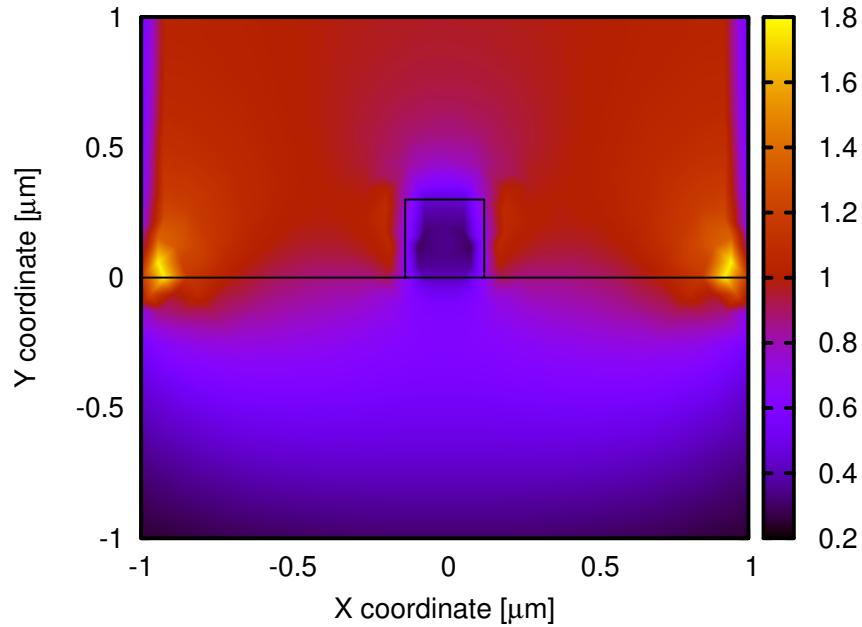


FIGURE 3.9. Simulated DC field around the EO polymer cladding waveguide for  $2\mu\text{m}$  electrode spacing and  $2\mu\text{m}$  electrode height.

because the DC field is homogenous. For the waveguide designed for 1310nm this would be 0.68, while for the 1550nm waveguide it is 0.71. From Fig. 3.10 and Fig. 3.11 and it is clear that both electrode spacing and electrode thickness play a major role in minimizing the overlap penalty due to a coplanar geometry. For 2 and  $3\mu\text{m}$  electrode spacing with 2m thick electrodes, the overlap integral is only reduced by 6 and 12% for 1550nm light and 8 and 14% for 1310 nm light, respectively.

To examine the suitability of the proposed electrode structure for possible high speed operation, the line capacitance as well as electrical loss from closed form analytical models was calculated. The line capacitance influences the RC time constant and with that the bandwidth of a lumped element structure as well as the RF power consumption ( $P_{AC} \propto CV^2$ ). A low capacitance is therefore desirable for high operating frequencies and low power consumption. In Fig. 3.12 the calculated line capacitance is shown for different coplanar-strip (CPS) geometries. A multilayer model for CPSe-

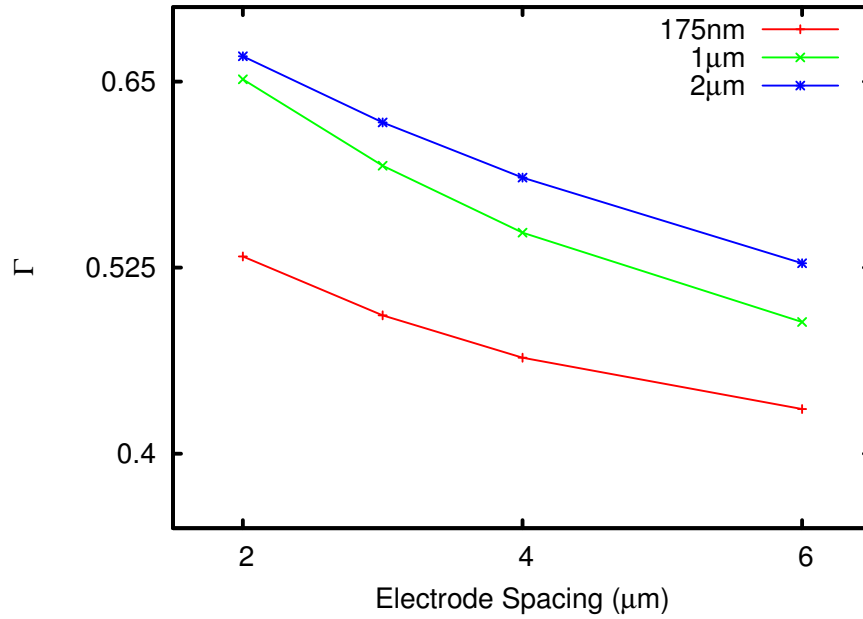


FIGURE 3.10. Overlap integral of the optical field in the EO polymer with the electrical DC field(1550nm light)

lectrodes [66] was used for the calculation. One should note that the calculated  $C_0$  is not correct and leads to false results. The base capacitance of the electrodes without any material ( $C_0$ ) was calculated in a slightly different way [67]. Due to the small volume of the silicon waveguide ( $< 2\%$ ) compared to the other materials, its contribution was ignored. The line capacitance of the analyzed CPSs is below  $1 \text{ pFcm}^{-1}$  for most structures. Here the electrode spacing is the gap between the electrodes where the waveguide would be situated and the electrode width is the width of one conductor. For these calculations the polymer cladding was assumed to be  $2\mu\text{m}$  thick and the BOX layer to be  $1\mu\text{m}$  thick. For silicon waveguide modulators line capacitances of  $3.4 \text{ pF/cm}$  have been demonstrated [68]. This is nearly a factor of 7 higher than a typical value for our proposed structure, corresponding to higher power consumption. Besides the capacitance, the electrical loss of the electrodes is important for good performance at high frequencies. We used an analytical model [69] to estimate the

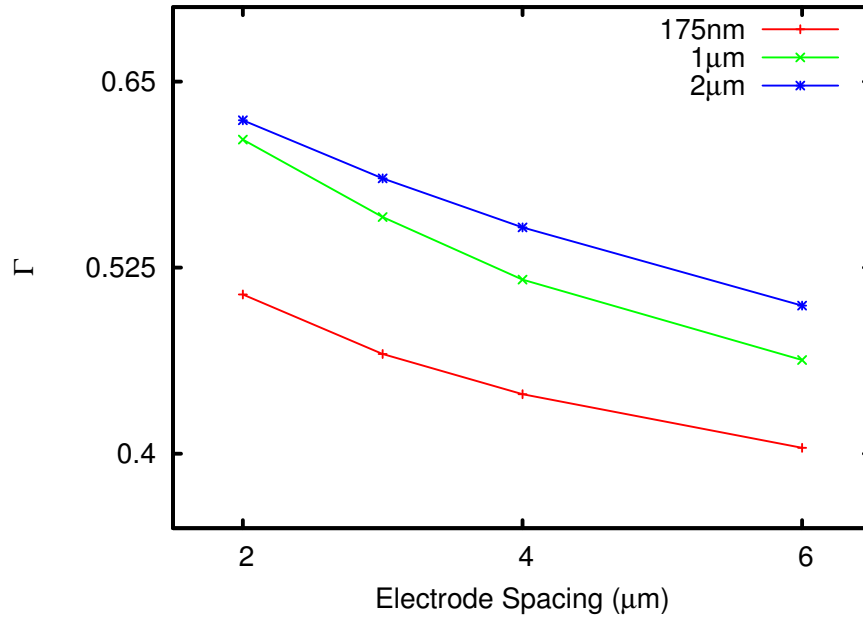


FIGURE 3.11. Overlap integral of the optical field in the EO polymer with the electrical DC field(1310nm light)

expected electrical loss of the coplanar-strip structures. The octavematlab scripts for calculating the capacitance and loss can be found in Appendix B. The calculations include dielectric as well as conductor losses. The estimated loss for several electrode structures can be seen in Fig. 3.13

The electrode loss decreases with increasing electrode width and electrode gap. It decreases dramatically in going from  $10\ \mu\text{m}$  to  $50\ \mu\text{m}$  electrode width, with  $50\ \mu\text{m}$  being the minimum width for having loss below 3 dB/cm at 50GHz; widening the electrodes beyond  $200\ \mu\text{m}$  provides only marginal further improvement. For all the structures analyzed the electrode loss is dominant. The average loss tangent of the EO-polymerSiO<sub>2</sub>Si structure was assumed to be 0.002[70],[71],[72].

An important factor determining the performance of an EO polymer modulator is the  $r_{33}$  coefficient of the polymer used. Polymers with up to  $160\text{pmV}^{-1}$  are now commercially available ([www.soluxra.com](http://www.soluxra.com)). This is the value assumed for  $V_{\pi}$  calcu-

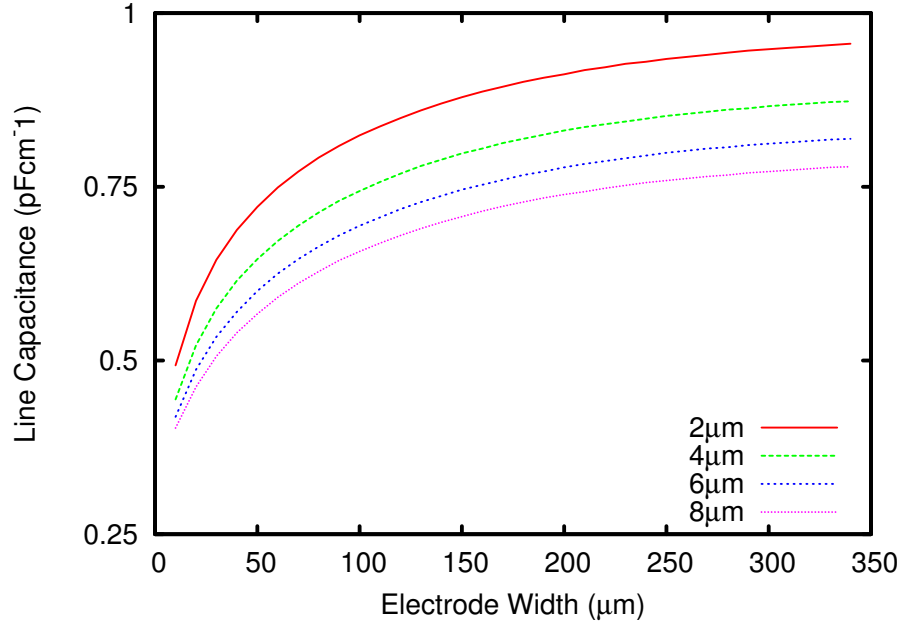


FIGURE 3.12. Line capacitance for 2,4,6, and 8 $\mu\text{m}$  electrode spacing plotted over the electrode width

lations. Future development of even better performing polymers will lower  $V_\pi$  even further. To also account for losses and the line capacitance, we defined a figure of merit (FOM) as follows

$$FOM = \frac{1}{V_\pi LC e^{(\alpha_o + \alpha_e)cm}} \quad (3.2)$$

where  $\alpha_o$  is the calculated optical mode loss caused by the electrode in  $\text{cm}^{-1}$ ,  $\alpha_e$  is the electrode loss coefficient at 50GHz in  $\text{cm}^{-1}$  for 50 $\mu\text{m}$  wide electrodes, and C is the line capacitance in  $\text{pFcm}^{-1}$  also for 50 $\mu\text{m}$  wide electrodes. In Fig. 3.14  $V_\pi L$  and the FOM are shown for the optimal waveguide dimension for 1550nm and 1310nm for different 2m thick electrode spacings. The lowest  $V_\pi L$  at the highest FOM was found to be 0.29Vcm at these electrode spacings for a 300nm  $\times$  220nm waveguide and 1310nm light. As expected both  $V_\pi L$  and FOM improve with smaller electrode spacing, but for electrode spacing below 2  $\mu\text{m}$  the FOM drops of sharply

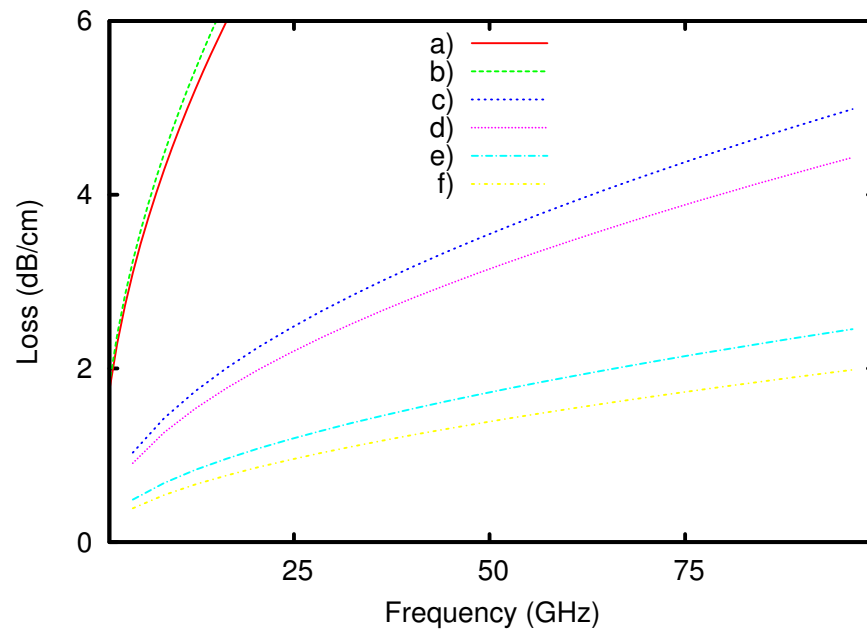


FIGURE 3.13. Calculated electrode loss for different electrode geometries ( a)=  $10\mu\text{m}$  wide,  $2\mu\text{m}$  gap, b)=  $10\mu\text{m}$  wide,  $4\mu\text{m}$  gap, c)=  $50\mu\text{m}$  wide,  $2\mu\text{m}$  gap, d)=  $50\mu\text{m}$  wide,  $4\mu\text{m}$  gap, e)=  $200\mu\text{m}$  wide,  $2\mu\text{m}$  gap, f)=  $200\mu\text{m}$  wide,  $4\mu\text{m}$  gap.

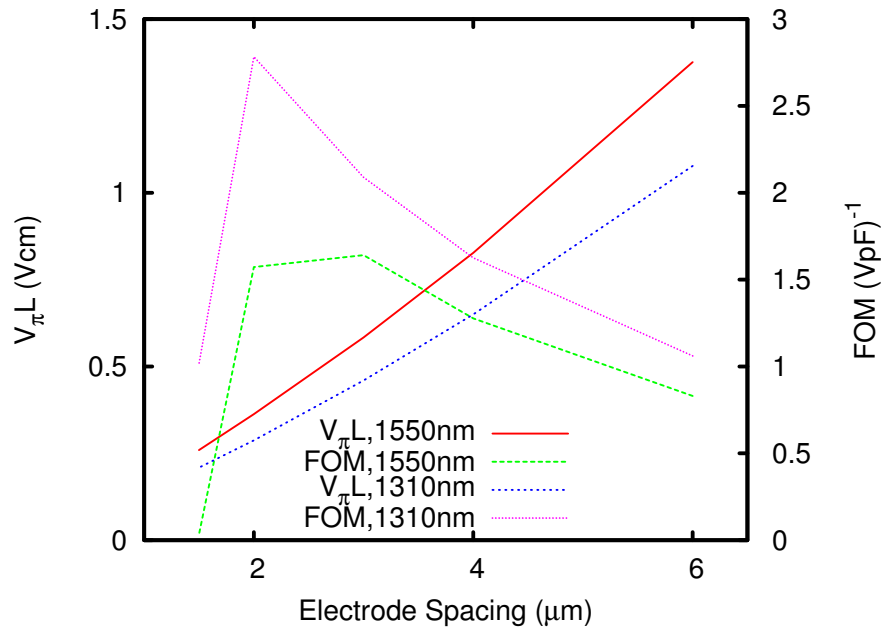


FIGURE 3.14. Calculated  $V_{\pi}L$  and FOM

due to increased optical and electrical loss. Note that these  $V_{\pi}L$  estimates would all be halved if a dual drive configuration were implemented.

### 3.2.3 Measurement results

Silicon waveguides with 220nm height and 275nm width in the active section and 2 $\mu\text{m}$  width at the input facet were fabricated to order at the UCSB nanofabrication facility by electrode beam lithography and dry etching. The taper from 2 $\mu\text{m}$  to 275nm was 100 $\mu\text{m}$  long and simulations predicted minimal loss from this transition. Electrodes with 5.4mm length were patterned with an MA6 mask aligner from Carl Suss and AZ5214 was used as a lift-off resist. The exact fabrication procedure for the electrode lift off is given in Appendix C. The metal layers were 25nm titanium and 150nm gold deposited with a Denton DV-502A electron evaporation tool. The photoresist was removed by stirring the samples in boiling acetone for 30min with

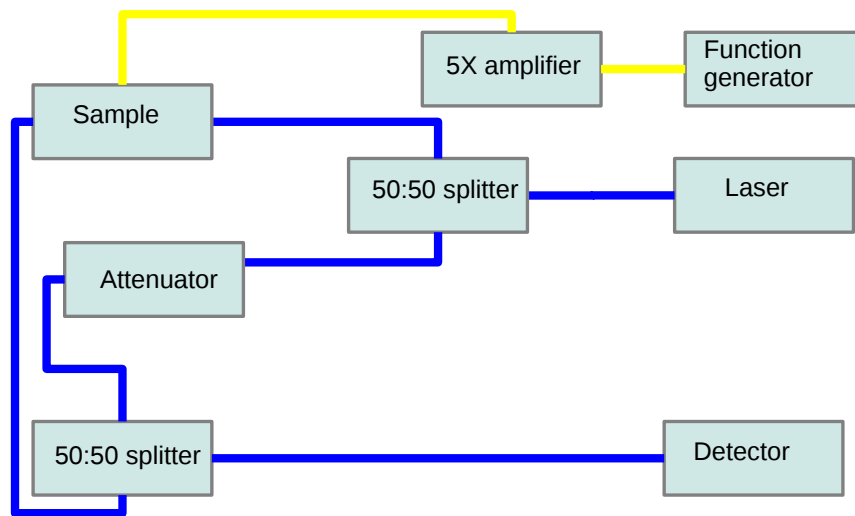


FIGURE 3.15. Schematic of the  $V$  measurement setup. Yellow lines show electrical and blue ones show optical connections

subsequent ultrasonication for 5min in hot acetone. The devices were then diced to a total length of 7mm; no subsequent polishing of the end facets was performed. The EO polymer SEO100 available from Soluxra was spun directly on the samples. Afterwards the samples were baked in a vacuum oven at 4mbar and 80°C for 16h. Poling was performed in a nitrogen atmosphere with an applied field of 700V for 7 $\mu$ m electrode spacing.

A lensed fiber with a mode field diameter of 2.5 $\mu$ m was used to couple light into the waveguide, with total TM loss of 20dB before poling with an estimated coupling loss of 13dB at 1550nm. The loss increased significantly with poling (5-10dB), presumably due to the space-charge-induced inhomogeneous poling field distribution [73], coupled with relatively large poling induced birefringence of these materials, leading to bulk scattering. Unfortunately the loss for the TE mode was too high for measurements. The origin of the high TE loss is likely to be sidewall roughness, to which TE modes are especially susceptible[74]. This is mostly due to the larger amount of the optical field extending to the sides of the waveguide in the case of TE polarization. Further optimization of fabrication and poling processes are required to tackle these problems. For  $V_\pi$  measurements the modulator was inserted into a fiber based Mach-Zehnder setup consisting of two 50:50 splitters, with the modulator being in the active arm (Fig. 3.15). The measured  $V_\pi$  for the TM mode was 21.35V at 1KHz. With the active length of 5.4mm, the calculated mode index of 1.748 and mode overlap of the electrical and optical field of 0.401 this corresponds to an  $r_{13}$  of roughly 44pmV<sup>-1</sup>.

A screenshot from the oscilloscope used to measure  $V_\pi$  of the modulation curve taken from an oscilloscope is shown in Fig. 3.16. The tensor ratio for EO polymers is generally 3 (see Chapter 2.6), which means that the  $r_{33}$  value can be estimated to be 132pmV<sup>1</sup>, which to our knowledge is the highest value ever achieved for an EO polymer in a coplanar geometry. This is consistent with non-device samples, which were poled under similar conditions and independently characterized. The theoretical  $V_\pi$  for the TE mode is 5.4 V for a mode index of 1.91 and optical-electrical field

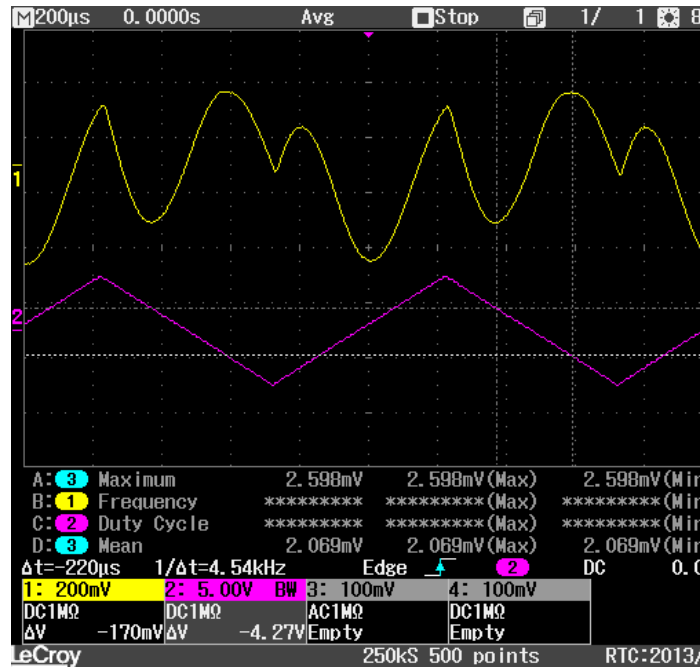


FIGURE 3.16. Screenshot from the oscilloscope used to measure  $V_{\pi}$

overlap of 0.41, corresponding to a  $V_{\pi} L$  of 3Vcm. This value is much higher than estimated above, primarily due to the large electrode spacing and the low overlap integral resulting from the use of 175 nm thick electrodes.

### 3.3 Silicon nitride devices

Silicon nitride, often used as a barrier or protection layer in electronics can also be used for waveguide applications. For this it is typically grown by chemical vapor deposition (CVD) on top of a silicon wafer with thermally grown oxide. Although, residual hydrogen from the CVD process needs to be removed by a high temperature baking step to achieve low loss at 1550nm, the optical losses at 1310nm can be very low. ( $\text{Si}_3\text{N}_4$ ) has a lower refractive index than silicon, with  $n = 1.979$  at 1550nm and 1.982 at 1310nm [75]. This has a number of impacts from a device design point of view. Because the index contrast in the waveguide is lower, sidewall roughness causes

lower loss, resulting in typically lower loss in  $\text{Si}_3\text{N}_4$  waveguides, when compared to silicon for typical etching processes. This also means that the mode confinement is smaller resulting in the necessity for larger electrode spacings. As will be shown later this also leads to smaller mode indices than in silicon waveguides.

### 3.3.1 Optical Design

As with the silicon based modulator design discussed earlier, the  $\text{Si}_3\text{N}_4$  is completely passive and the index modulation happens in the EO polymer cladding. The optimal dimension can be found in the same way by maximizing the confinement factor multiplied by  $n_{eff}^3$ . Optimization was carried out at 1310nm wavelength. In Fig. 3.17 the confinement factor and the effective index for two different  $\text{Si}_3\text{N}_4$  heights are shown versus the waveguide width. For 250nm height no mode is supported for waveguides narrower than 500nm. When compared to Fig. 3.3 one can see that the refractive index in  $\text{Si}_3\text{N}_4$  depends much less on the waveguide dimensions than in the silicon case. This is because the refractive index of  $\text{Si}_3\text{N}_4$  is much closer to the index of the EO polymer. In Fig. 3.18 it can be seen that unfortunately there is no clear maximum which would indicate optimal dimensions as what was found in Fig. 3.5. The highest achievable value for  $n_{eff}^3\Gamma$  in the  $\text{Si}_3\text{N}_4$  case is on par with a pure polymer modulator and around 20% lower than for silicon.

### 3.3.2 Sidecladding for field concentration

As can be seen from Fig. 3.17 and 3.18 the best device results are to be expected when most of the light is in the polymer. In the case of a silicon waveguide the optimal  $\Gamma$  is around 0.7. The fact that more light is in the polymer in the  $\text{Si}_3\text{N}_4$  case means that the performance can benefit more from modulation field concentration. This can be achieved by utilizing a high epsilon side cladding. Potential candidates are the materials discussed in Chapter (1.3.4). In Fig. 3.19 the electric field concentration in

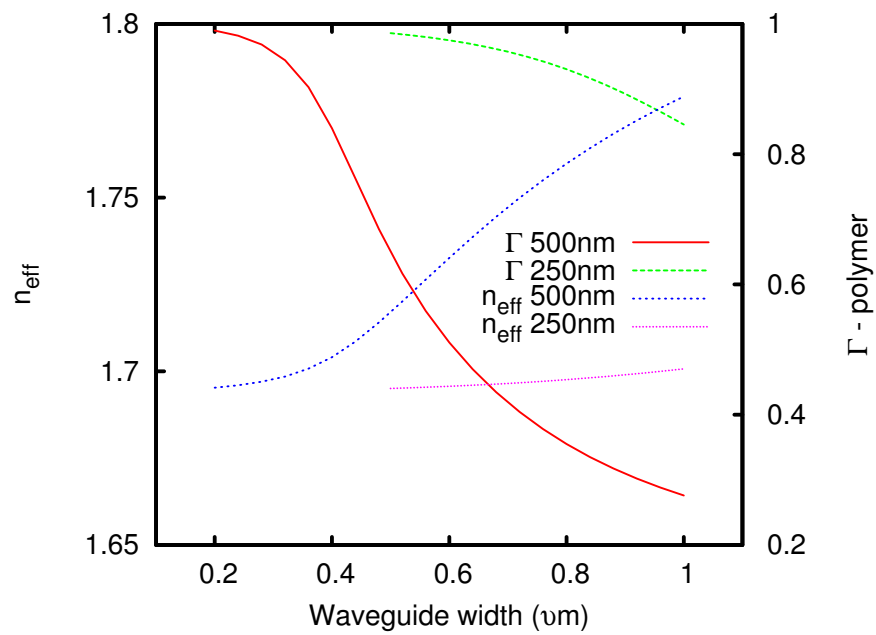


FIGURE 3.17. The confinement factor in the polymer ( $n = 1.7$ ) and  $n_{eff}$  vs.  $\text{Si}_3\text{N}_4$  waveguide width. The height of the  $\text{Si}_3\text{N}_4$  waveguide is 250nm and 500nm, while the wavelength of light is 1310nm.

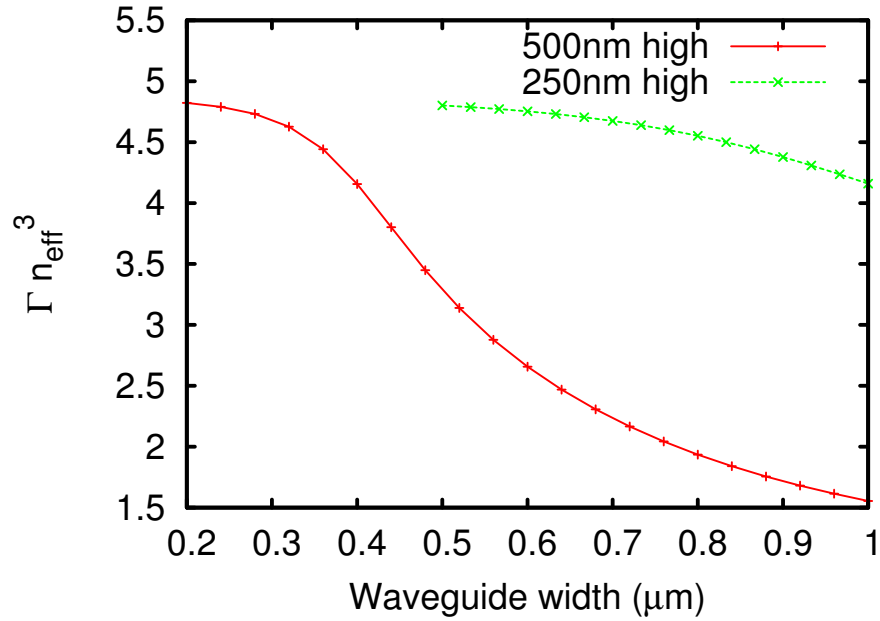


FIGURE 3.18. Confinement factor multiplied by  $n_{eff}^3$  for 1310nm light vs. waveguide width for different waveguide heights.

the EO polymer region can be seen. The dielectric constant of the EO polymer was set to 3 and  $\epsilon$  of the sol gel side cladding was 5.5, which is the measured dielectric constant for MAPTMS/ZPO 955 at 1KHz. The amount of field concentration in the polymer region depends on the dielectric constant of the cladding material. The materials discussed in Chapter 1.3.4 have dielectric constants up to 90. In Fig. 3.20 and Fig. 3.21 two cases are shown for a side cladding with  $\epsilon = 10$  and  $\epsilon = 100$ . The values are given relative to the plate capacitor case. This means that a value of 1.2 would indicate that the field is 20% higher than the applied voltage divided by the electrode spacing. By increasing the dielectric constant from 5.5 to 10 the electric field in the polymer region increases from approximately 1.2 to 1.5; when increased to 100, the field concentration factor increases to 2.8.

In addition to the dielectric constants, the structural dimensions also play a role in the enhancement of the modulation field. The trends for electrode spacing and

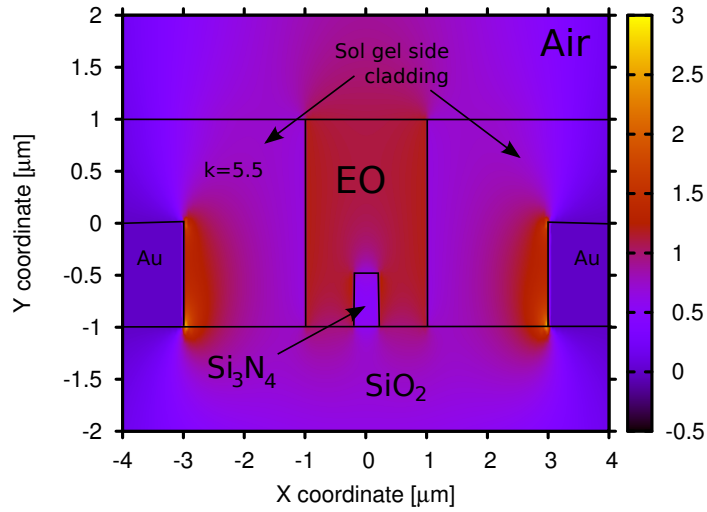


FIGURE 3.19. Electrical modulation field distribution for a  $\text{Si}_3\text{N}_4$  device with sol gel side cladding.

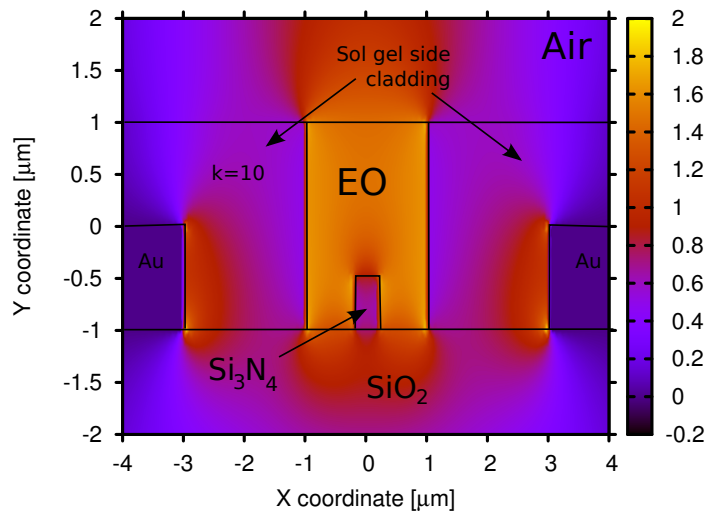


FIGURE 3.20. Electrical modulation field distribution for a  $\text{Si}_3\text{N}_4$  device with sol gel side cladding ( $\epsilon = 10$ ).

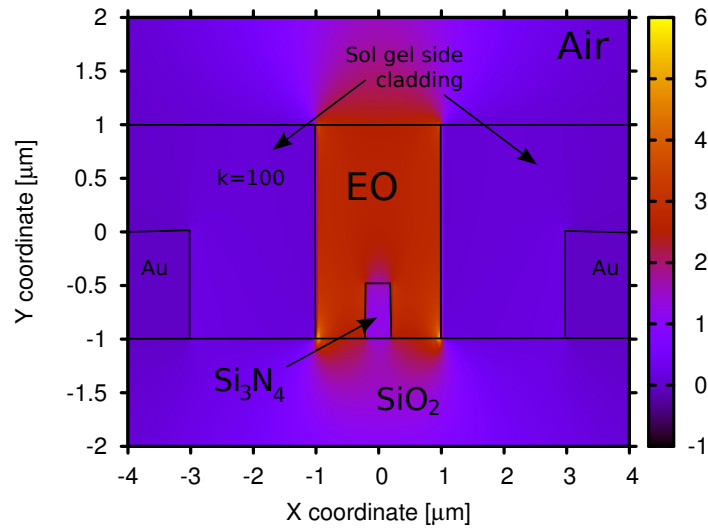


FIGURE 3.21. Electrical modulation field distribution for a  $\text{Si}_3\text{N}_4$  device with sol gel side cladding ( $\epsilon = 100$ ).

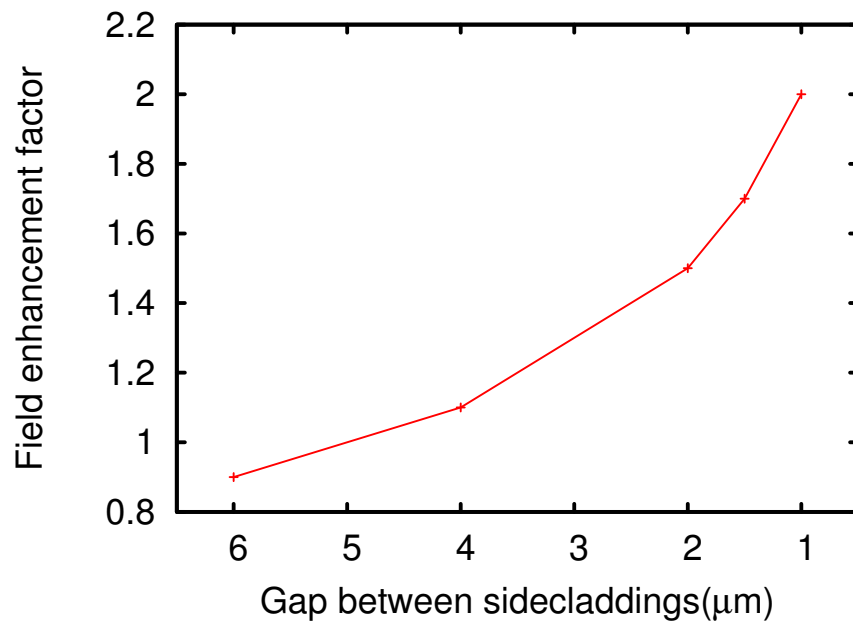


FIGURE 3.22. Electrical field enhancement increases with decreasing EO polymer gap.

thickness are the same as already mentioned in Section 3.2.2. In Fig. 3.22 the field enhancement factor for a  $\text{Si}_3\text{N}_4$  device with  $6\mu\text{m}$  electrode spacing and a sidecladding with an  $\epsilon$  of 10 is shown. The case where the gap is  $6\mu\text{m}$  corresponds to the case when no sidecladding is present. By changing the gap between the two sidecladdings the electrical field gets enhanced by over a factor of two. Narrowing the gap even more causes a large amount of the light to propagate in the side cladding and is therefore lost for modulation. One should note that the same method can be used for the silicon case.

### 3.4 Summary

The concept of a silicon waveguide EO polymer cladding modulator has been described. Design parameters have been defined and optimal dimensions have been found. A first device has been demonstrated and the necessary coplanar strip electrode geometry has been explored. The concept has been transferred to a  $\text{Si}_3\text{N}_4$  device which promises lower loss. The concept of a high  $\epsilon$  side cladding for enhancing poling and driving field has been introduced and its influence has been determined by simulations.

## Appendix A

### SOL-GEL RECIPES

**RH4:** In a 20ml vial with a polypropylene cap and magnetic stir bar, 4g (0.01611 mol) MAPTMS and 3.9377g DPDMS (0.01611 mol) with 0.693 g of 0.1M hydrochloric acid (0.0371 mol of water and  $6.8 \times 10^{-5}$  mol of HCl) are stirred on a stir plate for 5 days. Afterwards the cap is removed from the vial and the heater of the stir plate is turned on and set to 130°C . The vial is heated until 1.83g of methanol is evaporated.

**RH5:** In a 20ml vial with a polypropylene cap and magnetic stir bar, 4g (0.01611 mol) MAPTMS and 3.9377g DPDMS (0.01611 mol) with 0.5338 g of 0.1M hydrochloric acid (0.0286 mol of water and  $5.2 \times 10^{-5}$  mol of HCl) are stirred on a stir plate for 5 days. Afterwards the cap is removed from the vial and the heater of the stir plate is turned on and set to 130°C . The vial is heated until 1.83g of methanol is evaporated.

**RH8:** In a 20ml vial with a polypropylene cap and magnetic stir bar, 5g (0.02013 mol) MAPTMS and 4.92g DPDMS (0.02013 mol) with 0.658 g of 1M hydrochloric acid (0.0352 mol of water and  $6.4 \times 10^{-4}$  mol of HCl) are stirred on a stir plate for 5 days. Afterwards the cap is removed from the vial and the heater of the stir plate is turned on and set to 130°C . The vial is heated until 2.2g of methanol is evaporated.

For spincoating the resin is now diluted with 0.83 (10%) propylene glycol mono methyl ether acetate (PGMEA) and 0.083 (10%) of Irgacure 369 is added.

**RH10:** In a 20ml vial with a polypropylene cap and magnetic stir bar, 2.5g (0.01007 mol) MAPTMS, 4.92g DPDMS (0.02013 mol) and 2 g of PTMS (0.01007 mol)

with 0.658 g of 1M hydrochloric acid (0.0352 mol of water and  $6.4 \times 10^{-4}$  mol of HCl) are stirred on a stir plate for 5 days. Afterwards the cap is removed from the vial and the heater of the stir plate is turned on and set to 130°C . The vial is heated until 2.2g of methanol is evaporated.

For spincoating the resin is now diluted with 0.83 (10%) propylene glycol mono methyl ether acetate (PGMEA) and 0.083 (10%) of Irgacure 369 is added.

**RH17:** In a 20ml vial with a polypropylene cap and magnetic stir bar, 3.74g (0.01504 mol) MAPTMS, 4.92g DPDMS (0.02013 mol) and 1 g of PTMS (0.0508 mol) with 0.658 g of 1M hydrochloric acid (0.0352 mol of water and  $6.4 \times 10^{-4}$  mol of HCl) are stirred on a stir plate for 5 days. Afterwards the cap is removed from the vial and the heater of the stir plate is turned on and set to 130°C . The vial is heated until 2.2g of methanol is evaporated.

For spincoating the resin is now diluted with 0.83 (10%) propylene glycol mono methyl ether acetate (PGMEA) and 0.083 (10%) of Irgacure 369 is added.

**RH28:** In a 20ml vial with a polypropylene cap and magnetic stir bar, 5g (0.02 mol) MAPTMS, 4.9g DPDMS (0.02 mol) and 3 g of SucAHTES (0.01 mol) with 1.068 g of 1M hydrochloric acid (0.0572 mol of water and  $1.1 \times 10^{-3}$  mol of HCl) are stirred on a stir plate for 5 days. Afterwards the cap is removed from the vial and the heater of the stir plate is turned on and set to 130°C . The vial is heated until 3g of methanol is evaporated.

For spincoating the resin is now diluted with 1.1 (10%) propylene glycol mono methyl ether acetate (PGMEA) and 0.22 (20%) of Irgacure 369 is added.

**RH28-2:** In a 20ml vial with a polypropylene cap and magnetic stir bar 1.5 g of SucAHTES (0.05 mol) with 1.068 g of 1M hydrochloric acid (0.0572 mol of water and  $1.1 \times 10^{-3}$  mol of HCl) are stirred on a stir plate for 1 hour. Afterwards 2.5g (0.01 mol) MAPTMS, 2.46g DPDMS (0.01 mol) and 6 g of iso-propanol

are added. The mixture is stirred for 5 days. Then the cap is removed from the vial and the heater of the stir plate is turned on and set to 130°C . The vial is heated until 2g of methanol is evaporated.

For spincoating the resin is now diluted with 0.54 (10%) propylene glycol mono methyl ether acetate (PGMEA) and 0.054 (20%) of Irgacure 369 is added.

**RH28-2-st:** In a 20ml vial with a polypropylene cap and magnetic stir bar, 1.5 g of SuccAHTES (0.05 mol) with 1.27 g of water (0.07 mol) and 4 g iso-propanol are stirred on a stir plate for 20 hours. Afterwards 2.5g (0.01 mol) MAPTMS, 2.46g DPDMS (0.01 mol) and 0.078 tetra-butyl-ammonium-flouride dissolved in 4 g iso-propanol are added. The mixture is stirred for 5 days. Then the cap is removed from the vial and the heater of the stir plate is turned on and set to 130°C . The vial is heated until 2g of methanol is evaporated.

For spincoating the resin is now diluted with 0.54 (10%) propylene glycol mono methyl ether acetate (PGMEA) and 0.054 (20%) of Irgacure 369 is added.

**RH31:** In a 20ml vial with a polypropylene cap and magnetic stir bar, 2g (0.00805 mol) MAPTMS, 1.57g DPDMS (0.00644 mol) and 0.68 g of BPFDPDMS (0.00161 mol) with 0.2390 g of 1M hydrochloric acid (0.0128 mol of water and  $2.3 \times 10^{-4}$  mol of HCl) are stirred on a stir plate for 5 days. Afterwards the cap is removed from the vial and the heater of the stir plate is turned on and set to 130°C . The vial is heated until 0.81g of methanol is evaporated.

For spincoating the resin is now diluted with 0.36 (10%) propylene glycol mono methyl ether acetate (PGMEA) and 0.036 (10%) of Irgacure 369 is added.

**RH33:** In a 20ml vial with a polypropylene cap and magnetic stir bar, 2g (0.00805 mol) MAPTMS, 1.57g DPDMS (0.00644 mol) and 0.37 g of BPFDPDMS (0.00087 mol) with 0.261 g of 1M hydrochloric acid (0.014 mol of water and  $2.5 \times 10^{-4}$  mol of HCl) are stirred on a stir plate for 5 days. Afterwards the cap is removed

from the vial and the heater of the stir plate is turned on and set to 130°C . The vial is heated until 0.89g of methanol is evaporated.

For spincoating the resin is now diluted with 0.36 (10%) propylene glycol mono methyl ether acetate (PGMEA) and 0.036 (10%) of Irgacure 369 is added.

**RH34:** In a 20ml vial with a polypropylene cap and magnetic stir bar, 2g (0.00805 mol) MAPTMS, 1.76g DPDMS (0.00724 mol) and 0.27 g of BPFDPDMS (0.00064 mol) with 0.265 g of 1M hydrochloric acid (0.0142 mol of water and  $2.6 \times 10^{-4}$  mol of HCl) are stirred on a stir plate for 5 days. Afterwards the cap is removed from the vial and the heater of the stir plate is turned on and set to 130°C . The vial is heated until 0.9g of methanol is evaporated.

For spincoating the resin is now diluted with 0.36 (10%) propylene glycol mono methyl ether acetate (PGMEA) and 0.036 (10%) of Irgacure 369 is added.

**RHTi1:** The reaction of  $\text{TiCl}_4$  with ethanol is highly exothermic and HCl gas is formed during it. The whole synthesis should be performed inside a fume hood and with great care. In a 20ml vial with a polypropylene cap, 0.9g (0.047 mol) of titanium tetra chloride ( $\text{TiCl}_4$ ) are added to 10 ml (7.89g) dry ethanol. The vial is closed and the mixture is shaken for 5 seconds. Then 0.28g (0.0156mol) of water are added. After the vial is again shaken, 0.98g (0.0169 mol) of propylene oxide are added. The vial is again closed and shaken. The mixture should be allowed to age for 5 to 7 days before spincoating.

For spincoating, the silicon substrate is spin cleaned with acetone, water and iso-propanol. The RHTi mixture dispensed through a 100nm polytetrafluoroethylene membrane syringe filter directly onto the substrate. The films are spin-coated between 1000 and 4000 RPM without a spread cycle, followed by baking for 30 sec at 80°C , for 10 min at 120°C on a hotplate and then for 18h at 150°C in an oven.

**RHTi2:** The reaction of  $\text{TiCl}_4$  with ethanol is highly exothermic and  $\text{HCl}$  gas is formed during it. The whole synthesis should be performed inside a fume hood and with great care. In a 20ml vial with a polypropylene cap, 0.9g (0.047 mol) of titanium tetra chloride ( $\text{TiCl}_4$ ) are added to 10 ml (7.89g) dry ethanol. The vial is closed and the mixture is shaken for 5 seconds. Then 0.28g (0.0156mol) of water are added. After the vial is again shaken, 2.4g (0.0169 mol) of glycidyl methacrylate are added. The vial is again closed and shaken. The mixture should be allowed to age for 5 to 7 days before spincoating.

For spincoating, the silicon substrate is spin cleaned with acetone, water and iso-propanol. The RHTi mixture dispensed through a 100nm polytetrafluoroethylene membrane syringe filter directly onto the substrate. The films are spin-coated between 1000 and 4000 RPM without a spread cycle, followed by baking for 30 sec at  $80^\circ\text{C}$  , for 10 min at  $120^\circ\text{C}$  on a hotplate and then for 18h at  $150^\circ\text{C}$  in an oven.

**RHTi13:** The reaction of  $\text{TiCl}_4$  with ethanol is highly exothermic and  $\text{HCl}$  gas is formed during it. The whole synthesis should be performed inside a fume hood and with great care. In a 20ml vial with a polypropylene cap, 0.9g (0.047 mol) of titanium tetra chloride ( $\text{TiCl}_4$ ) are added to 11.086 ml (8.73g) dry ethanol. The vial is closed and the mixture is shaken for 5 seconds. Then 0.28g (0.0156mol) of water are added. After the vial is again shaken, 0.978g (0.0168 mol) of propylene oxide are added. The vial is again closed and shaken. The mixture should be allowed to age for 5 to 7 days before spincoating.

For spincoating, the silicon substrate is spin cleaned with acetone, water and iso-propanol. The RHTi mixture dispensed through a 100nm polytetrafluoroethylene membrane syringe filter directly onto the substrate. The films are spin-coated between 1000 and 4000 RPM without a spread cycle, followed by baking for 30 sec at  $80^\circ\text{C}$  , for 10 min at  $120^\circ\text{C}$  on a hotplate and then for 18h

at 150°C in an oven.

**RHTi14:** The reaction of  $\text{TiCl}_4$  with ethanol is highly exothermic and  $\text{HCl}$  gas is formed during it. The whole synthesis should be performed inside a fume hood and with great care. In a 20ml vial with a polypropylene cap, 0.9g (0.047 mol) of titanium tetra chloride ( $\text{TiCl}_4$ ) are added to 10.27 ml (8.1g) dry ethanol. The vial is closed and the mixture is shaken for 5 seconds. Then 0.28g (0.0156mol) of water are added. After the vial is again shaken, 0.244g (0.0042 mol) of propylene oxide and 1.799g (0.0126mol) of glycidyl methacrylate are added. The vial is again closed and shaken. The mixture should be allowed to age for 5 to 7 days before spincoating.

For spincoating, the silicon substrate is spin cleaned with acetone, water and iso-propanol. The RHTi mixture dispensed through a 100nm polytetrafluoroethylene membrane syringe filter directly onto the substrate. The films are spin-coated between 1000 and 4000 RPM without a spread cycle, followed by baking for 30 sec at 80°C , for 10 min at 120°C on a hotplate and then for 18h at 150°C in an oven.

**RHTi15:** The reaction of  $\text{TiCl}_4$  with ethanol is highly exothermic and  $\text{HCl}$  gas is formed during it. The whole synthesis should be performed inside a fume hood and with great care. In a 20ml vial with a polypropylene cap, 0.9g (0.047 mol) of titanium tetra chloride ( $\text{TiCl}_4$ ) are added to 10.53 ml (8.31g) dry ethanol. The vial is closed and the mixture is shaken for 5 seconds. Then 0.28g (0.0156mol) of water are added. After the vial is again shaken, 0.4878g (0.0084 mol) of propylene oxide and 1.2g (0.0084mol) of glycidyl methacrylate are added. The vial is again closed and shaken. The mixture should be allowed to age for 5 to 7 days before spincoating.

For spincoating, the silicon substrate is spin cleaned with acetone, water and

iso-propanol. The RHTi mixture dispensed through a 100nm polytetrafluoroethylene membrane syringe filter directly onto the substrate. The films are spin-coated between 1000 and 4000 RPM without a spread cycle, followed by baking for 30 sec at 80°C , for 10 min at 120°C on a hotplate and then for 18h at 150°C in an oven.

**RHTi16:** The reaction of  $\text{TiCl}_4$  with ethanol is highly exothermic and HCl gas is formed during it. The whole synthesis should be performed inside a fume hood and with great care. In a 20ml vial with a polypropylene cap, 0.9g (0.047 mol) of titanium tetra chloride ( $\text{TiCl}_4$ ) are added to 10.78 ml (8.50g) dry ethanol. The vial is closed and the mixture is shaken for 5 seconds. Then 0.28g (0.0156mol) of water are added. After the vial is again shaken, 0.731g (0.0126 mol) of propylene oxide and 0.599g (0.0042mol) of glycidyl methacrylate are added. The vial is again closed and shaken. The mixture should be allowed to age for 5 to 7 days before spincoating.

For spincoating, the silicon substrate is spin cleaned with acetone, water and iso-propanol. The RHTi mixture dispensed through a 100nm polytetrafluoroethylene membrane syringe filter directly onto the substrate. The films are spin-coated between 1000 and 4000 RPM without a spread cycle, followed by baking for 30 sec at 80°C , for 10 min at 120°C on a hotplate and then for 18h at 150°C in an oven.

**RHTi17:** The reaction of  $\text{TiCl}_4$  with ethanol is highly exothermic and HCl gas is formed during it. The whole synthesis should be performed inside a fume hood and with great care. In a 20ml vial with a polypropylene cap, 0.9g (0.047 mol) of titanium tetra chloride ( $\text{TiCl}_4$ ) are added to 10.93 ml (8.62g) dry ethanol. The vial is closed and the mixture is shaken for 5 seconds. Then 0.28g (0.0156mol) of water are added. After the vial is again shaken, 0.854g (0.0147 mol) of propylene oxide and 0.299g (0.0021mol) of glycidyl methacrylate are added. The vial is

again closed and shaken. The mixture should be allowed to age for 5 to 7 days before spincoating.

For spincoating, the silicon substrate is spin cleaned with acetone, water and iso-propanol. The RHTi mixture dispensed through a 100nm polytetrafluoroethylene membrane syringe filter directly onto the substrate. The films are spin-coated between 1000 and 4000 RPM without a spread cycle, followed by baking for 30 sec at 80°C , for 10 min at 120°C on a hotplate and then for 18h at 150°C in an oven.

**RHTi18:** The reaction of  $\text{TiCl}_4$  with ethanol is highly exothermic and HCl gas is formed during it. The whole synthesis should be performed inside a fume hood and with great care. In a 20ml vial with a polypropylene cap 0.9g (0.047 mol) of titanium tetra chloride ( $\text{TiCl}_4$ ) are added to 10.97 ml (8.68g) dry ethanol. The vial is closed and the mixture is shaken for 5 seconds. Then 0.28g (0.0156mol) of water are added. After the vial is again shaken, 0.915g (0.0158 mol) of propylene oxide and 0.136g (0.001mol) of glycidyl methacrylate are added. The vial is again closed and shaken. The mixture should be allowed to age for 5 to 7 days before spincoating.

For spincoating, the silicon substrate is spin cleaned with acetone, water and iso-propanol. The RHTi mixture dispensed through a 100nm polytetrafluoroethylene membrane syringe filter directly onto the substrate. The films are spin-coated between 1000 and 4000 RPM without a spread cycle, followed by baking for 30 sec at 80°C , for 10 min at 120°C on a hotplate and then for 18h at 150°C in an oven.

**RHTi19:** The reaction of  $\text{TiCl}_4$  with ethanol is highly exothermic and HCl gas is formed during it. The whole synthesis should be performed inside a fume hood and with great care. In a 20ml vial with a polypropylene cap, 0.9g (0.047 mol) of titanium

tetra chloride ( $\text{TiCl}_4$ ) are added to 11ml (8.68g) dry ethanol. The vial is closed and the mixture is shaken for 5 seconds. Then 0.28g (0.0156mol) of water are added. After the vial is again shaken, 0.940g (0.0162 mol) of propylene oxide and 0.075g (0.0005mol) of glycidyl methacrylate are added. The vial is again closed and shaken. The mixture should be allowed to age for 5 to 7 days before spincoating.

For spincoating, the silicon substrate is spin cleaned with acetone, water and iso-propanol. The RHTi mixture dispensed through a 100nm polytetrafluoroethylene membrane syringe filter directly onto the substrate. The films are spin-coated between 1000 and 4000 RPM without a spread cycle, followed by baking for 30 sec at  $80^\circ\text{C}$  , for 10 min at  $120^\circ\text{C}$  on a hotplate and then for 18h at  $150^\circ\text{C}$  in an oven.

## Appendix B

### MATLAB - OCTAVE CODE

#### B.1 Optical field handling

The optical field handling script must be run before the electrical field handling script. They could be in the same program, but the electrical part takes a long time to run, due to the `griddata` command.

```
1
2 clear
3
4 %FIMMWAVE exports all E and H fields, I need them for overlap ...
   calculations
5
6 fimmwave.fieldEX = load ("yourEXfile")
7 fimmwave.fieldEY = load ("yourEXfile")
8 fimmwave.fieldEZ = load ("yourEXfile")
9 fimmwave.fieldHX = load ("yourEXfile")
10 fimmwave.fieldHY = load ("yourEXfile")
11 fimmwave.fieldHZ = load ("yourEXfile")
12
13 %exported data is turned by 90 deg, no reason for that...
14 ofieldEX = transpose (fimmwave.fieldEX);
15 ofieldEY = transpose (fimmwave.fieldEY);
16 ofieldEZ = transpose (fimmwave.fieldEZ);
17 ofieldHX = transpose (fimmwave.fieldHX);
18 ofieldHY = transpose (fimmwave.fieldHY);
19 ofieldHZ = transpose (fimmwave.fieldHZ);
20
21 %finding the size of the matrix all should be the same
22 xsize = size(ofieldEX) (1);
23 ysize = size(ofieldEX) (2);
24
25 %deleting empty rows, in case the fields are complex, but show no ...
   loss
26
27 #ofield_del = ofield(1:2:xsize, 1:ysize);
28 ofield_delEX = ofieldEX;
29 ofield_delEY = ofieldEY;
30 ofield_delEZ = ofieldEZ;
```

```

31 ofield_delHX = ofieldHX;
32 ofield_delHY = ofieldHY;
33 ofield_delHZ = ofieldHZ;
34
35
36
37 waveguide_width=0.260;
38 waveguide_height=0.300;
39 %waveguide position middle of bottom, origin is top left, y axis ...
    goes down but is positive to make matrix handling easier
40 WGpos = [1,1];
41 %defining area of interest around the waveguide
42 %make sure the points don't lay on a border, that messes up the ...
    handling, remember that origin is top left and y goes down but ...
    is positive!!!!
43 # keep the waveguide in the middle of things
44 point1 = [-1,-1];
45 point2 = [1,1];
46 optical_cellsize_x = 2;
47 optical_cellsize_y = 2;
48 optical_resolution_x = size(ofield_delEX) (2)-1;
49 optical_resolution_y = size(ofield_delEX) (1)-1;
50 optical_stepsize_x = optical_cellsize_x / optical_resolution_x;
51 optical_stepsize_y = optical_cellsize_y / optical_resolution_y;
52
53
54 %moving the center of the waveguide bottom to the origin and ...
    cropping the matrix
55 % cell 1,1 is 0,2 in real coordinates
56 start_cell_pos = WGpos+point1;
57 end_cell_pos = WGpos+point2;
58 start_cell(1) = round(start_cell_pos(1)/optical_stepsize_x+1);
59 start_cell(2) = round(start_cell_pos(2)/optical_stepsize_y+1);
60 end_cell(1) = round(end_cell_pos(1)/optical_stepsize_x);
61 end_cell(2) = round(end_cell_pos(2)/optical_stepsize_y);
62
63 ofield_fixedEX = ofield_delEX(start_cell(2):end_cell(2), ...
    start_cell(1):end_cell(1));
64 ofield_fixedEY = ofield_delEY(start_cell(2):end_cell(2), ...
    start_cell(1):end_cell(1));
65 ofield_fixedHX = ofield_delHX(start_cell(2):end_cell(2), ...
    start_cell(1):end_cell(1));
66 ofield_fixedHY = ofield_delHY(start_cell(2):end_cell(2), ...
    start_cell(1):end_cell(1));
67
68 new_cell_length(1) = (size(ofield_fixedEX) (2)-1)*optical_stepsize_x;
69 new_cell_length(2) = (size(ofield_fixedEX) (1)-1)*optical_stepsize_y;
70 new_cell_start(1) = start_cell_pos(1);
71 new_cell_start(2) = start_cell_pos(2);

```

```

72 new_cell_end(1) = start_cell_pos(1) + ...
    (size(ofield.fixedEX)(2)-1)*optical_stepsize_x;
73 new_cell_end(2) = start_cell_pos(2) + ...
    (size(ofield.fixedEX)(1)-1)*optical_stepsize_y;
74
75
76 oX_grid_shift = ((new_cell_start(1) - WGpos(1)) : ...
    optical_stepsize_x : (new_cell_end(1)-WGpos(1)));
77 oY_grid_shift = ((new_cell_start(2)-WGpos(2)) : ...
    optical_stepsize_y : (new_cell_end(2) -WGpos(2)));
78 matrix_size = size(ofield.fixedEX);
79 xvector = size(oX_grid_shift);
80 yvector = size(oY_grid_shift);
81
82
83 #removing the waveguide, this assumes the wave guide is in the ...
    middle!, also the e and o matrix have to be the same size!
84
85 WG_bottom_left_cell = round([(matrix_size(2))/2-0.5 * ...
    waveguide_width /optical_stepsize_x, (matrix_size(1)-1)/2])
86 WG_top_right_cell = round([(matrix_size(2))/2+0.5 * ...
    waveguide_width /optical_stepsize_x, ((matrix_size(1)-1)/2) + ...
    waveguide_height/optical_stepsize_y])
87 WG_top_right_cell - WG_bottom_left_cell
88 ofield.fixedEX_noWG = ofield.fixedEX;
89 ofield.fixedEX_noWG (WG_bottom_left_cell(2) : ...
    WG_top_right_cell(2) , WG_bottom_left_cell(1) : ...
    WG_top_right_cell(1)) = 0;
90
91 ofield.fixedEY_noWG = ofield.fixedEY;
92 ofield.fixedEY_noWG (WG_bottom_left_cell(2) : ...
    WG_top_right_cell(2) , WG_bottom_left_cell(1) : ...
    WG_top_right_cell(1)) = 0;
93 ofield.fixedHX_noWG = ofield.fixedHX;
94 ofield.fixedHX_noWG (WG_bottom_left_cell(2) : ...
    WG_top_right_cell(2) , WG_bottom_left_cell(1) : ...
    WG_top_right_cell(1)) = 0;
95 ofield.fixedHY_noWG = ofield.fixedHY;
96 ofield.fixedHY_noWG (WG_bottom_left_cell(2) : ...
    WG_top_right_cell(2) , WG_bottom_left_cell(1) : ...
    WG_top_right_cell(1)) = 0;
97
98 #ofield.fixed_noWG (1:50,47:56) = 0;
99
100
101
102 #cutting out everthing but SiO2
103 ofield_onlyEXSiO2 = ofield.fixedEX;
104 ofield_onlyEXSiO2 ((round((matrix_size(1)) /2)): matrix_size(1) ...

```

```

    ,1:matrix_size(2)) = 0;
105 ofield_onlyEYSiO2 = ofield.fixedEY;
106 ofield_onlyEYSiO2 ((round((matrix_size(1))/2)):matrix_size(1) ...
    ,1:matrix_size(2)) = 0;
107 ofield_onlyHXSiO2 = ofield.fixedHX;
108 ofield_onlyHXSiO2 ((round((matrix_size(1))/2)):matrix_size(1) ...
    ,1:matrix_size(2)) = 0;
109 ofield_onlyHYSiO2 = ofield.fixedHY;
110 ofield_onlyHYSiO2 ((round((matrix_size(1))/2)):matrix_size(1) ...
    ,1:matrix_size(2)) = 0;
111
112 ofield_onlyEX_WG = (ofield.fixedEX - ofield.fixedEX.noWG);
113 ofield_onlyEX_EO = ofield.fixedEX.noWG - ofield_onlyEXSiO2;
114
115 ofield_onlyEY_WG = (ofield.fixedEY - ofield.fixedEY.noWG);
116 ofield_onlyEY_EO = ofield.fixedEY.noWG - ofield_onlyEYSiO2;
117
118 ofield_onlyHX_WG = (ofield.fixedHX - ofield.fixedHX.noWG);
119 ofield_onlyHX_EO = ofield.fixedHX.noWG - ofield_onlyHXSiO2;
120
121 ofield_onlyHY_WG = (ofield.fixedHY - ofield.fixedHY.noWG);
122 ofield_onlyHY_EO = ofield.fixedHY.noWG - ofield_onlyHYSiO2;
123
124 figure
125 pcolor(oX_grid.shift, oY_grid.shift, ofield_onlyEX_WG.^2)
126 shading interp
127 figure
128 pcolor(oX_grid.shift, oY_grid.shift, ofield_onlyEXSiO2.^2)
129 shading interp
130 figure
131 pcolor(oX_grid.shift, oY_grid.shift, ofield_onlyEX_EO.^2)
132 shading interp
133
134 ec = 2.654e-3;
135 #overlap_top_withE = trapz(trapz(ofield.fixed.noWG .* ...
    ofield.fixed.noWG .* interpo_field_calc ./100)) ;
136 overlap_top_inEO = ec/4*1.7*trapz(trapz(ofield_onlyEX_EO .* ...
    ofield_onlyEX_EO)) ;
137 overlap_top_inWG = ec/4*3.48*trapz(trapz(ofield_onlyEX_WG .* ...
    ofield_onlyEX_WG)) ;
138 overlap_top_inSiO2 = ec/4*1.44*trapz(trapz(ofield_onlyEXSiO2 .* ...
    ofield_onlyEXSiO2));
139 #overlap_bottom = overlap_top_inEO + overlap_top_inWG + ...
    overlap_top_inSiO2;
140 #overlap_bottom = 0.6527*trapz(trapz((1.7*ofield_onlyEX_EO + ...
    3.48*ofield_onlyEX_WG + 1.44*ofield_onlyEXSiO2) .* ...
    (ofield.fixedEX.noWG + ofield_onlyEX_WG + ofield_onlyEXSiO2)))
141 #overlap_bottom = trapz(trapz((ofield_onlyEO + ofield_onlyWG + ...
    ofield_onlySiO2) .* (ofield.fixed.noWG + ofield_onlyWG + ...

```

```

        ofield_onlySiO2)))
142
143
144 overlap_bottom = trapz(trapz(ofieldEX .* ofieldHY - ofieldEY .* ...
        ofieldHX));
145
146 S_top_inEO = trapz(trapz(ofield_onlyEX_EO .* ofield_onlyHY_EO - ...
        ofield_onlyEY_EO .* ofield_onlyHX_EO));
147 S_top_inSiO2 = trapz(trapz(ofield_onlyEXSiO2 .* ofield_onlyHYSiO2 ...
        - ofield_onlyEYSiO2 .* ofield_onlyHXSiO2));
148 S_top_inWG = trapz(trapz(ofield_onlyEX_WG .* ofield_onlyHY_WG - ...
        ofield_onlyEY_WG .* ofield_onlyHX_WG)) ;
149
150
151 #gammawithE = overlap_top_withE / overlap_bottom
152 gammainEO = overlap_top_inEO / overlap_bottom * 5.5444
153 gammainSiO2 = overlap_top_inSiO2 / overlap_bottom * 5.5444
154 gammainWG = overlap_top_inWG / overlap_bottom * 5.5444
155
156 fillinEO = S_top_inEO / overlap_bottom
157 fillinSiO2 = S_top_inSiO2 / overlap_bottom
158 fillinWG = S_top_inWG / overlap_bottom
159 #overlap = ofield_fixed_noWG .* ofield_fixed_noWG .* ...
        interpo_field_calc ./100 ;
160 #pcolor(oX_grid_shift, oY_grid_shift, overlap)
161 #shading interp
162
163 summ_gamma = gammainEO+gammainSiO2+gammainWG
164 summ_fill = fillinEO + fillinSiO2 + fillinWG
165 #figure
166 #pcolor(oX_grid_shift, oY_grid_shift, ofield_fixed)
167 #shading interp

```

## B.2 Electrical field handling

```

1 comsol_field = load ("yourfile.txt");
2 %here you load any field you want, the script is set to work with ...
        regular export data from Comsol
3 %here I define some geometry parameters
4 electrode_spacing = 1.999;
5 EO_height = 2.0001;
6 sio2height = 0;
7 left_border = -electrode_spacing/2;
8 right_border = electrode_spacing/2;
9

```

```

10 lower_border = sio2height;
11 upper_border = lower_border + EO.height;
12 x = comsol_field(:,1);
13 y = comsol_field(:,2);
14 z = comsol_field(:,3);
15
16
17 X_plot = ((left_border):0.1:(right_border));
18 Y_plot = ((lower_border):0.1:(upper_border));
19
20 interpo_field_plot = griddata(x,y,z,X_plot,Y_plot);
21 pcolor (X_plot, Y_plot, interpo_field_plot)
22 shading interp
23
24 grid_size_x = optical_stepsize_x;
25 grid_size_y = optical_stepsize_y;
26
27
28 # cutting out the right piece
29 X_calc = (left_border:grid_size_x:right_border);
30 Y_calc = (lower_border:grid_size_y:upper_border);
31
32 interpo_field_calc = griddata(x,y,z,X_calc,Y_calc);
33 # adjusting for waveguide offset
34
35 Y_calc = Y_calc-WGpos(2);
36
37 overall_mean = mean(mean(interpo_field_calc));
38
39 electricalfieldmatrixsize = size (interpo_field_calc);
40 opticalfieldmatrixsize = size (ofield_fixedEX);
41 #size (interpo_field_plot);
42
43 electricalcellsize = (right_border - left_border) * (upper_border ...
    - lower_border)
44
45
46
47 figure
48 pcolor (X_calc, Y_calc, interpo_field_calc)
49
50 interpo_field_calc = interpo_field_calc (1:500, 1:500);
51
52 gnuplotfield = interpo_field_calc / 100;
53 % for plotting
54 save ("youfile.txt", "gnuplotfield")
55 shading interp

```

### B.3 CPS capacitance calculations

```

1
2 % from Chen et. al , Trans MTT 1997, Vol. 45. No.6 , ...
   "Characteristics of
3 % coplanar transmission lines on multilayer substrates"
4 % Author Ram Voorakaranam, 8/21/13
5 %edited and expanded by Roland Himmelhuber 8/30/13
6 lear all;
7 close all;
8
9 epsilon1 = 1.0; % air
10 epsilon2 = 3; % topcladding sol-gel = 3.0
11 h2 = 2e-6; % top cladding thickness
12 epsilon3 = 1.0;
13 epsilon5 = 3.9; % SiO2 = 3.9
14 h5 = 1e-6; % oxide thickness
15 epsilon4 = 11.8; %Si = 11.8
16 h4 = 200e-6; %substrate height
17
18 subw = 500e-6; %substrate width
19 epsilon0 = 8.854e-12;
20
21 % CPW dimensions
22 w = 10e-6; %electrode width, note that this cannot be greater ...
   than substrate width
23 g = 2e-6; % electrode gap
24
25 w_min = w;
26 g_min = g;
27
28 w_max=350e-6;
29 g_max=10e-6;
30
31 w_step=10e-6;
32 g_step=1e-6;
33
34 number_of_steps_w = (w_max-w)/w_step;
35 number_of_steps_g = (g_max-g)/g_step;
36
37
38 for i=1:number_of_steps_w
39     g=g_min;
40     for j = 1:number_of_steps_g
41
42     xa = w/2;
43     xb = xa + g;

```

```

44 xc = subw/2;
45
46 sinhxa_h2 = sinh(pi*xa/(2*h2));
47 sinhxb_h2 = sinh(pi*xb/(2*h2));
48 sinhxc_h2 = sinh(pi*xc/(2*h2));
49 sinhxa_h4 = sinh(pi*xa/(2*h4));
50 sinhxb_h4 = sinh(pi*xb/(2*h4));
51 sinhxc_h4 = sinh(pi*xc/(2*h4));
52 sinhxa_h5 = sinh(pi*xa/(2*h5));
53 sinhxb_h5 = sinh(pi*xb/(2*h5));
54 sinhxc_h5 = sinh(pi*xc/(2*h5));
55 k0 = xc/xb * sqrt((xb^2-xa^2)/(xc^2-xa^2));
56 k2 = sinhxc_h2/sinhxb_h2 * sqrt((sinhxb_h2^2 - ...
    sinhxa_h2^2)/(sinhxc_h2^2 - sinhxa_h2^2));
57 k4 = sinhxc_h4/sinhxb_h4 * sqrt((sinhxb_h4^2 - ...
    sinhxa_h4^2)/(sinhxc_h4^2 - sinhxa_h4^2));
58 k5 = sinhxc_h5/sinhxb_h5 * sqrt((sinhxb_h5^2 - ...
    sinhxa_h5^2)/(sinhxc_h5^2 - sinhxa_h5^2));
59
60 % k0 = s/(s+g);
61 % k1 = sinh(pi*s/(2*h1))/sinh(pi*(s+g)/(2*h1));
62 % k2 = sinh(pi*s/(2*H))/sinh(pi*(s+g)/(2*H));
63 k0p = sqrt(1-k0^2);
64 k2p = sqrt(1-k2^2);
65 k4p = sqrt(1-k4^2);
66 k5p = sqrt(1-k5^2);
67
68 % complete elliptical integrals
69 K_k0 = ellipke(k0);
70 K_k2 = ellipke(k2);
71 K_k4 = ellipke(k4);
72 K_k5 = ellipke(k5);
73 K_k0p = ellipke(k0p);
74 K_k2p = ellipke(k2p);
75 K_k4p = ellipke(k4p);
76 K_k5p = ellipke(k5p);
77
78 %partial capacitances for
79 C0_CPW = 4*epsilon0*K_k0p/K_k0;
80 C1 = 0;
81 C2 = 2*epsilon0*(epsilon2-1)*K_k2p/K_k2;
82 C3 = 0;
83 C4 = 2*epsilon0*(epsilon4-1)*K_k4p/K_k4;
84 C5 = 2*epsilon0*(epsilon5-epsilon4)*K_k5p/K_k5;
85
86 C_CPW= C0_CPW+C1+C2+C3+C4+C5;
87 epsilon_eff_CPW = C_CPW/C0_CPW;
88 vpfrac = 1/sqrt(epsilon_eff_CPW);
89 vph = 3e8*vpfrac;

```

```

90 Z0_CPW = 30*pi/sqrt(epsilon_eff_CPW)*K.k0/K.k0p;
91
92 C_CPW_scan(i,j)=C_CPW;
93 Z0_CPW_scan(i,j)=Z0_CPW;
94
95 % CPS
96 k0 = xa/xb;
97 %k0 = sqrt( 1 - (xa^2/xb^2) );
98 k0p = sqrt(1-k0);
99 %k0p = xa/xb;
100 k2 = sqrt( 1 - (sinhxa.h2^2)/(sinhxb.h2^2));
101 k4 = sqrt( 1 - (sinhxa.h4^2)/(sinhxb.h4^2));
102 k5 = sqrt( 1 - (sinhxa.h5^2)/(sinhxb.h5^2));
103 k2p = sqrt(1-k2^2);
104 k4p = sqrt(1-k4^2);
105 k5p = sqrt(1-k5^2);
106 % complete elliptical integrals
107 K.k0 = ellipke(k0);
108 K.k4 = ellipke(k4);
109 K.k5 = ellipke(k5);
110 K.k0p = ellipke(k0p);
111 K.k4p = ellipke(k4p);
112 K.k5p = ellipke(k5p);
113 epsilon_eff_CPS = 1 + 0.5 * (epsilon2 - 1) * K.k0 / K.k0p * ...
    K.k2p / K.k2 + 0.5 * (epsilon4 - 1) * K.k0 / K.k0p * K.k4p / ...
    K.k4 + 0.5 * (epsilon5 - epsilon4) * K.k0 / K.k0p * K.k5p / K.k5;
114
115 %C0 = epsilon0*K.k0/K.k0p %from Chen this is wrong
116 C0 = epsilon0*K.k0p/K.k0; % from LINE CAPACITANCE AND IMPEDANCE ...
    OF COPLANAR-STRIP WAVEGUIDES ON SUBSTRATES WITH MULTIPLE ...
    DIELECTRIC LAYERS S. Gevorgian 1,2 and H. Bergl
117
118 %w_step=5e-6;
119 C_CPS = epsilon_eff_CPS * C0;
120 vpfrac = 1/sqrt(epsilon_eff_CPS);
121 vph = 3e8*vpfrac;
122 Z0_CPS = 120*pi/sqrt(epsilon_eff_CPS)*K.k0p/K.k0;
123
124 C_CPS_scan(i,j)=C_CPS;
125 Z0_CPS_scan(i,j)=Z0_CPS;
126
127 %added by me for calculating bandwith
128 R_Au = 22.14e-9; %resistance of gold in Ohm*m
129 e_length = 2e-3; %electrode length in m
130 e_height = 2e-6; %electroed hight in m
131
132 R_e = R_Au/(e.height*w)*e.length; %resistance of electrode
133
134 bandwidth_CPW = 1/(R_e * C_CPW)/1e9; %bandwith in GHz

```

```

135 bandwidth_CPS = 1/(R_e * C_CPS)/1e9; %bandwith in GHz
136
137 bandwidth_CPW_scan(i,j)=bandwidth_CPW;
138 bandwidth_CPS_scan(i,j)=bandwidth_CPS;
139
140 g_scan(j) = g;
141 g=g+g_step;
142
143 endfor
144 w_scan(i) = w;
145 w=w+w_step;
146
147 endfor
148
149 %plot (w_scan*1e6,bandwidth_CPW_scan)
150 %title ('CPW')
151 %xlabel ('Electrode Width ( m)')
152 %ylabel ('Bandwidth (GHz)')
153 %legend ('2um spacing','4um spacing','6um spacing','8um ...
           spacing','10um spacing', "location", "north")
154
155 %figure
156 %plot (w_scan*1e6,bandwidth_CPS_scan)
157 %title ('CPS')
158 %xlabel ('Electrode Width ( m)')
159 %ylabel ('Bandwidth (GHz)')
160 %legend ('2um spacing','4um spacing','6um spacing','8um ...
           spacing','10um spacing', "location", "north")
161
162 %figure
163 %plot (w_scan*1e6,Z0_CPS_scan)
164 %title ('CPS')
165 %xlabel ('Electrode Width ( m)')
166 %ylabel ('Z_0 (Ohm)')
167 %legend ('2um spacing','4um spacing','6um spacing','8um ...
           spacing','10um spacing', "location", "north")
168
169
170 %figure
171 %plot (w_scan*1e6,Z0_CPW_scan)
172 %title ('CPW')
173 %xlabel ('Electrode Width ( m)')
174 %ylabel ('Z_0 (Ohm)')
175 %legend ('2um spacing','4um spacing','6um spacing','8um ...
           spacing','10um spacing', "location", "north")
176
177
178 figure
179 plot (w_scan*1e6,C_CPS_scan*1e10)

```

```

180 title ('CPS')
181 xlabel ('Electrode Width ( m)')
182 ylabel ('C (pF/cm)')
183 legend ('2um spacing','3um spacing','4um spacing','5um ...
         spacing','6um spacing','7um spacing','8um spacing', ...
         "location", "north")
184
185 w_scan=w_scan';
186 save ("yourfile'", "C_CPS_scan");
187 save ("yourfile", "w_scan");

```

## B.4 Electrode loss calculations

```

1
2 clear
3 c = 299792458; %speed of light in m/s
4 f = [0.5e9:.1e9:100e9]; %frequency in Hz
5 %f = 1e9;
6 wavelength = c./f;
7 R_Au = 22.14e-9; %resistance of gold in Ohm*m 22.14e-9 for Au, ...
   1.72e-8
8 w = 50e-6; %electrode width in m
9 s = 1.5e-6; %gapwidth in m
10 d = 2*w+s;
11 kp = sqrt(1-(s/d)^2);
12 K = ellipke(kp);
13 t = 2e-6; %electrode thickness
14 mu_0 = 4*pi*1e-7;
15 h = 100e-6;
16 Z_0 = 217.5;
17 d_Z = 1;
18 C = 3.73E-011;
19 e_eff = 5.9154;
20
21 skin_depth = sqrt(pi*R_Au./(f.*mu_0));
22 sheet_resistance = R_Au./skin_depth;
23
24 one = 1-(s/d)
25 two = t*(1+(s/d))
26 ln1 = log((4*pi*s*one/two))
27 ln2 = log((4*pi*d*one/two))
28
29 first = 8.686*sheet_resistance./(0.4*d*Z_0*K^2*(1-(s/d)^2));
30 second = (2*d/s*(pi + ln1))
31 third = 2*(pi+ln2)

```

```

32
33 %alpha_c1 = 8.686*sheet_resistance./(0.4*d*Z_0*K^2*(1-(s/d)^2)) * ...
    (2*d/s*(pi + ln1) + 2*(pi+ln2)); %in dB/m
34 alpha_c = first .* (second + third); %in dB/m
35 %plot(f,lambda_c)
36
37 tan_Δ = 1e-3;
38
39 alpha_d = 0.91*tan_Δ.*f/1e9*sqrt(e_eff);
40 %figure
41 %plot(f,lambda_d)
42 plot (f/1e9,alpha_c/100,f/1e9,alpha_d,f/1e9,(alpha_c/100+alpha_d))
43 xlabel ('Frequency (GHz)')
44 ylabel ('loss (dB/cm)')
45 legend ('Conductor','Dielectrid','Both')
46 total_loss = alpha_c/100+alpha_d;
47
48 save ("yourfile", "total_loss");
49 save ("yourfile", "f");
50
51 s_over_h=s/h
52 w_over_h=w/h

```

## B.5 Reflection correction factor calculations

```

1 clear all
2
3 z=[0:0.5:6]; %SiO2 thickness
4 NA=0.6;
5 lambda_f=1.56;
6 lambda_s=0.5*lambda_f;
7 air = 1;
8 n0_f=1.487; %sg
9 n1_f=1.710; %eo
10 n2_f=1.44; %sio2
11 n3_f=3.47+i*1.1e-6; %si
12
13
14 %n1_s = [0.6:0.05:1.8];
15
16 n0_s = 1.495;%sg
17 n1_s = 1.490+i*0.181;%eo
18 n2_s = 1.46;%sio2
19 n3_s = 3.7+i*7.47e-3;%si
20 %relections

```

```

21
22 %I0 = 1-abs(((n0_f-air)/(n0_f+air))).^2 %from air to sol gel
23 If0 = 1-abs(((n1_f-air)/(n1_f+air))).^2; % from air to EO
24
25 %If0= I0-abs(((n0_f-n1_f)/(n0_f+n1_f))).^2 %from sol gel to EO
26
27 If1= If0*abs(((n1_f-n2_f)/(n1_f+n2_f))).^2 ;%fundamental power ...
    reflected from Si02
28 If2= (If0-2*If1)*abs(((n2_f-n3_f)/(n2_f+n3_f))).^2 ;%fundamental ...
    power reflected from Si
29
30 Is0 = If0^2; %SH generated forward by If0
31 Is0p = Is0.*abs(((n1_s-n2_s)./(n1_s+n2_s))).^2 ;%SH power ...
    reflected from Si02
32 Is1 = (If1)^2 ;% backward generated SH from If1
33 Is2 = (Is0-2*Is0p)*abs(((n2_s-n3_s)./(n2_s+n3_s))).^2; %SH power ...
    reflected from Si
34 Is3 = (If2)^.2; % backward generated SH from If2
35
36 increase_fromAu.electrodes = (0.97^2+0.524)/(Is0p+Is1)
37
38
39 w0=lambda_f/pi/NA;
40 w0_s=lambda_s/pi/NA;
41 z0_1550=pi*w0^2/lambda_f;
42 z0_s=pi*w0_s^2/lambda_s;
43
44
45 w_1550=sqrt(w0^2.*(1+(z./z0_1550).^2));
46 w_s=sqrt(w0_s^2.*(1+(z./z0_s).^2));
47 w_s2=sqrt(w0_s^2.*(1+(2*z./z0_s).^2));
48
49 %calculating the agular spread
50
51 gkat_1550 = (w_1550-w0)./2;
52 angle_1550 = atan(gkat_1550./z)./2./pi.*360;
53 angle_1550c = atan(gkat_1550./z);
54
55 gkat_s = (w_s+w0_s)./2;
56 angle_s = atan(gkat_s./z)./2./pi.*360;
57 angle_sc = atan(gkat_s./z);
58
59 gkat_2s = (w_s2+w0_s)./2;
60 angle_2s = atan(gkat_2s./z)./2./pi.*360;
61 angle_2sc = atan(gkat_2s./z);
62
63 %plot(z,angle_1550, z, angle_s)
64 %legend('1550','s')
65

```

```

66
67 %reflection with angles
68 %air
69 n1=air;
70 n2=n0_f;
71
72 I0 = 1-abs((n1 .* cos(angle_1550c) - n2 .* sqrt(1 - (n1 ./ n2 .* ...
      sin(angle_1550c)).^2)) ./ (n1 .*cos(angle_1550c) + n2 .*sqrt(1 ...
      - (n1 ./n2 .*sin(angle_1550c)).^2) ) ).^ 2 ;%from air to sol ...
      gel s
73 %I0 = 1-abs((n1 .*sqrt(1-(n1./n2.*sin(angle_1550c)).^2) - ...
      n2.*cos(angle_1550c)) ./ ...
      (n1.*sqrt(1-(n1./n2.*sin(angle_1550c)).^2) + ...
      n2.*cos(angle_1550c))) .^2;%from air to sol gel p
74
75
76 n1=n0_f;
77
78 n2=n1_f;
79
80 If0 = I0-abs((n1.*cos(angle_1550c)-n2 .* ...
      sqrt(1-(n1./n2.*sin(angle_1550c)).^2)) ./ ...
      (n1.*cos(angle_1550c) + n2.*sqrt(1 - ...
      (n1./n2.*sin(angle_1550c)).^2))).^2 ;%from solgel to eo s
81 %I0 = 1-abs((n1.*sqrt(1 - (n1./n2.*sin(angle_1550c)).^2) - ...
      n2.*cos(angle_1550c)) ./ (n1.*sqrt(1 - ...
      (n1./n2.*sin(angle_1550c)).^2) + n2 .* cos(angle_1550c))) ...
      .^2;%from sol gel to eo p
82 n1=air;
83 n2=n1_f;
84
85 %If0 = 1-abs((n1 .*cos(angle_1550c) - n2 .*sqrt(1 - (n1 ./ ...
      n2.*sin(angle_1550c)).^2)) ./ (n1.*cos(angle_1550c) + ...
      n2.*sqrt(1 - (n1./n2.*sin(angle_1550c)).^2))).^2 ;%from air to eo
86
87 %fundamental power reflected from Si02
88 n1=n1_f;
89 n2=n2_f;
90
91 If = abs((n1.*cos(angle_1550c)- n2 .*sqrt(1 - ...
      (n1./n2.*sin(angle_1550c)).^2)) ./ (n1.*cos(angle_1550c) + ...
      n2.*sqrt(1 - (n1./n2.*sin(angle_1550c)).^2))).^2 ;%s
92 %If = abs((n1.*sqrt(1 - (n1./n2.*sin(angle_1550c)).^2) - ...
      n2.*cos(angle_1550c)) ./ (n1.*sqrt(1 - ...
      (n1./n2.*sin(angle_1550c)).^2) + n2.*cos(angle_1550c))).^2;%p
93
94 If1= If0.*If;
95
96 %fundamental power reflected from Si

```

```

97
98 n1=n2_f;
99 n2=n3_f;
100
101 If = abs((n1.*cos(angle_1550c) - n2.*sqrt(1 - ...
      (n1./n2.*sin(angle_1550c)).^2)) ./ (n1.*cos(angle_1550c) + ...
      n2.*sqrt(1 - (n1./n2.*sin(angle_1550c)).^2))).^2;%s
102 %If = abs((n1.*sqrt(1-(n1 ./ n2.*sin(angle_1550c)).^2) - ...
      n2.*cos(angle_1550c)) ./ (n1.*sqrt(1 - ...
      (n1./n2.*sin(angle_1550c)).^2) + n2.*cos(angle_1550c))).^2;%p
103
104 If2= (If0-2.*If1).*If;
105
106 Is0 = If0.^2; %SH generated forward by If0
107
108 %SH power reflected from Si02
109 n1=n1_s;
110 n2=n2_s;
111
112 If = abs((n1.*cos(angle_sc) - n2.*sqrt(1 - (n1 ...
      ./n2.*sin(angle_sc)).^2)) ./ (n1.*cos(angle_sc) + n2.*sqrt(1 ...
      - (n1./n2.*sin(angle_sc)).^2))).^2;%s
113 %If = abs((n1.*sqrt(1-(n1 ./n2.*sin(angle_sc)).^2) - n2 ...
      .*cos(angle_sc)) ./ (n1 .* sqrt(1 - (n1 ./ ...
      n2.*sin(angle_sc)).^2) + n2 .*cos(angle_sc))).^2;%p
114
115 Is0p = Is0.*If;
116
117 Is1 = (If1).^2; % backward generated SH from If1
118
119
120 %SH power reflected from Si
121 n1 = n2_s;
122 n2=n3_s;
123
124 If = abs((n1.*cos(angle_sc) - n2.*sqrt(1-(n1 ./ ...
      n2.*sin(angle_sc)).^2)) ./ (n1.*cos(angle_sc)+n2.*sqrt(1 - ...
      (n1./n2.*sin(angle_sc)).^2))).^2;%s
125 %If = abs((n1.*sqrt(1-(n1 ./ ...
      n2.*sin(angle_sc)).^2)-n2.*cos(angle_sc)) ./ (n1.*sqrt(1-(n1 ...
      ./ n2.*sin(angle_sc)).^2) +n2 .*cos(angle_sc))).^2;%p
126 Is2 = (Is0-2*Is0p).*If;
127
128 Is3 = (If2).^2; % backward generated SH from If2
129
130
131
132 %with gaussian beam parameters
133

```

```

134 If1g = If1;
135 If2g = If2.*(w0./w.1550).^2;
136
137 Is0pg = Is0p; %SH power reflected from SiO2;
138 Is0pg = Is0pg * (1-abs(((n1_s-air)/(n1_s+air))).^2); % from EO to air
139 %Is0pg = Is0pg * (1-abs(((n1_s-n0_s)/(n1_s+n0_s))).^2); % from EO ...
    to solgel
140 %Is0pg = Is0pg * (1-abs(((n0_s-air)/(n0_s+air))).^2) % from ...
    solgel to air
141
142 Is1g = Is1; %backward generated SH from If1;
143 Is1g = Is1g * (1-abs(((n1_s-air)/(n1_s+air))).^2); % from EO to air
144 %Is1g = Is1g * (1-abs(((n1_s-n0_s)/(n1_s+n0_s))).^2); % from EO ...
    to solgel
145 %Is1g = Is1g * (1-abs(((n0_s-air)/(n0_s+air))).^2) % from solgel ...
    to air
146
147 Is2g = Is2.*(w0./w.s2).^2; %SH power reflected from Si
148 Is2g = Is2g * (1-abs(((n1_s-air)/(n1_s+air))).^2); % from EO to air
149 %Is2g = Is2g * (1-abs(((n1_s-n0_s)/(n1_s+n0_s))).^2); % from EO ...
    to solgel
150 %Is2g = Is2g * (1-abs(((n0_s-air)/(n0_s+air))).^2) % from solgel ...
    to air
151
152
153 Is3g = (If2g).^2; % backward generated SH from If2g
154 Is3g = Is3g * (1-abs(((n1_s-air)/(n1_s+air))).^2); % from EO to air
155 %Is3g = Is3g * (1-abs(((n1_s-n0_s)/(n1_s+n0_s))).^2); % from EO ...
    to solgel
156 %Is3g = Is3g * (1-abs(((n0_s-air)/(n0_s+air))).^2) % from solgel ...
    to air
157
158
159
160 Firstpeak = Is0pg+Is1g+Is2g;
161 Secondpeak = Is3g;
162
163 Peak_ratio = Secondpeak./Firstpeak;
164 calibration_ratio = Is0pg./(Firstpeak+Secondpeak);
165
166 r33=34*0.83*(sqrt(395*calibration_ratio));
167
168 calibration = [z;calibration_ratio];
169 calibration = transpose (calibration);
170 plot (calibration)
171
172
173
174 save ("youfile ", "calibration");

```

## Appendix C

### FABRICATION DESCRIPTIONS

#### C.1 Electrode Fabrications by lift off

Substrates were cleaned by oxygen plasma for 5 min. AZ5214 IR photoresist was spun at  $4000 \text{ min}^{-1}$  for 45 sec. The resist films were baked at  $110^\circ\text{C}$  for 50s and exposed (on the MA6) for 10s at an intensity of  $1.7 \text{ mJcm}^{-2}$  measured at 240nm. Reversal bake was carried out at  $120^\circ\text{C}$  for 90s on a stainless steel hotplate. Both hotplates should be at the required temperature for at least 20min before processing, to ensure reproducible results. The films were then flood exposed for 3 min and developed in AZ400K (1:4 deluted with water) for 40(for silicon substrates) to 45s (silica substrates)min.

## REFERENCES

- [1] C. F. Brinker and G. W. Scherer, *SolGel Science*. Academic Press, 1990.
- [2] R. Himmelhuber, C. C. DeRose, R. A. Norwood, and N. Peyghambarian, “Uv-patternable inorganic-organic hybrid materials tailored for use in electro-optic modulators,” in *Photonic Devices+ Applications*. International Society for Optics and Photonics, 2008, pp. 70 490G–70 490G.
- [3] R. Dinu, D. Jin, D. Huang, M. K. Koenig, A. M. Barklund, Y. Fang, T. C. Parker, Z. Shi, J. Luo, and A. K. Jen, “Low-voltage electro-optic polymer modulators,” in *Defense and Security Symposium*. International Society for Optics and Photonics, 2006, pp. 62 430G–62 430G.
- [4] Y. Enami, G. Meredith, N. Peyghambarian, and A.-Y. Jen, “Hybrid electro-optic polymer/sol–gel waveguide modulator fabricated by all-wet etching process,” *Applied physics letters*, vol. 83, no. 23, pp. 4692–4694, 2003.
- [5] C. T. DeRose, Y. Enami, C. Loychik, R. A. Norwood, D. Mathine, M. Fallahi, N. Peyghambarian, J. D. Luo, A. K. Y. Jen, M. Kathaperumal, and M. Yamamoto, “Pockel’s coefficient enhancement of poled electro-optic polymers with a hybrid organic-inorganic sol-gel cladding layer,” *App.Phys. Lett.*, vol. 89, no. 13, SEP 25 2006.
- [6] Y. Enami, C. T. Derose, D. Mathine, C. Loychik, C. Greenlee, R. A. Norwood, T. D. Kim, J. Luo, Y. Tian, A. K. Y. Jen, and N. Peyghambarian, “Hybrid polymer/sol-gel waveguide modulators with exceptionally large electro-optic coefficients,” *Nature Photonics*, vol. 1, no. 3, pp. 180–185, MAR 2007.
- [7] R. Buestrich, F. Kahlenberg, M. Popall, A. Martin, and O. Rsch, “Low si-oh ormocer s for dielectrical and optical interconnection technology,” in *Mat.Res.Symp.Proc.*, 2000, p. CC9.8.1CC9.8.6.
- [8] O. Soppera, P. Moreira, A. Leite, and P. Marques, “Low-loss photopatternable hybrid solgel materials,” *Journal of Sol-Gel Science and Technology*, vol. 35, no. 1, pp. 27–39, 2005. [Online]. Available: <http://dx.doi.org/10.1007/s10971-005-3212-1>
- [9] O. Soppera, P. Moreira, P. Marques, and A. Leite, “Influence of temperature and environment humidity on the transmission spectrum of solgel hybrid channel waveguides,” *Optics Communications*, vol. 271, no. 2, pp. 430 – 435, 2007. [Online]. Available: <http://www.sciencedirect.com/science/article/pii/S0030401806011758>

- [10] R. Houbertz, G. Domann, J. Schulz, B. Olsowski, L. Frhlich, and W.-S. Kim, "Impact of photoinitiators on the photopolymerization and the optical properties of inorganicorganic hybrid polymers," *Applied Physics Letters*, vol. 84, no. 7, pp. 1105–1107, 2004. [Online]. Available: <http://scitation.aip.org/content/aip/journal/apl/84/7/10.1063/1.1647706>
- [11] K. Viswanathan, C. E. Hoyle, E. S. Jnsson, C. Nason, and K. Lindgren, "Effect of amine structure on photoreduction of hydrogen abstraction initiators," *Macromolecules*, vol. 35, no. 21, pp. 7963–7967, 2002. [Online]. Available: <http://pubs.acs.org/doi/abs/10.1021/ma0120308>
- [12] C.-C. Teng, "Precision measurements of the optical attenuation profile along the propagation path in thin-film waveguides," *Appl. Opt.*, vol. 32, no. 7, pp. 1051–1054, Mar 1993. [Online]. Available: <http://ao.osa.org/abstract.cfm?URI=ao-32-7-1051>
- [13] H. Sayilkan, S. Sener, and E. Arpac, "Zirconium tetra-n-butylate modified with different organic acids: Hydrolysis and polymerization of the products," *Journal of Inorganic and Organometallic Polymers*, vol. 5, no. 4, pp. 409–423, 1995. [Online]. Available: <http://dx.doi.org/10.1007/BF01193063>
- [14] M. Hesse, H. Meier, and B. Zeeh, *Spectroscopic Methods in Organic Chemistry*, 2nd ed. Thieme, 2008.
- [15] R. Himmelhuber, P. Gangopadhyay, R. A. Norwood, D. A. Loy, N. Peyghambarian *et al.*, "Titanium oxide sol-gel films with tunable refractive index," *Optical Materials Express*, vol. 1, no. 2, pp. 252–258, 2011.
- [16] C. Guan, C.-L. L, Y.-F. Liu, and B. Yang, "Preparation and characterization of high refractive index thin films of tio<sub>2</sub>/epoxy resin nanocomposites," *Journal of Applied Polymer Science*, vol. 102, no. 2, pp. 1631–1636, 2006. [Online]. Available: <http://dx.doi.org/10.1002/app.23947>
- [17] P. Chrysicopoulou, D. Davazoglou, C. Trapalis, and G. Kordas, "Optical properties of sio<sub>2</sub>-tio<sub>2</sub> sol-gel thin films," *Journal of materials science*, vol. 39, no. 8, pp. 2835–2839, 2004.
- [18] C. Gonzalez-Oliver, P. F. James, and H. Rawson, "Silica and silica-titania glasses prepared by the sol-gel process," *Journal of Non-Crystalline Solids*, vol. 48, no. 1, pp. 129–152, 1982.
- [19] Z. Wang, U. Helmersson, and P.-O. Käll, "Optical properties of anatase tio<sub>j</sub> sub<sub>i</sub> 2<sub>i</sub>/sub<sub>i</sub> thin films prepared by aqueous sol-gel process at low temperature," *Thin Solid Films*, vol. 405, no. 1, pp. 50–54, 2002.

- [20] A. Antonello, M. Guglielmi, V. Bello, G. Mattei, A. Chiasera, M. Ferrari, and A. Martucci, "Titanate nanosheets as high refractive layer in vertical microcavity incorporating semiconductor quantum dots," *The Journal of Physical Chemistry C*, vol. 114, no. 43, pp. 18 423–18 428, 2010.
- [21] A. E. Gash, T. M. Tillotson, J. H. Satcher, J. F. Poco, L. W. Hrubesh, and R. L. Simpson, "Use of epoxides in the sol-gel synthesis of porous iron (iii) oxide monoliths from fe (iii) salts," *Chemistry of Materials*, vol. 13, no. 3, pp. 999–1007, 2001.
- [22] B. Damin, J. Garapon, and B. Sillion, "A convenient synthesis of chlorohydrins using chloramine t," *Synthesis*, vol. 1981, no. 05, pp. 362–363, 1981.
- [23] D. Rakhmankulov, N. E. Maksimova, R. Karakhanov, E. A. Kantor, M. Bartok, and S. S. Zlotskii, "Chemistry of 1,3-bifunctional systems. 20. synthesis and thiolysis of sulfur-containing 1,3-dioxacyclanes," *Acta. Phys. Chem.*, vol. 21, pp. 177–180, 1975.
- [24] J. G. Erickson, "Method of preparing glycidyl ester," Sep. 11 1951, uS Patent 2,567,842.
- [25] "Advanced chemistry development (acd/labs) software," 19942010.
- [26] R. Deschenaux and J. K. Stille, "Transition-metal-catalyzed asymmetric organic synthesis via polymer-attached optically active phosphine ligands. 13. asymmetric hydrogenation with polymer catalysts containing primary and chiral secondary pendant alcohols," *J. Org. Chem.*, vol. 50, no. 13, pp. 2299–2302, 1985.
- [27] A. Mohammad, D. Satchell, and R. Satchell, "Quantitative aspects of lewis acidity. part viii. the validity of infrared carbonyl shifts as measures of lewis acid strength. the interaction of lewis acids and phenalen-1-one (perinaphthenone)," *J. Chem. Soc. B*, pp. 723–725, 1967.
- [28] SDBSWeb:, "<http://riodb01.ibase.aist.go.jp/sdbs/> national institute of advanced industrial science and technology, september 16, 2010."
- [29] M. Zhao, X. Gu, S. E. Lowther, C. Park, Y. C. Jean, and T. Nguyen, "Subsurface characterization of carbon nanotubes in polymer composites via quantitative electric force microscopy," *Nanotechnology*, vol. 21, no. 22, p. 225702, 2010. [Online]. Available: <http://stacks.iop.org/0957-4484/21/i=22/a=225702>
- [30] C. Riedel, R. Arinero, P. Tordjeman, G. L ev eque, G. Schwartz, A. Alegria, and J. Colmenero, "Nanodielectric mapping of a model polystyrene-poly (vinyl acetate) blend by electrostatic force microscopy," *Physical Review E*, vol. 81, no. 1, p. 010801, 2010.

- [31] R. A. Parker, "Static dielectric constant of rutile ( $\text{TiO}_2$ ), 1.6-1060 k," *Physical Review*, vol. 124, no. 6, p. 1719, 1961.
- [32] J. Brandup and E. H. Immergut, Eds., *Polymer Handbook*. Wiley, 1975.
- [33] R. Himmelhuber, S. S. Mehravar, O. D. Herrera, V. Demir, K. Kieu, J. Luo, A. K.-Y. Jen, R. A. Norwood, and N. Peyghambarian, "Characterization of coplanar poled electro optic polymer films for si-photonic devices with multiphoton microscopy," *Applied Physics Letters*, vol. 104, no. 16, pp. –, 2014. [Online]. Available: <http://scitation.aip.org/content/aip/journal/apl/104/16/10.1063/1.4872165>
- [34] T. Goodson, S. Gong, and C. Wang, "Nonlinear-optical susceptibility of a model guest-host polymeric system as investigated by electrooptics and 2nd-harmonic generation," *Macromolecules*, vol. 27, no. 15, pp. 4278–4283, JUL 18 1994.
- [35] J. S. Schildkraut, "Determination of the electrooptic coefficient of a poled polymer film," *Applied optics*, vol. 29, no. 19, pp. 2839–2841, 1990.
- [36] S. J. Benight, D. H. Bale, B. C. Olbricht, and L. R. Dalton, "Organic electro-optics: Understanding material structure/function relationships and device fabrication issues," *Journal of Materials Chemistry*, vol. 19, no. 40, pp. 7466–7475, 2009.
- [37] A. Nahata, C. WU, and J. Yardley, "Electrooptic characterisation of organic media," *IEEE T. Instrum Meas.*, vol. 41, no. 1, pp. 128–131, FEB 1992, 8th Annual Conf On The Instrumentation And Measurement Technology ( Imtc/91 ), Atlanta, Ga, May 14-16, 1991.
- [38] G. Martin, E. Toussaere, L. Soulier, and J. Zyss, "Reflection second harmonic generation scanning microscope," *Synthetic Met.*, vol. 127, no. 1-3, SI, pp. 105–109, MAR 26 2002, E-MRS 2001 Spring Meeting, Strasbourg, France, Jun 05-08, 2001.
- [39] J. Beermann, S. Bozhevolnyi, K. Pedersen, and J. Fage-Pedersen, "High-resolution second-harmonic microscopy of poled silica waveguides," *Opt. Commun.*, vol. 221, no. 4-6, pp. 295–300, JUN 15 2003.
- [40] R. Loucif-Saibi, K. Nakatani, J. Delair, M. Dumont, and Z. Sekkat, "Photoisomerization and second harmonic generation in disperse red one-doped and -functionalized poly(methyl methacrylate) films," *Chem. Mater.*, vol. 5, no. 2, pp. 229–236, FEB 1993.

- [41] D. Sandkuijl, A. E. Tuer, D. Tokarz, J. E. Sipe, and V. Barzda, "Numerical second- and third-harmonic generation microscopy," *J. Opt. Soc. Am. B*, vol. 30, no. 2, pp. 382–395, FEB 2013.
- [42] K. Kieu and M. Mansuripur, "Femtosecond laser pulse generation with a fiber taper embedded in carbon nanotube/polymer composite," *Opt. Lett.*, vol. 32, no. 15, pp. 2242–2244, AUG 1 2007.
- [43] K. Kieu, S. Mehravar, R. Gowda, R. A. Norwood, and N. Peyghambarian, "Label-free multi-photon imaging using a compact femtosecond fiber laser mode-locked by carbon nanotube saturable absorber," *Biomed. Opt. Express*, vol. 4, no. 10, pp. 2187–2195, Oct 2013. [Online]. Available: <http://www.opticsinfobase.org/boe/abstract.cfm?URI=boe-4-10-2187>
- [44] F. Kajzar and J. Swalen, Eds., *Organic Thin Films for Waveguiding Nonlinear Optics*. Gordon and Breach Publishers, 1996.
- [45] I. H. Malitson, "Interspecimen comparison of the refractive index of fused silica," *J. Opt. Soc. Am.*, vol. 55, no. 10, pp. 1205–1208, Oct 1965. [Online]. Available: <http://www.opticsinfobase.org/abstract.cfm?URI=josa-55-10-1205>
- [46] *Handbook of optical constants of solids*. Academic Press, 1997.
- [47] R. Himmelhuber, O. D. Herrera, R. Voorakaranam, L. Li, A. M. Jones, R. A. Norwood, J. Luo, A. K.-Y. Jen, N. Peyghambarian *et al.*, "A silicon-polymer hybrid modulator design, simulation and proof of principle," *IEEE/OSA Journal of Lightwave Technology*, vol. 31, no. 24, pp. 4067–4072, 2013.
- [48] G. Khanarian, D. Allen, C. Walton, H. Goldberg, and J. B. Stamatoff, "Electro-optic characterization of nonlinear-optical guest-host films and polymers," *J. Opt. Soc. Am. B*, vol. 13, no. 9, pp. 1927–1934, Sep 1996. [Online]. Available: <http://josab.osa.org/abstract.cfm?URI=josab-13-9-1927>
- [49] E. L. Wooten, K. M. Kissa, A. Yi-Yan, E. J. Murphy, D. A. Lafaw, P. F. Hallemeier, D. Maack, D. V. Attanasio, D. J. Fritz, G. J. McBrien *et al.*, "A review of lithium niobate modulators for fiber-optic communications systems," *Selected Topics in Quantum Electronics, IEEE Journal of*, vol. 6, no. 1, pp. 69–82, 2000.
- [50] D. E. Zelmon, D. L. Small, and D. Jundt, "Infrared corrected sellmeier coefficients for congruently grown lithium niobate and 5 mol.% magnesium oxide -doped lithium niobate," *J. Opt. Soc. Am. B*, vol. 14, no. 12, pp. 3319–3322, Dec 1997. [Online]. Available: <http://josab.osa.org/abstract.cfm?URI=josab-14-12-3319>

- [51] T. Findakly and M. Bramson, "High-performance integrated-optical chip for a broad range of fiber-optic gyro applications," *Optics letters*, vol. 15, no. 12, pp. 673–675, 1990.
- [52] C. T. Derose, R. Himmelhuber, D. Mathine, R. Norwood, J. Luo, A.-Y. Jen, N. Peyghambarian *et al.*, "High  $\delta n$  strip-loaded electro-optic polymer waveguide modulator with low insertion loss," *Optics express*, vol. 17, no. 5, pp. 3316–3321, 2009.
- [53] B. Bortnik, Y.-C. Hung, H. Tazawa, B.-J. Seo, J. Luo, A. K.-Y. Jen, W. H. Steier, and H. R. Fetterman, "Electrooptic polymer ring resonator modulation up to 165 ghz," *Selected Topics in Quantum Electronics, IEEE Journal of*, vol. 13, no. 1, pp. 104–110, 2007.
- [54] Y. Cai and A.-Y. Jen, "Thermally stable poled polyquinoline thin film with very large electro-optic response," *Applied physics letters*, vol. 67, no. 3, pp. 299–301, 1995.
- [55] G. Treyz, P. May, and J.-M. Halbout, "Silicon mach-zehnder waveguide interferometers based on the plasma dispersion effect," *Applied physics letters*, vol. 59, no. 7, pp. 771–773, 1991.
- [56] N.-N. Feng, S. Liao, D. Feng, P. Dong, D. Zheng, H. Liang, R. Shafiha, G. Li, J. E. Cunningham, A. V. Krishnamoorthy *et al.*, "High speed carrier-depletion modulators with 1.4 v-cm  $v_i$  sub $i$   $\pi_i$ /sub $i$  l integrated on 0.25  $\mu\text{m}$  silicon-on-insulator waveguides," *Optics express*, vol. 18, no. 8, pp. 7994–7999, 2010.
- [57] Q. Xu, B. Schmidt, S. Pradhan, and M. Lipson, "Micrometre-scale silicon electro-optic modulator," *Nature*, vol. 435, no. 7040, pp. 325–327, 2005.
- [58] A. Birner, R. B. Wehrspohn, U. M. Gösele, and K. Busch, "Silicon-based photonic crystals," *Advanced Materials*, vol. 13, no. 6, pp. 377–388, 2001.
- [59] L. Alloatti, D. Korn, R. Palmer, D. Hillerkuss, J. Li, A. Barklund, R. Dinu, J. Wieland, M. Fournier, J. Fedeli *et al.*, "42.7 gbit/s electro-optic modulator in silicon technology," *Optics express*, vol. 19, no. 12, pp. 11 841–11 851, 2011.
- [60] T. Baehr-Jones, M. Hochberg, G. Wang, R. Lawson, Y. Liao, P. Sullivan, L. Dalton, A. Jen, and A. Scherer, "Optical modulation and detection in slotted silicon waveguides," *Optics Express*, vol. 13, no. 14, pp. 5216–5226, 2005.
- [61] T. Baehr-Jones, B. Penkov, J. Huang, P. Sullivan, J. Davies, J. Takayesu, J. Luo, T.-D. Kim, L. Dalton, A. Jen *et al.*, "Nonlinear polymer-clad silicon slot waveguide modulator with a half wave voltage of 0.25 v," *Applied Physics Letters*, vol. 92, no. 16, p. 163303, 2008.

- [62] X. Wang, C.-Y. Lin, S. Chakravarty, J. Luo, A. K.-Y. Jen, and R. T. Chen, "Effective in-device  $r_{33}$  of 735 pm/v on electro-optic polymer infiltrated silicon photonic crystal slot waveguides," *Optics letters*, vol. 36, no. 6, pp. 882–884, 2011.
- [63] T. Visser, H. Blok, B. Demeulenaere, and D. Lenstra, "Confinement factors and gain in optical amplifiers," *Quantum Electronics, IEEE Journal of*, vol. 33, no. 10, pp. 1763–1766, 1997.
- [64] C. M. Kim and R. V. Ramaswamy, "Overlap integral factors in integrated optic modulators and switches," *Lightwave Technology, Journal of*, vol. 7, no. 7, pp. 1063–1070, 1989.
- [65] D. Marcuse, "Electrooptic coupling between te and tm modes in anisotropic slabs," *Quantum Electronics, IEEE Journal of*, vol. 11, no. 9, pp. 759–767, 1975.
- [66] E. Chen and S. Y. Chou, "Characteristics of coplanar transmission lines on multilayer substrates: Modeling and experiments," *IEEE transactions on microwave theory and techniques*, vol. 45, no. 6, pp. 939–945, 1997.
- [67] S. Gevorgian and H. Berg, "Line capacitance and impedance of coplanar-strip waveguides on substrates with multiple dielectric layers," in *EUROPEAN MICROWAVE CONFERENCE*, vol. 31. Nexus Media Limited; 1996, 2001, pp. 153–156.
- [68] X. Xiao, X. Li, H. Xu, Y. Hu, K. Xiong, Z. Li, T. Chu, J. Yu, and Y. Yu, "44-gb/s silicon microring modulators based on zigzag pn junctions," *Photonics Technology Letters, IEEE*, vol. 24, no. 19, pp. 1712–1714, 2012.
- [69] R. K. Hoffman, *Handbook Microwave Integrated Circutes*. Artech House, 1987.
- [70] Y. Jie, W. Bo, H. Zhi-Ling, L. Ming-Ming, C. Wen-Qiang, B. Chuan, F. Xiao-Yong, and C. Mao-Sheng, "High-temperature permittivity and data-mining of silicon dioxide at ghz band," *Chinese Physics Letters*, vol. 29, no. 2, p. 027701, 2012.
- [71] J. Krupka, J. Breeze, A. Centeno, N. Alford, T. Claussen, and L. Jensen, "Measurements of permittivity, dielectric loss tangent, and resistivity of float-zone silicon at microwave frequencies," *Microwave Theory and Techniques, IEEE Transactions on*, vol. 54, no. 11, pp. 3995–4001, 2006.
- [72] M. Lee, O. Mitrofanov, H. Katz, and C. Erben, "Millimeter-wave dielectric properties of electro-optic polymer materials," *Applied physics letters*, vol. 81, no. 8, pp. 1474–1476, 2002.

- [73] S. Huang, T.-D. Kim, J. Luo, S. K. Hau, Z. Shi, X.-H. Zhou, H.-L. Yip, and A. K.-Y. Jen, “Highly efficient electro-optic polymers through improved poling using a thin tio 2-modified transparent electrode,” *Applied Physics Letters*, vol. 96, no. 24, pp. 243 311–243 311, 2010.
- [74] Y. Vlasov and S. McNab, “Losses in single-mode silicon-on-insulator strip waveguides and bends,” *Optics Express*, vol. 12, no. 8, pp. 1622–1631, 2004.
- [75] T. Bååk, “Silicon oxynitride; a material for grin optics,” *Appl. Opt.*, vol. 21, no. 6, pp. 1069–1072, Mar 1982. [Online]. Available: <http://ao.osa.org/abstract.cfm?URI=ao-21-6-1069>

# Index

## Symbols

3-(Triethoxysilyl)-propyl-succinic-acid- anhydride, 27

## B

Bispenta-fluoro-diphenyl-dimethoxy-silane, 18  
BPFDPDMS, *see* Bispenta-fluoro-diphenyl-dimethoxy-silane

## C

CMOS, 70  
colloid, 14  
Complex refractive indices, 64  
Confinement Factor, 73

## D

DC field, 77  
Dielectric constant, 44  
Diphenyl-dimethoxy-silane, 18, 20  
Diphenylsilanediol, 17  
DPDMS, *see* Diphenyl-dimethoxy-silane  
DPSD, *see* Diphenylsilanediol

## E

EFM, 44  
Eigenvalue, 71, 88  
Electrode Design, 75  
Electrode loss, 81

## F

Fiber Mach-Zehnder, 86  
Field Enhancement, 90  
Figure of merit, 82  
Fresnel reflection, 66  
FT-IR, 29, 33

## G

Glycidyl-methacrylate, 31  
GLYME, *see* Glycidyl-methacrylate

## I

Index ellipsoid, 53

## L

Line capacitance, 81  
Lithium niobate, 53, 69

## M

Mach-Zehnder modulator, 69  
MAPTMS, *see* Methacryl-oxipropyl-trimethoxy-silane  
Methacryl-oxipropyl-trimethoxy-silane, 18  
Microwave loss, 81

## N

Naphthalen-trimethoxy-silane, 18, 22  
NaphTMS, *see* Naphthalen-trimethoxy-silane

## O

Optical loss, 17, 21  
Overlap Integral, 71, 78, 88

## P

Phenyl-trimethoxy-silane, 18  
Photoinitiator, 18  
PO, *see* Propylene-oxide  
Pockels Effect, 50  
Precursors, 17  
Propylene-oxide, 31  
PTMS, *see* Phenyl-trimethoxy-silane

## R

Refractive index tuning, 22, 23

Rutile, 44

## S

SHG, 61

Sidecladding, 90

Silicon modulator, 71

Silicon nitride, 87

Sol, 14

Sol Gel, 14

SucAHTES, *see* 3-(Triethoxysilyl)-propyl-  
succinic-acid-anhydride

Susceptibility, 48

Switching Voltage, 71

## T

TE loss, 86

TE mode, 72

THG, 61

Titania, 32

Titania-terta-chloride, 31

## W

Waveguide, 23

## X

XPS, 36